Clemson University
TigerPrints

All Theses | Theses

8-2010

INVESTIGATING PRE-BREAKDOWN CURRENTS IN POLYMER TANTALUM CAPACITORS

Githin Alapatt
Clemson University, githin@gmail.com

Follow this and additional works at: https://tigerprints.clemson.edu/all_theses

Part of the Electrical and Computer Engineering Commons

Recommended Citation

Alapatt, Githin, "INVESTIGATING PRE-BREAKDOWN CURRENTS IN POLYMER TANTALUM CAPACITORS" (2010). *All Theses*. 864.
https://tigerprints.clemson.edu/all_theses/864

This Thesis is brought to you for free and open access by the Theses at TigerPrints. It has been accepted for inclusion in All Theses by an authorized administrator of TigerPrints. For more information, please contact kokeefe@clemson.edu.

INVESTIGATING PRE-BREAKDOWN CURRENTS IN POLYMER TANTALUM CAPACITORS

A Thesis
Presented to
the Graduate School of
Clemson University

In Partial Fulfillment
of the Requirements for the Degree
Master of Science
Electrical Engineering

---

by
Githin Francis Alapatt
August 2010

Accepted by:
Dr. William R. Harrell, Committee Chair
Dr. Kelvin F. Poole
Dr. Yuri Freeman
Dr. Joel S. Greenstein

ABSTRACT

Poly(3,4-ethylenedioxythiophene) (PEDOT), a conducting polymer, has been used since the 1990s for the cathode of tantalum capacitors, which have a tantalum anode, and a layer of tantalum pentoxide as the dielectric. Such capacitors are referred to as Polymer Ta capacitors. The first method, an *in situ* polymerization technique, used to deposit the polymer resulted in capacitors with a significant leakage current and breakdown voltages near 50 V. The second method, a pre-polymerization (pre-poly) technique, resulted in capacitors that have a much lower leakage current and a higher breakdown voltage than the *in situ* capacitors.

In this thesis, an accurate measurement technique for dielectric leakage current, also referred to as the pre-breakdown current, was established for capacitors. Current versus time measurements at constant voltage were performed at several voltages and the results were compiled to obtain the current-voltage (I-V) characteristics of both *in situ* and pre-poly types of capacitors. These characteristics were then modeled and analyzed, which led to the conclusion that the pre-breakdown current is controlled by the Poole-Frenkel mechanism in the *in situ* capacitors and by both the Poole-Frenkel and Schottky mechanisms in the pre-poly capacitors. Current versus time measurements were also performed at various temperatures to obtain the activation energy for the current in the capacitors and to verify the leakage mechanisms. Results suggest the presence of shallow 0.15 eV traps in the dielectric of the *in situ* capacitor and deeper 0.75 eV traps in that of the pre-poly capacitor. Additionally, pre-poly capacitors also have a 0.54 eV Schottky barrier that limits the electrons from being emitted into the dielectric from the electrode. Both the deep trap levels and the Schottky barrier explain the lower leakage current and higher breakdown voltage observed in the pre-poly capacitors as compared to the *in situ* capacitors.

DEDICATION

I dedicate this thesis to my parents, wife, and sister, for their constant support and encouragement.

ACKNOWLEDGEMENTS

I would like to thank my advisor, Dr. William R. Harrell, for his guidance while conducting this research and writing this thesis. I would also like to thank Dr. Yuri Freeman for his assistance and KEMET Electronics Corporation for supporting this project financially for the past three years. Sincere gratitude also goes to Dr. Kelvin F. Poole for the valuable discussions I have had with him. I would also like to thank Dr. James E. Harriss for his help in the Microstructures Laboratory with device fabrication. I also express gratitude to Dr. Joel S. Greenstein who reviewed my thesis and served on my thesis committee.

I also appreciate the support during research from Dr. Philip Lessner, Dr. Erik Reed, Mr. Tony Kinard and Dr. James Chen of KEMET Electronics Corporation, and Dr. Igor Luzinov of Clemson. I am also grateful to Ms. Barbara Ramirez, Director of the writing center at the Class of 1941 Studio for Student Communications at Clemson, who has helped me to improve this thesis. I would also like to thank Mr. Kapil C. Madathil for authoring a software package that made data compilation easier for me, Mr. Sriram Ravindren for proof reading this thesis, and Mr. John Hicks for his help in the ECE shop. Thanks also go to Mr. Jesse Grant for his good company during the writing of this thesis.

A part of this thesis was presented in the conference paper: G.F. Alapatt, W. R. Harrell, Y. Freeman and P. Lessner, “Observation of the Poole-Frenkel Effect in Tantalum Polymer Capacitors” presented at IEEE SoutheastCon 2010, Charlotte, NC, USA.

TABLE OF CONTENTS

Page

TITLE PAGE i

ABSTRACT ii

DEDICATION iii

ACKNOWLEDGMENTS iv

LIST OF TABLES vii

LIST OF FIGURES viii

CHAPTER

1. INTRODUCTION 1
   - 1.1. Electrolytic Capacitors 1
   - 1.2. Summary of Chapters 5
2. EVOLUTION OF TANTALUM CAPACITORS 7
3. POLYMER TANTALUM CAPACITORS 13
   - 3.1. Introduction 13
   - 3.2. Fabrication of Polymer Tantalum Capacitors 14
   - 3.3. Primary Electrical Properties 18
   - 3.4. Modeling Polymer Tantalum Capacitors as MIS Devices 25
4. BREAKDOWN PHENOMENON IN TANTALUM CAPACITORS 27
   - 4.1. Breakdown Phenomenon in Dielectrics 27
   - 4.2. Dielectric Breakdown Phenomenon in Tantalum Capacitors 32
   - 4.3. Poole-Frenkel Mechanism 35
   - 4.4. Schottky Effect 36
   - 4.5. Space Charge Limited Conduction Mechanism 37
   - 4.6. Tunneling Mechanism 38
   - 4.7. Fowler-Nordheim Tunneling Mechanism 40
   - 4.8. Activation Energy of a Leakage Mechanism 41
   - 4.9. Leakage Mechanisms Observed in Tantalum Pentoxide Structures 42
5. ELECTRICAL CHARACTERIZATION TECHNIQUES FOR CAPACITORS 45
   - 5.1. I-V measurements 45
     - 5.1.1 Limiting Noise in I-V Measurements 45
     - 5.1.2 Determining Time Delay required for I-V Measurements 50
   - 5.2. C-V Measurements 60
   - 5.3. Performing Measurements as a Function of Temperature 63

Table of contents (Continued)

Page

6. CHARACTERISTICS OF POLYMER TANTALUM CAPACITORS 65
    6.1. *In situ* Capacitors 66
    6.2. Pre-poly Capacitors 72
    6.3. Comparison of *In situ* and Pre-poly Capacitors 82
    6.4. Reverse Polarity Characteristics of Tantalum Capacitors 84
7. SUMMARY AND CONCLUSIONS 90

APPENDIX 93

REFERENCES 98

LIST OF TABLES

Page

I. Leakage mechanisms observed in Ta_2O_5 devices. 43

II. Results from Series and Parallel mode measurements 62

LIST OF FIGURES

Page

1.1. Model of a real capacitor 4

2.1. ESR and Maximum WV in the tantalum D case capacitors 9

2.2. Comparison of Technology Mix in a Laptop produced in 2003 and 2005 12

3.1. Functional parts and materials of the polymer Ta capacitor 13

3.2. Tantalum pellet before and after the pressing and sintering process 14

3.3. Structure of the polymer Ta capacitor 17

3.4. Tantalum capacitor in a chip-type package 18

3.5. Variation of ESR with frequency 19

3.6. Distributed RC network model of the capacitor 20

3.7. Simplified distributed RC model 20

3.8. Capacitance roll-off in MnO_2 and polymer Ta capacitors 21

3.9. Electrical Conditioning of the polymer Ta capacitor 22

3.10. Variation of leakage current in *In situ* and Pre-poly capacitors 24

3.11. Simplified capacitor structure for analysis 25

4.1. Generation of traps leading to breakdown 30

4.2. Variation of BDV in SiO_2 films with its thickness 32

4.3. Dependence of Breakdown voltage on dielectric thickness in Ta capacitors 34

5.1. I-time measurement result on an polymer Ta capacitor 46

5.2. Simplified schematic of the measurement system 47

5.3. I-time measurement result on polymer Ta capacitor with the series resistor 50

5.4. Current decay in an *in-situ* capacitor for the first 200 s. $V_0 = 15$ V. 53

List of Figures (Continued)

Page

5.5. Current decay in an *in-situ* capacitor from t = 175 s to 17 ks. V_0 = 15 V 55

5.6. I-time measurement results at 15 V on an *in situ* capacitor. 56

5.7. Compiled I-V data of an *in situ* capacitor from I-time measurements 57

5.8. Results from incorrect I-V measurements on an *in-situ* capacitor 59

5.9. Graphite probe attached to an alligator clip 60

6.1. I-V characteristics of *in situ* capacitors 67

6.2. Schottky plot of the I-V characteristics of *in situ* capacitors 69

6.3. PF plot of the I-V characteristics of *in situ* capacitors.. 70

6.4. Arrhenius plot for the *in situ* capacitors 72

6.5. I-V characteristics of pre-poly capacitors 74

6.6. Schottky plot of I-V characteristics of pre-poly capacitors... 75

6.7. Arrhenius plot for pre-poly capacitor (Sample 3)... 77

6.8. PF plot of the I-V characteristics of pre-poly capacitors... 78

6.9. Variation of current with time in Sample 4 at 250 K. 80

6.10. Arrhenius plot for pre-poly capacitor (Sample 4) 81

6.11. Comparison of I-V characteristics of *in situ* and pre-poly capacitors 83

6.12. I-V curve of discrete polymer capacitors from – 1 to 10 V. 85

6.13. I-V characteristics of the Ta-Ta_2O_5-Al MIM structure 86

6.14. Electronic band structure of Ta-Ta_2O_5-Al 87

A.1. Results from fourteen continuous I-time runs on an *in situ* capacitor........................... 94

A.2. Comparison of I-time results on all samples 95

A.3. Worst-case PF plot 97

CHAPTER ONE

INTRODUCTION

1.1 Electrolytic Capacitors

Electrolytic capacitors are a class of capacitors in which the anode is typically a metal and the cathode is either a conductive electrolyte or a conducting organic or inorganic material. A material with a high dielectric strength, a high dielectric constant, and good film forming properties is employed as the capacitor's dielectric. This material is typically a natural oxide of the anodic metal because a high quality thin layer of it can be grown easily on the anode. The primary function of the dielectric is to maintain a fixed distance between the anode and the cathode to create a capacitance between them. It also acts as an insulator that blocks the flow of dc current between the electrodes. This dielectric is often fragile and uneven, requiring the cathode to be a soft material or a liquid. The liquid electrolyte also helps to reform the dielectric, meaning the electrolyte promotes the re-growth of the dielectric at a local hot spot when the capacitor has a dc bias applied across it.

Given its structure, the electrolytic capacitor can be treated as a parallel plate device, the capacitance of which is given by

$$C = \frac{A\epsilon_0\epsilon_r}{d} \tag{1.1}$$

where, A is the area of the capacitor, d the thickness of the dielectric, ϵ_0 the permittivity of free space and ϵ_r the relative permittivity of the dielectric, also known as the dielectric

constant. In theory, the capacitor does not conduct dc current; however, because the capacitor is not perfect, some dc current always flows through the capacitor when a dc voltage is applied across it. This current is an important parameter of the capacitor, referred to as the capacitor's leakage current. The magnitude of this current is dependent on factors such as the quality and type of dielectric, the anode and cathode material, and the dielectric thickness. When a sufficiently high dc voltage is applied across the capacitor, it breaks down because of the excessive leakage current, which damages the dielectric. This voltage, another important parameter of the capacitor, is referred to as the breakdown voltage (BDV) of the capacitor. Because it is unsafe to operate capacitors near their breakdown voltage, they are typically rated to work reliably up to approximately half of their breakdown voltage or even below. This maximum rated dc voltage below which the capacitor works reliably is referred to as its working voltage (WV). While the breakdown voltage is a parameter of the capacitor and is determined by the manufacturing process and technology, the working voltage is determined by the manufacturer based on reliability and life tests conducted on numerous capacitors. Another important parameter of a capacitor is its maximum reverse voltage, the maximum voltage that can be applied momentarily across the capacitor at reverse polarity without causing dielectric damage. It is typically about 10% of the rated working voltage at room temperature. This restriction is in place because the electrolytic capacitors typically exhibit polar characteristics, meaning they conduct heavily and breakdown even when a small reverse bias is applied across them.

The product of a capacitor's capacitance and its working voltage (C·V) is roughly constant for a given electrode area, or the case size of the device. This is because, in order to increase the working voltage, the manufacturers increase the dielectric thickness resulting in a lower capacitance according to Eq. 1.1. This C·V product is important because the capacitor manufacturers fix the maximum leakage limit in terms of the current per C·V, equivalently, microamperes per microfarad volt $\mu A/(V \cdot \mu F)$. Typically, this figure is in the range of 0.01 to 0.1 $\mu A/(V \cdot \mu F)$. The C·V accounts for the voltage existing across the capacitor and its capacitance; it is possible to calculate the electric field across the oxide from the capacitance, because the capacitance is directly related to the oxide thickness. In addition, $Q = C \cdot V,$ so the charge on the capacitor is also known. Therefore, the number of microamperes per microfarad volt represents the minimum time constant for self-discharge, or the maximum leakage at constant field. For a uniform and perfect dielectric, the parameter $\mu A/(V \cdot \mu F)$ should be independent of the dielectric thickness.

A manufactured capacitor can be modeled electrically using ideal capacitors, resistors, and inductors as shown in Fig.1.1. The ESL stands for Equivalent Series Inductance that exists because of the lead wire used inside the capacitor's assembly. The ESL in most instances is a very small value and is negligible. The Equivalent Series Resistance (ESR) is the value of the resistance the capacitor offers to ac signals. Factors contributing to the ESR are the resistance of the lead wires and the capacitor's electrodes. C in this figure stands for an ideal capacitive element that predomiantly contributes to the capacitance of the capacitor. R_L is the capacitor leakage resistance which accounts for the

capacitor's small dc leakage current. Its value is approximately 50 GΩ for tantalum capacitors and about 1000 GΩ for ceramic and film capacitors. C_d and R_d represent a capacitor and a resistor that accounts for the capacitive and resistive losses due to dielectric absorption and molecular polarization [1].

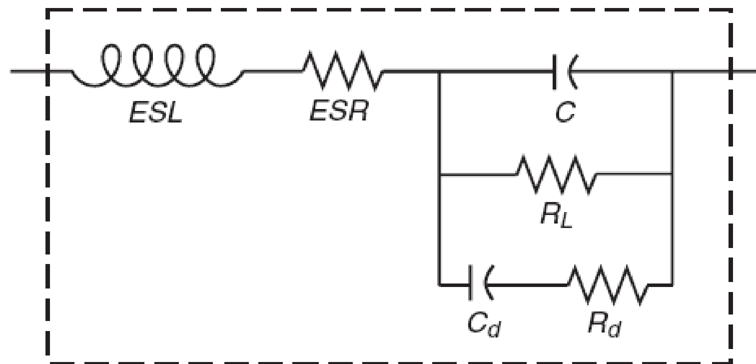

Fig.1.1. Model of a real capacitor. (Adapted from [1])

Electrolytic capacitors have certain features that make the capacitor's use attractive in military, space, and medical applications. Their most important feature is their high volumetric efficiency, meaning they can hold more charge per unit volume; this is because of their large surface area and extremely thin dielectric film. Historically, the biggest drawbacks of using the electrolytic capacitors are that they have a high ESR and they exhibit polar characteristics. They are typically used for bypassing, decoupling, and filtering applications where the ac component of the applied signal is comparatively lower than its dc component. This restriction exists because electrolytic capacitors are typically polarized. Further details on electrolytic capacitors are available in the literature [2-4].

Electrolytic capacitors have a long history and it is interesting to note that the first patent for an electrolytic capacitor was given to Charles Pollak in 1897, who designed a capacitor using aluminum. Tantalum and niobium electrolytic capacitors were investigated by G. Schulze in the early 1900s. The first tantalum electrolytic capacitor was manufactured by Fansteel Metallurgical Corporation in 1925 and the first miniature porous tantalum electrolytic capacitors were first sold in 1949 [5]. Tantalum capacitors manufactured since the 1950s use pressed and sintered particles of tantalum to form the anode because the particles help to increase the surface area of the anode and thus the volumetric efficiency. This research focuses primarily on the electrical properties of polymer based tantalum electrolytic capacitors and the current conduction in its dielectric, tantalum pentoxide, which is tantalum's natural oxide.

1.2 Summary of Chapters

In Chapter 2, the evolution of tantalum capacitors is discussed and some of its properties are examined.

In Chapter 3, the polymer tantalum capacitor is introduced and its fabrication and properties are reviewed in detail. The polymer capacitor is also compared to the standard Metal Insulator Semiconductor (MIS) device.

In Chapter 4, the breakdown in polymer tantalum capacitors is reviewed in detail along with the basic theory of dielectric breakdown. The basic conduction mechanisms in dielectrics – Poole-Frenkel Effect, Schottky Effect, Space Charge Limited Current, and Tunneling are also examined.

In Chapter 5, the techniques that were devised for performing I-V and C-V measurements on the tantalum capacitors are presented.

In Chapter 6, the major results from the current versus time measurements performed on the polymer tantalum capacitors are presented. The results include characteristic plots of leakage mechanisms, and Arrhenius plots.

Finally, in Chapter 7, the previous chapters are summarized and conclusions are presented based on the results from this research.

CHAPTER TWO

EVOLUTION OF TANTALUM CAPACITORS

Tantalum capacitors were developed in order to address the poor electrical quality associated with the aluminum capacitor, which used aluminum as the anode material. Aluminum capacitors had two major shortcomings: they were bulky and had a limited shelf life. Replacing the aluminum at the anode with tantalum resulted in major improvements due to the following properties: high volumetric efficiency of tantalum, chemical stability of the tantalum metal and its oxide, the high dielectric constant of tantalum's oxide, compatibility of tantalum's oxide with electrolytes possessing a high conductivity and a low freezing point. Thus, this change resulted in a capacitor that was miniaturized, had an increased shelf life, had a wider range of operating temperature, and possessed a higher overall electrical quality. During the last fifty years, tantalum powder used to construct the anode was made even finer, increasing the capacitor's area and, hence, its capacitance. It increased from 1000 CV/g in the 1960s to more than 150000 CV/g in the 2000s [6, 7]. This increase is technically referred to as an increase in volumetric efficiency, which is the ability to achieve a larger capacitance per gram (or cm^3) of tantalum powder and is measured in charge/unit weight or charge/unit volume.

Tantalum capacitors are broadly divided in two types based on the nature of their cathode: wet or solid. The wet capacitor employs a conducting liquid electrolyte as the cathode, while a solid capacitor employs a solid conducting material as the cathode. The first tantalum capacitors were manufactured in the 1940s and were of the wet type. It had a sintered tantalum anode, a thin layer of Ta_2O_5 dielectric, and a liquid electrolyte such as

sulfuric acid as the cathode. The advantage of using a liquid electrolyte as the cathode is that it conforms to the dielectric's surface and helps the dielectric to be reformed at a fault site during capacitor operation. Reformation refers to electric field assisted recreation of the dielectric at the point where it has been damaged. This capability is necessary because the initially created oxide might have defects due to impurities in the anode metal [1].

However, using a liquid electrolyte requires a hermetic seal to prevent it from evaporating or leaking. Leaks are potentially dangerous because of the acidic nature of the electrolyte. Another disadvantage of using the liquid electrolyte is that it freezes at low temperatures and prevents the capacitor from functioning [8]. Despite all these factors, wet tantalum capacitors work reliably up to approximately 150 V and are still used in applications that require high working voltages.

To solve the problems associated with the liquid electrolyte, Bell Labs developed a solid electrolytic capacitor in 1950s [9]. It employed manganese dioxide (MnO_2), a solid semiconducting material, as the counter electrode in place of the liquid electrolyte, thus avoiding the presence of any liquids in the system. In comparison to the wet tantalum capacitor, this new solid capacitor had a reduced capacitor volume, better high temperature characteristics, a lower power factor, and a longer shelf life. In addition, since the solid capacitor did not contain a liquid electrolyte, a hermetic seal was not required [9]. However, solid tantalum capacitors are limited to a lower maximum working voltage of approximately 75 V, compared to 150 V for the wet tantalum capacitors. This limitation was not seen as a serious problem because the industry was

beginning to manufacture transistorized circuits that required relatively small operating voltages. Similar to the wet tantalum capacitors, tantalum capacitors with MnO_2 counter electrodes are still manufactured and used widely today. The ESR and working voltage of three types of capacitors are shown in Fig. 2.1. One of the Y-axes shows the ESR in mΩ and the other Y-axis shows the working voltage (WV) in volts. The X-axis shows a timeline from 1940 to 1990 and the cathode material/capacitor technology. In this figure, Polymer refers to a type of solid capacitor with a polymeric cathode, which will be discussed in this section later. From the figure, it is evident that the ESR and Working voltage have been decreasing over the last fifty years.

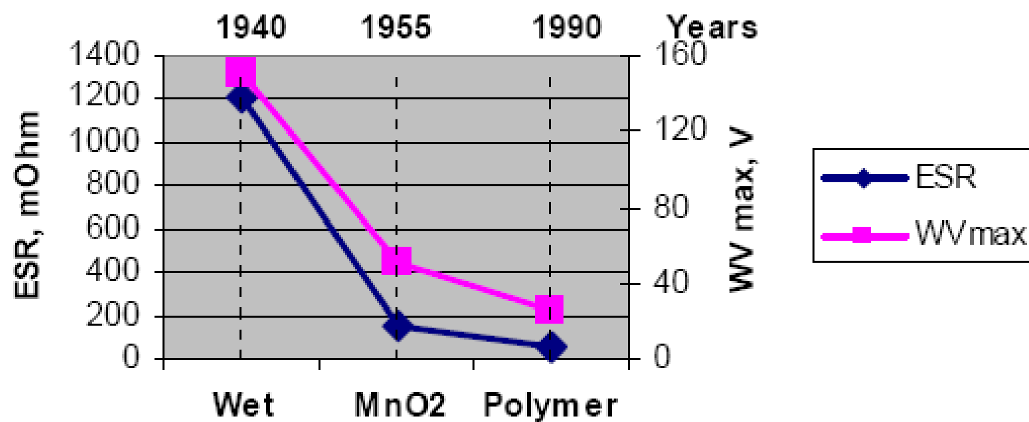

Fig. 2.1. ESR and Maximum WV in the tantalum D case capacitors [10].

Another advantage of using MnO_2 is that if a local hot spot is formed in the dielectric due to a defect and excessive current flows through it, the conductive material near the defect site becomes oxidized to Mn_2O_3, which has much lower conductivity than the initial MnO_2. The defect becomes isolated since the resistivity around the hot-spot

falls significantly, ensuring that no further current flows through it. This self-healing, or electrical conditioning property, is what makes MnO_2 – based capacitors useful. These capacitors also work well under thermo-mechanical loads and at high temperatures, and exhibit good DC bias and steady state reliability [11].

However, one disadvantage of MnO_2 is that it is a poorly conducting material and cannot satisfy the ultra low Equivalent Series Resistance (ESR) requirements of the modern electronics industry. The conductivity of MnO_2 is 0.1 S/cm, meaning it is not possible to manufacture ultra low ESR capacitors using this material [12]. A low ESR capacitor is useful in applications that require capacitors with a smaller RC delay and lesser I^2R power being dissipated over the series resistance [13]. These are important characteristics of modern integrated and discrete circuit designs, which employ higher operating frequencies and lower supply voltages [14]. For example, the Intel 8086 processor released in the late 1970s ran on a 5 V supply at 5 MHz, while the Intel Atom processor released in 2009 requires only a 1.2 V supply and operates at 2 GHz. In addition, overall power consumption per chip has increased over the last 40 years because of the increase in circuit functionality and performance. This increased power consumption coupled with the lower supply voltage results in a large current flowing in the circuit. These large currents in conjunction with the high frequency signals in the circuit make low ESR capacitors particularly important in today's circuits.

A second disadvantage of the tantalum MnO_2 capacitor is that under certain conditions, it exhibits a catastrophic ignition failure when the extreme heat generated in the capacitor causes it to ignite [1]. MnO_2, which is a good source of oxygen, fuels an

exothermic process converting pure tantalum at the anode into crystalline tantalum pentoxide. This is extremely dangerous as the ignition of the capacitor can burn the circuitry around it and cause serious damage to the entire product. It is best for devices to fail, if at all, in a graceful mode. Finally, a third disadvantage is that the MnO_2 deposition process involves the application of high temperatures which might cause cracks in the dielectric because of the stress created due to the mismatch in the coefficient of thermal expansion of the materials constituting the capacitor. Even the smallest crack can increase the leakage current, causing the capacitor to fail [15]. Because of these two disadvantages, the solid tantalum MnO_2 capacitors have reliability issues.

In the late 1980s, an intrinsically conducting polymer was proposed to replace MnO_2 as the counter electrode in the tantalum capacitors because of its higher conductivity, higher reliability, and ease of synthesis [16-22]. Polyaniline, polypyrole and Poly(3,4-ethylenedioxythiophene) (PEDOT) were the conductive polymers initially investigated to replace MnO_2 [12, 23, 24]. Tantalum capacitors manufactured using these polymer counter electrodes do not exhibit the catastrophic burning failure mechanism because they do not have sufficient oxygen to fuel the reaction [1]. They also have a lower ESR and better high frequency characteristics. In addition, polymer-based capacitors have the advantage of higher reliability because their deposition technique does not involve high temperatures, which can cause cracks in the dielectric [15].

This change in the cathode material provided the advantage needed by the capacitors to be suitable for modern electronic battery-operated devices. The increased reliability and stability of polymer tantalum capacitors makes them attractive for military,

space, and medical applications [10]. For example, in a case study, it was found that in 2003, 47% of the capacitors inside a typical laptop computer were of the tantalum-polymer type and in 2005, this figure has jumped up to 70% [11]. The full details of the case study are represented numerically on the pie chart in Fig 2.2.

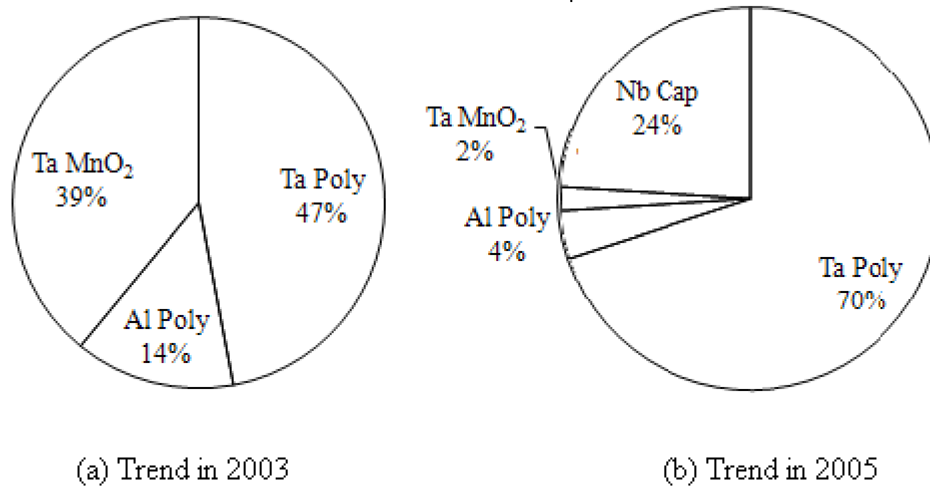

Fig 2.2. Comparison of Technology Mix in a Laptop computer produced in (a) 2003 and (b) 2005. (Adapted from [11])

The evolution of tantalum electrolytic capacitors has been explored and the properties of the existing three types of tantalum capacitors were compared. To understand the characteristics of the polymer based tantalum capacitors, its fabrication, and properties need to be investigated.

CHAPTER THREE

POLYMER TANTALUM CAPACITORS

3.1 Introduction

The structure of a polymer tantalum capacitor is similar to that of the earlier tantalum MnO_2 capacitor, except that while forming the cathode, Poly(3,4-ethylenedioxythiophene) (PEDOT) instead of MnO_2 is deposited on the dielectric. During fabrication, the Ta anode is made first, then a layer of tantalum pentoxide is grown on the Ta, forming the dielectric. Finally, a layer of conductive polymer is deposited on the dielectric, which forms the cathode. This layered structure is shown in Fig 3.1 in which the capacitor's functional parts and the materials are marked. Although this is not a complete packaged capacitor at this point, these are the primary material layers that form the capacitor.

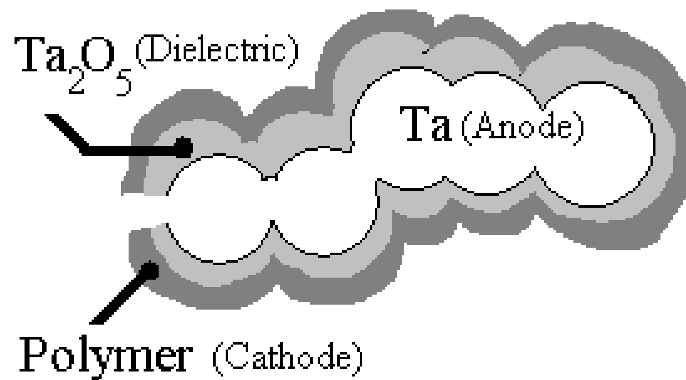

Fig. 3.1. Functional parts and materials of the polymer Ta capacitor.

3.2 Fabrication of Polymer Tantalum Capacitors

The capacitor's anode is fabricated using fine powdered tantalum in order to maximize the area of the anode and thus, the capacitance per unit gram of tantalum powder, thereby achieving a high volumetric efficiency. The powdered tantalum is first pressed into a pellet around a tantalum riser wire and then sintered in vacuum at 1350 °C for 10 minutes. This sintering process helps to establish good electrical connectivity between the individual particles of the powder. Fig 3.2 shows a pellet with a riser wire before and after the pressing and sintering process. The tantalum riser wire serves as an external common contact to all the tantalum particles in the pellet as is evident in the figure. To enhance the morphology of tantalum, necessary for good performance, deoxidizing and decarbonizing steps are performed [25].

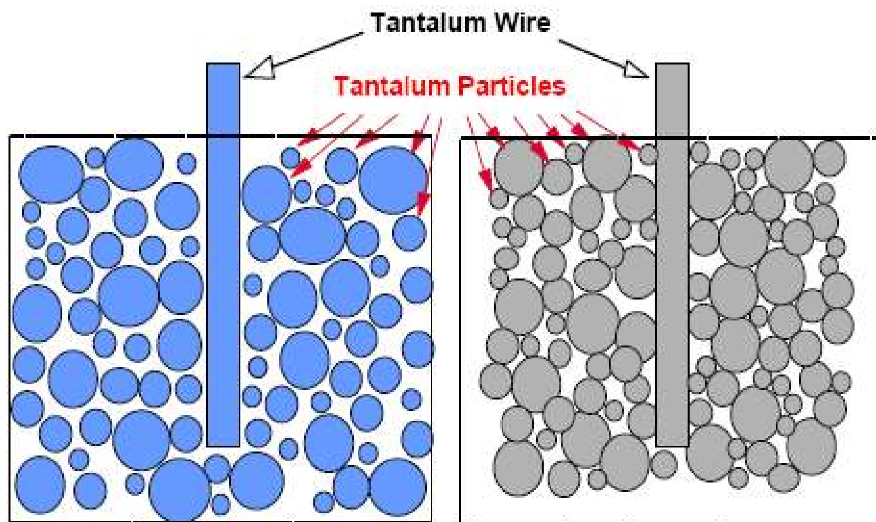

Fig. 3.2. Ta pellet before (left) and after (right) pressing and sintering [1].

The dielectric is formed through an electrochemical anodization process, during which the anode structure is placed in an electrolytic bath containing an aqueous solution of 0.01 mol% phosphoric acid at 80 °C. A dc voltage, referred to as the formation voltage, is subsequently applied at the anode with respect to the bath. The power supply applying the formation voltage is set to a maximum current of 1 mA/cm^2, an optimal value based on experiments conducted at KEMET, which showed that increasing the current density promotes quicker oxide formation; however, the oxide also tends to crystallize, resulting in hot spots when it is grown using a high current density. With this formation voltage applied, an oxide film of Ta_2O_5 begins to grow on the Ta metal, forming the dielectric. The chemical equations pertaining to this process are:

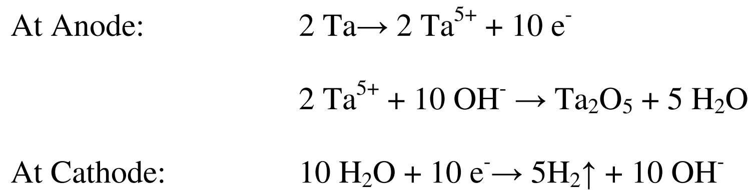

At Anode: $2\,Ta \rightarrow 2\,Ta^{5+} + 10\,e^-$

$2\,Ta^{5+} + 10\,OH^- \rightarrow Ta_2O_5 + 5\,H_2O$

At Cathode: $10\,H_2O + 10\,e^- \rightarrow 5H_2\uparrow + 10\,OH^-$

The Ta ions created at the anode combine with the OH ions created from the aqueous phosphoric acid and result in the formation of Ta_2O_5 and hydrogen. Ta_2O_5 is deposited at the Ta anode, while hydrogen escapes from the solution forming bubbles. The thickness of the oxide grown varies with the applied formation voltage and can be determined from the relationship, T_{ox} = 2 nm/V at 80 °C [5].

This electrochemical setup initially works as a current limited circuit with the current level continuously decreasing and the voltage across the oxide increasing as the

oxide grows in thickness. When the pre-determined thickness of oxide is formed on the anode, the voltage ceases to increase and the setup becomes voltage limited. This electrochemical process of growing the dielectric layer, which takes approximately three hours, results in a layer of amorphous Ta_2O_5 on the surface of the anode. Strictly speaking, the oxide not only forms on the surface of the metal, but also consumes some of the metal, growing down into the anode. This general method of oxide growth is referred to as oxide formation at constant potential process. Additional annealing steps are also conducted to enhance the quality of the grown oxide.

The cathode of the capacitor is formed using one of the two commercial methods of depositing the conducting polymer. The first method involves the *in situ* oxidative polymerization of ethylenedioxythiophene (EDOT) (Clevios™ M from H.C. Starck) with iron (III) toluenesulfonate and capacitors formed by this method are referred to as *in situ* type polymer Ta capacitors. The second method involves the application of pre-polymerized PEDOT particles (Clevios™ K from H.C. Starck) onto the dielectric through a dip and dry process. These are referred to as pre-poly or slurry type polymer Ta capacitors because of the pre-polymerized slurry applied to the dielectric to create the cathode. For both processes, a conductive layer of PEDOT is formed on the surface of the capacitor during this cathode formation process.

Although a capacitor is functional when the anode, dielectric, and cathode are formed, the exposed PEDOT needs to be covered with a more robust material to establish an external contact. This is achieved by first coating the PEDOT surface with a conductive graphite powder in order to enhance the conductivity at the interface, and then

covering the graphite with silver paint to create a low resistance connection. The initial graphite coating helps to prevent the formation of silver oxide between the silver paint and the PEDOT [26].

The capacitor structure formed at this stage is illustrated in Fig 3.3. This capacitor is then cured and conductive epoxy is subsequently used to connect the silver surface with a lead frame [1]. The Ta riser wire at the anode is welded to a second lead frame element. This entire structure is packaged in plastic with the lead frames protruding from opposite sides as illustrated in Fig.3.4. The particular type of packaging shown in Fig 3.4 is known as a chip-type package, approximately 3mm x 8mm x 5mm.

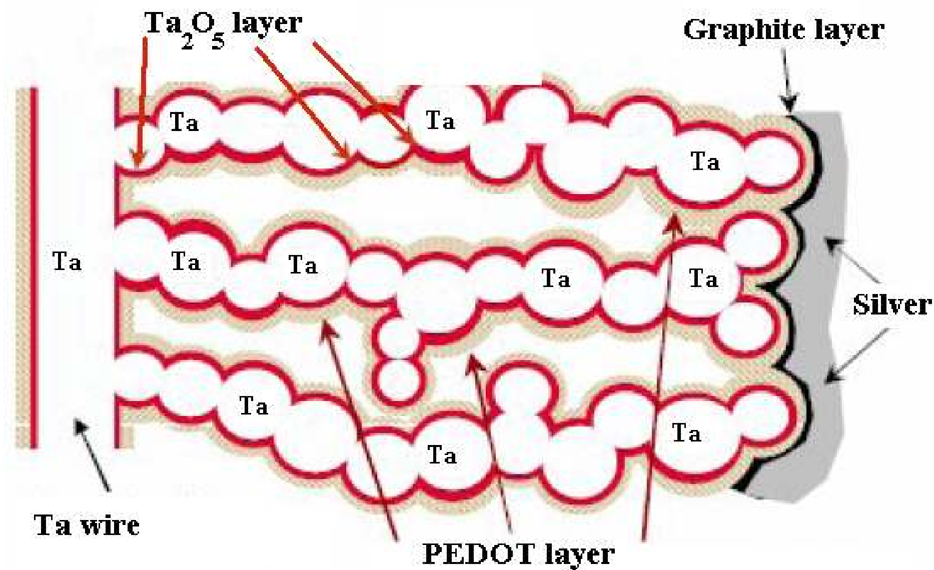

Fig 3.3. Structure of the Polymer Ta capacitor. (Adapted from [26])

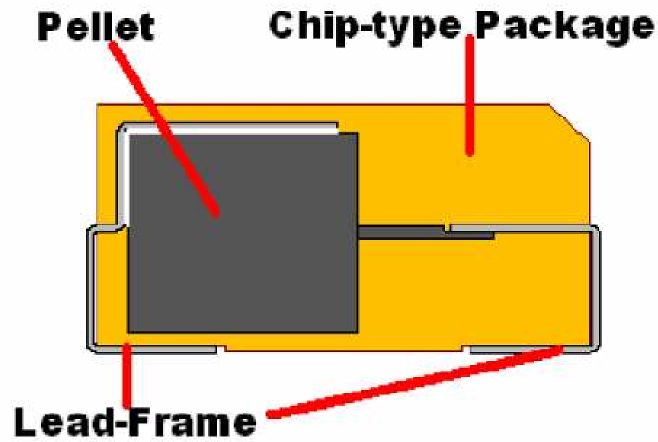

Fig. 3.4. Tantalum capacitor in a chip-type package [27].

3.3 Primary Electrical Properties

The attractive features of the polymer Ta capacitor giving it a competitive edge over other types are its low ESR, its self-healing mechanism, and its high stability and reliability.

The polymer Ta capacitor has a lower ESR than its MnO_2 counterpart throughout the entire frequency spectrum as can be seen in the plot in Fig. 3.5. In this figure, the ESR is plotted against signal frequency. At low frequencies near 10 kHz, the ESR of the Low ESR MnO_2 and the Commercial MnO_2 capacitor is greater than twice that of the polymer capacitor, while at higher frequencies, the ESR of all capacitors reduces to a low value because inner resistive components of the capacitor become unresponsive and no longer contribute to the total series resistance.

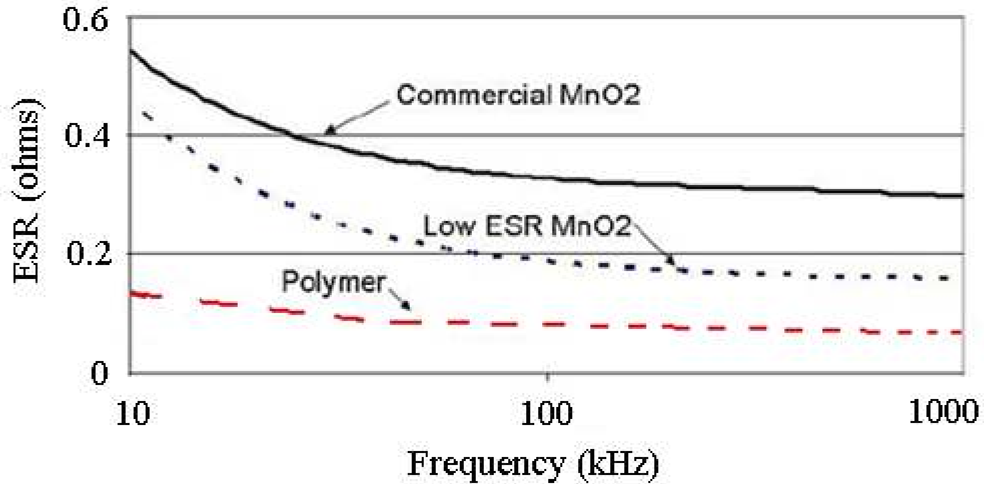

Fig. 3.5. Variation of ESR with frequency. (Adapted from [28])

One benefit of this low ESR is that the polymer Ta capacitor has an improved capacitance roll-off with frequency because of the reduction in the Resistance-Capacitance (RC) ladder effect. This RC ladder, as illustrated in Fig 3.6, is created within the capacitor because of the use of powdered tantalum particles at the anode. This distributed network RC model of the capacitor is made up of individual, but connected, particles of tantalum covered by the dielectric and the cathode [26]. Ignoring the resistivity of tantalum at the anode, the structure in Fig 3.6 can be simplified to the RC network as shown in Fig. 3.7, which accounts only for the resistance created due to the resistivity of the cathode material. For an individual capacitive element, C1, situated away from the cathode, the RC time constant is high due to the cumulative effect of all the resistors R1, R2 and so on until Rn, in its path. This high time constant will prevent C1 from responding to high frequency signals. Because of the low ESR in polymer Ta

capacitors, the values of individual resistors are low and hence the RC ladder effect is small.

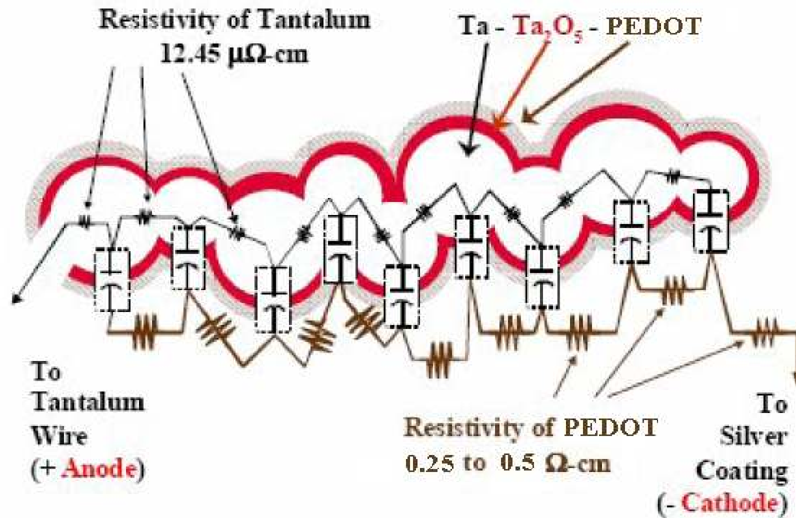

Fig. 3.6. Distributed RC network model of the capacitor [26].

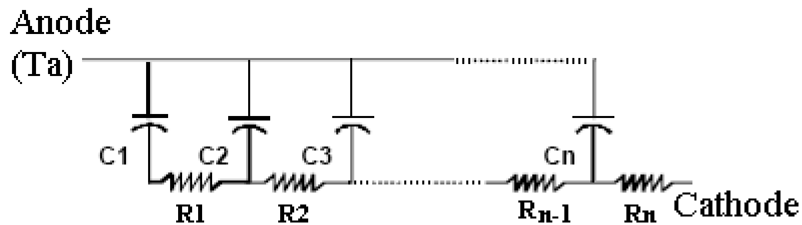

Fig. 3.7. Simplified distributed RC model. (Adapted from [26])

This RC ladder effect causes the capacitance to roll off at higher frequencies as shown in Fig. 3.8. As the RC ladder effect in polymer Ta capacitors is low, the capacitance roll-off begins at a higher frequency in comparison to the tantalum MnO_2 capacitors, making the tantalum-polymer capacitor more suitable for high frequency applications.

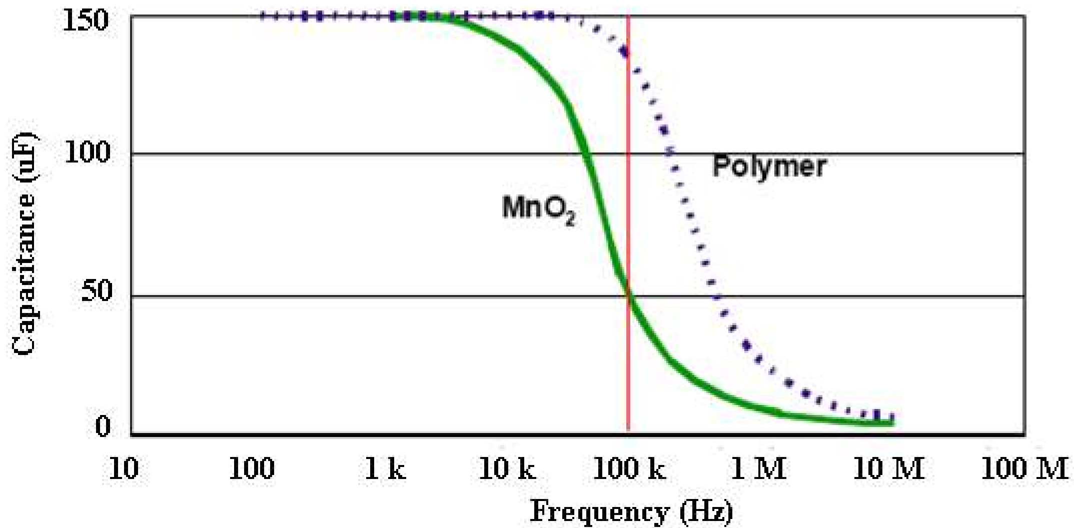

Fig. 3.8. Capacitance roll-off in MnO_2 and Polymer Ta capacitors [26].

Another attractive feature of the polymer Ta capacitor is its self-healing or electrical conditioning mechanism by which it heals any macroscopic defects that were created during its formation. This self-healing mechanism is explained by two theories. The first one attributes it to the evaporation of the PEDOT due to the excessive heat generated from the large fault current flowing through the dielectric at a defect site, which is illustrated in Fig. 3.9. This evaporation isolates the defect site from the capacitor system and prevents further current flow. Another explanation is that the polymer's resistivity is proportional to the oxygen level within it, which increases due to the movement of oxygen from the dielectric into the PEDOT, owing to the excess heat that is generated by the fault current. This high resistivity of the PEDOT adjacent to the defect site effectively limits the current flow through the defect [28]. Both these theories predict

that the self-healing mechanism increases the reliability of capacitors and makes it possible to manufacture reliable capacitors using simple processing techniques.

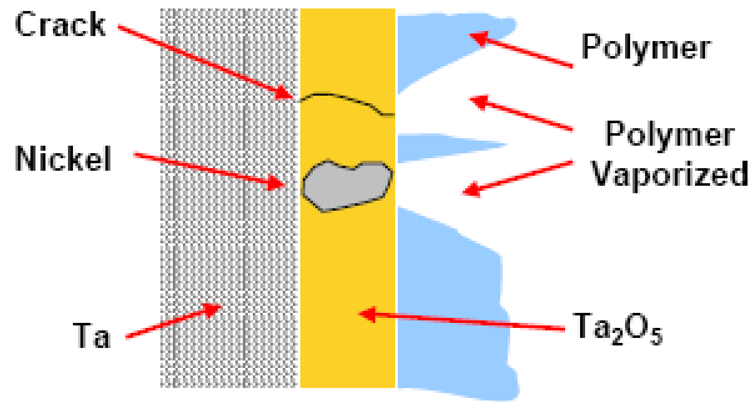

Fig. 3.9. Electrical Conditioning of the polymer Ta capacitor [10].

Other factors that improve the polymer Ta capacitor's reliability are lower process-induced stresses and the absence of the burning failure mechanism. There are lower process-induced stresses because PEDOT is a soft and flexible material and can thus adjust to physical forces that are created during the capacitor fabrication without cracking. Moreover, the polymer deposition process involves drying only at room temperatures, which further decreases the possibility of creating crack like faults [13]. Additionally, PEDOT does not contain enough oxygen to fuel the ignition failure mechanism that is common in MnO_2 based capacitors, so that the polymer capacitors can be safely used in sensitive environments where an ignition needs to be avoided at all costs [13].

To evaluate the possibility of an ignited failure, tests were conducted on identical polymer and MnO_2 based capacitors during which they were all biased at reverse polarity

with twice their rated voltage using a power supply that could deliver up to 20 Amps. Biasing at such a high reverse polarity is a sure way to significantly increase the leakage current in the capacitor and cause it to fail immediately. The results showed that all MnO_2 based capacitors failed and ignited while none of the polymer parts ignited, although they were damaged by the reverse polarity applied [26]. In terms of the cost involved, although the polymer as a raw material is more expensive than MnO_2, the polymer deposition process is cheaper than that of MnO_2 [1].

The biggest single drawback of using the polymer cathode was a reduction in the working voltage of the tantalum-polymer capacitor in comparison to that of the tantalum-MnO_2 capacitor. Until 2008, manufactured polymer Ta capacitors were of the *in situ* type and it was not possible to obtain a working voltage higher than 20 V. Using the pre-polymerized method of polymer deposition, it is now possible to manufacture tantalum-polymer capacitors with higher working voltages [28, 29]. The *in situ* capacitor and the pre-poly capacitor are essentially the same, with the exception that their polymeric cathode is deposited with a different method; however, this increased the maximum working voltage that could be obtained with a polymer capacitor. It has been observed that the *in situ* capacitor has a significantly higher leakage current than the pre-poly capacitor [30]. In Fig. 3.9, the leakage current in the *in situ* and the pre-poly capacitors is shown as a function of the applied dc voltage. At 25 V, the *in situ* capacitor conducts approximately 2 nA/cm^2, while the pre-poly capacitor conducts only 20 fA/cm^2. From Fig. 3.10, diode like I-V characteristics can be observed in the pre-poly capacitor. At normal bias, i.e., a positive bias applied to its anode with respect to its cathode, the

current is low; but when reverse biased, the current increases drastically. This high leakage current, at a negative bias, makes Ta capacitors unsuitable for operation in the negative bias regime; it is thus referred to as a polar capacitor.

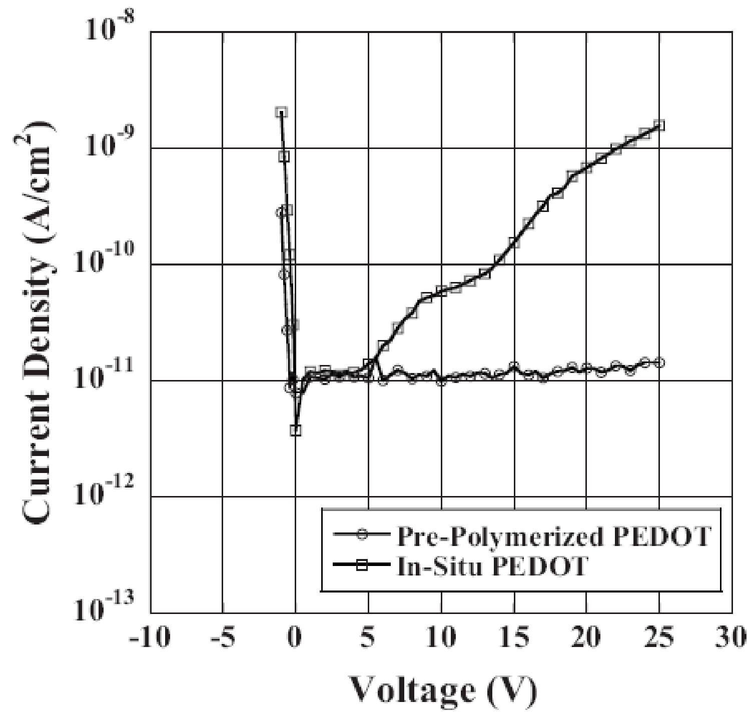

Fig. 3.10. Variation of leakage current in *In situ* and Pre-poly capacitors [30].

It is theorized that the lower leakage current in the pre-poly capacitors gives rise to its high breakdown voltage. Because of this, they are able to work reliably at higher voltages when compared to the *in situ* type [31]. Hence, the pre-polymerized polymer deposition technique is used to manufacture high voltage polymer Ta capacitors. In early 2009, the first polymer Ta capacitor was manufactured which had a working voltage of 35 V, and capacitors with a working voltage up to 75 V are undergoing reliability and life testing. Increasing the capacitor's maximum working voltage is necessary to enable their

use in applications that require capacitors with both high working voltage and low ESR, this requires a good understanding of the leakage and the breakdown mechanism in the capacitor. To analyze these complicated capacitors, it is often helpful to consider them as classical Metal-Insulator-Semiconductor (MIS) devices because of the inherent similarities between them [30].

3.4 Modeling Polymer Tantalum Capacitors as MIS Devices

The polymer Ta capacitor is composed of numerous spherical particles of tantalum covered with a layer of Ta_2O_5 and subsequently with a conducting polymer. This complicated structure can be represented as a network of interconnected metal-insulator-polymer structures as shown in Fig 3.11(a). To keep the device geometry simple, and to have similarity with standard microelectronic MIS devices, the capacitor's metal-insulator-polymer structure is assumed to be flat, even though in reality it is spherical, and the polymer is treated as a moderately doped semiconducting material [27]. This geometrical simplification is shown in Fig 3.11(b) and (c). The spherical structure of individual particles inside the capacitor is shown to enhance the existing electric field and preliminary results indicate that there is a change in the magnitude of leakage current because of the curvature of the structure [32]. However, these are second-order effects and can be safely ignored because they do not change the fundamental leakage mechanism that causes the capacitor to break down.

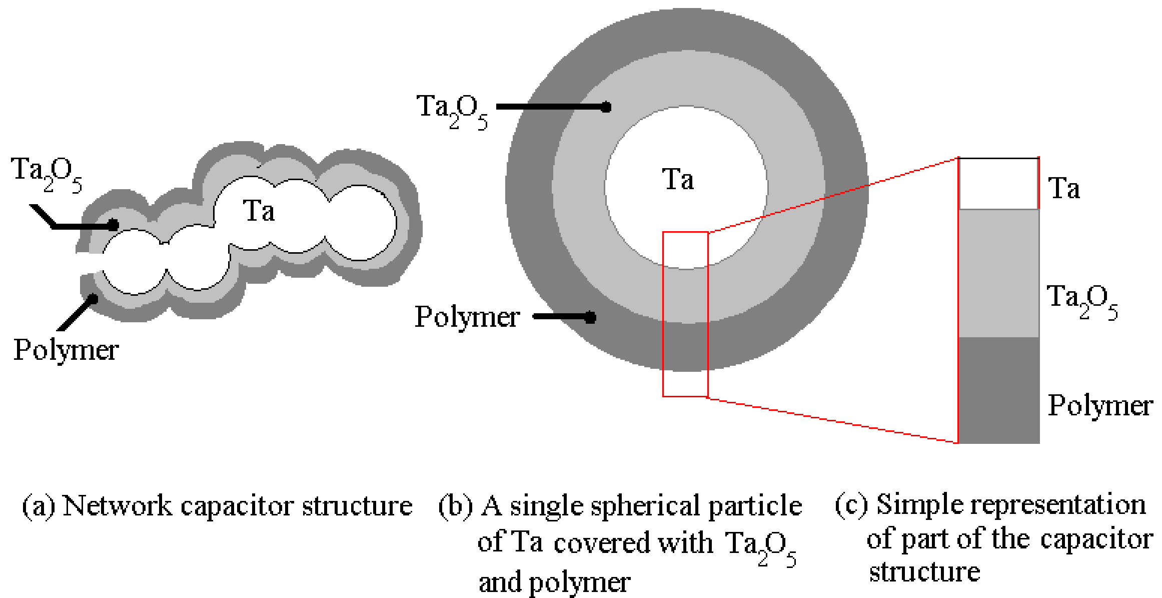

Fig. 3.11. Simplified capacitor structure for analysis

Many characteristics of standard MIS structures, such as capacitance as a function of an applied voltage (C-V) curves, and electronic band diagram based models are already well documented. In this research, we will treat the polymer Ta capacitor as a single flat MIS structure with capacitance, oxide thickness, and area equivalent to that of the actual fabricated capacitor.

Out of the three functional parts of the capacitor, the dielectric and the interface between the dielectric and the electrodes play the most important role in limiting the leakage current because the dielectric is the only insulator in the capacitor system. Hence, the leakage current, and consequently the breakdown voltage of the capacitor is fundamentally dependent on the dielectric and its interaction with the electrodes.

CHAPTER FOUR

BREAKDOWN PHENOMENON AND LEAKAGE MECHANISMS

4.1 Breakdown Phenomenon in Dielectrics

Dielectric breakdown phenomenon is the common cause of capacitor breakdown at high voltages, during which a conducting path is formed throughout the dielectric, resulting in a sudden increase in the current flowing through it. This breakdown often damages the dielectric, effectively changing it from an insulator into a conductor.

Until the 1950s, this breakdown was theorized to be initiated due to a variety of causes. A dominant cause is thermal runaway, during which the dielectric leakage produces heat, causing a further increase in the leakage, resulting in further heating. This cycle results because of the inability of the material system to remove heat at a sufficiently high rate. Another dominant cause is the Avalanche effect, during which electrons acquire enough energy from the field to ionize atoms, resulting in the creation of more electrons, thus increasing the current; this cycle continues until the dielectric breaks down. This effect is predominant in crystalline structures in which the probability of electrons losing energy by interacting with lattice imperfections is low. Other causes for breakdown include material flaws in the dielectric such as cracks, pinholes, or excessive surface roughness; the electromechanical collapse of the dielectric due to the Coulombic attraction between the electrodes; and the formation of a conductive gaseous channel in the dielectric [5, 33, 34].

However, since the 1960s, modern physics has attributed dielectric breakdown to a continuous wear-out process by which the dielectric is slowly degraded by applied

voltage stresses due to the generation of traps. These traps, a type of defect, are created either by the injection of electrons and holes from the electrodes or during dielectric film growth when impurities find their way into the material. The rate of trap generation is shown to be dependent on the electric field in the dielectric. Other possible factors that influence trap generation are hydrogen ions, free holes and electrons, and oxide currents, which cause internal bonds to break producing a trap [35-38]. No matter how the traps are generated, they degrade the dielectric by creating Stress Induced Leakage Currents (SILCs), which result from electrons tunneling in and out of the traps, a phenomenon referred to as a Trap Assisted Tunneling. Increasing SILCs raise the heat dissipated in the oxide, ultimately leading to breakdown.

These traps in the dielectric increase the local current density and the local heat generation, triggering thermal runaways and dielectric breakdowns [39]. These breakdowns may be destructive or non-destructive depending on the energy, given by $\frac{1}{2}CV^2$, stored in the dielectric system, which is essentially a capacitor, and the rate of discharge of this energy [40]. The energy stored in the capacitor depends on the oxide thickness, its surface area, and the applied voltage, while the rate of the energy discharge depends on the impedance of the complete measurement system through which the energy discharges. Prior to a destructive breakdown, many non-destructive ones, referred to as soft-breakdowns, can be observed, primarily in thin dielectric devices, because the energy stored in them is low. During a soft breakdown, the dielectric at the local hot spot melts and evaporates, causing the defect site to be open-circuited preventing further current flow. The dielectric layer is then recharged through the power supply and it

regains its dissipated energy [41]. On the other hand, a destructive breakdown results in the establishment of a permanent conducting path between the two electrodes, resulting in permanent damage. Research suggests that the magnitude of current flowing in the dielectric prior to breakdown is a strong indication of the probability to break down, this current being referred to as a pre-breakdown current. As this pre-breakdown current increases, the chance of dielectric breakdown and thus damage increases [31]. However, the underlying reason for the pre-breakdown current is the presence of traps in the dielectric.

The formation of these traps leading to a conductive path in the oxide is illustrated in Fig. 4.1; this conductive path carries the electrons from one electrode to the other, thus generating heat and resulting in breakdown. In this figure, the oxide region is sandwiched between the two electrodes, a necessity for making electrical measurements on the oxide. Part (a) of the figure illustrates the oxide layer containing intrinsic traps just after it is grown and (b) illustrates the oxide after the generation of traps due to the device being stressed by the application of a voltage. In Part (c), the number of defects has further increased, forming a conducting path between the electrodes resulting in a non-destructive breakdown that causes the existing defect path to be open circuited as shown in (d). As the device is stressed further, another conductive path is formed as shown in Part (e), leading to break down as shown in Part (f). This process continues until a final destructive breakdown occurs.

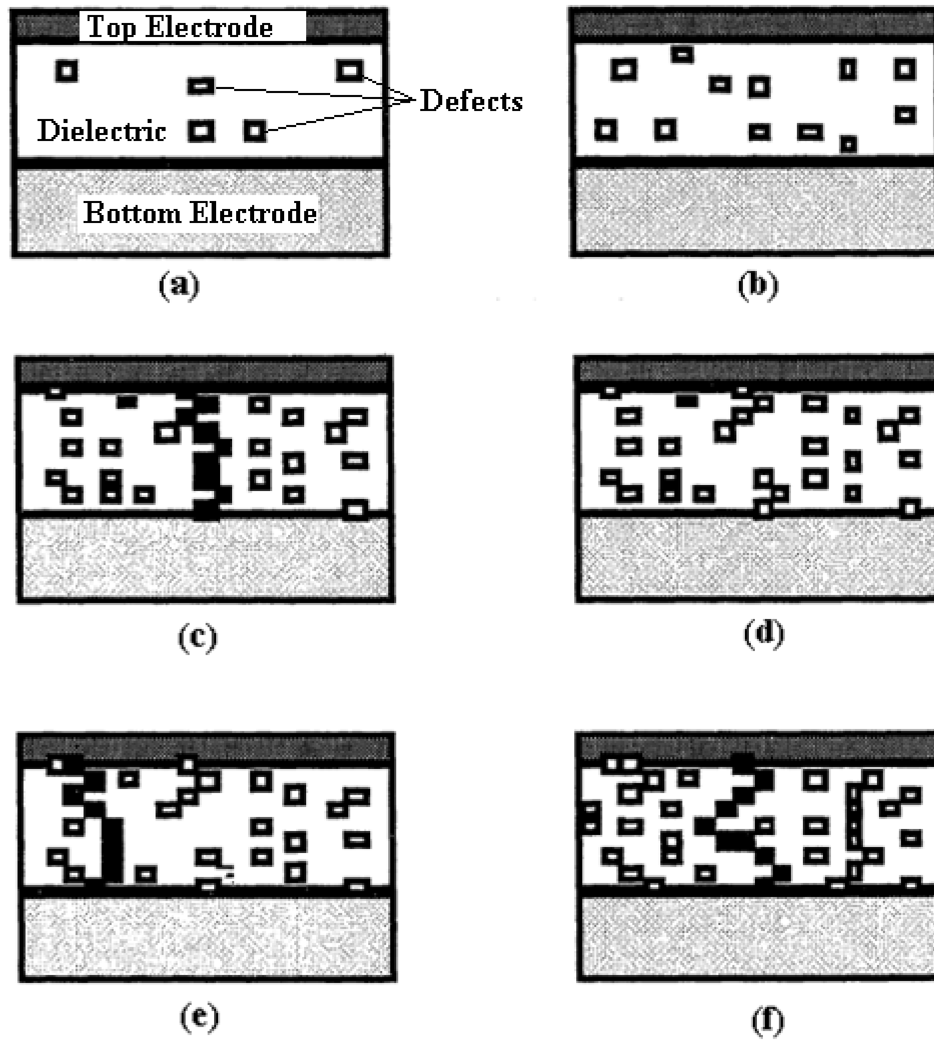

Fig. 4.1. Generation of traps leading to breakdown. (Adapted from [39])

The trap generation and subsequent breakdown have been modeled using a percolation theory suggesting that defects are generated at random locations, a breakdown occurring when they form a complete path through the oxide [42, 43]. Although this theory suggests the oxide breakdown occurs due to the traps generated

during high voltage stresses, it applies only to near perfect dielectrics, those free of macro defects. In these near-perfect dielectrics, the breakdown generally occurs near a particular electric field strength, referred to as the material's dielectric strength. Because the breakdown is a result of randomly generated defects, a material's dielectric strength is not a fixed value, but rather an approximated one [44].

The dielectric strength for Ta_2O_5, the dielectric used in all Ta capacitors, is estimated to be between 8 MV/cm and 10 MV/cm, which means that applying approximately 80 V causes the breakdown of a 100 nm thick layer of this oxide [31]. Dielectric strength is expressed as the amount of voltage per unit thickness, implying a higher theoretical breakdown voltage for a dielectric film of greater thickness. However, this relationship is not always accurate in practice because of such imperfections in the dielectrics as inclusions, sharp points, manufacturing defects, and the presence of impurities, all of which increase the pre-breakdown current and thus the probability of breakdown at a lower voltage [45, 46]. In ideal dielectrics, the breakdown voltage varies linearly with dielectric thickness, however, for practical dielectrics, the breakdown strength is found to decrease with an increase in dielectric thickness [47]. For high quality oxides used in the microelectronics industry in the past four decades, the breakdown voltage has been found to vary linearly with thickness over a limited range as shown in Fig. 4.2, suggesting the possibility of achieving a high breakdown voltage using a sufficiently thick dielectric of high quality [39]. For example, a breakdown voltage of 300 V was estimated for a 700 nm thick oxide of aluminum sandwiched between aluminum electrodes [39]. Since the dielectric layer is the key insulating component in

the capacitor affecting its BDV, the thicker the layer, the higher is the BDV. A high breakdown voltage is important in high voltage capacitors, which are expected to work reliably in the range of 100-200 V.

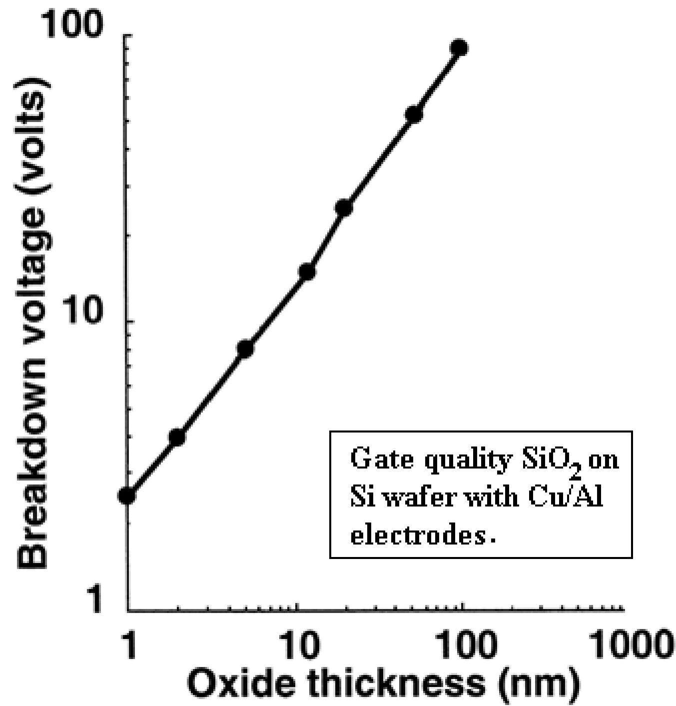

Fig. 4.2. Variation of BDV in SiO_2 films with its thickness. (Adapted from [39])

4.2 Dielectric Breakdown Phenomenon in Tantalum Capacitors

Once the dielectric layer breaks down, the tantalum capacitor then begins to conduct dc current, losing its capacitive property, and behaving more like a resistor. Growing a thicker layer of dielectric helps to achieve a higher BDV; however, this method works only up to a certain point. For wet tantalum capacitor, past research has

found that it is possible to obtain a maximum BDV of 210 V using a dielectric layer of thickness 510 nm. For improving the capacitor's electrical performance, when the cathode material was changed to MnO_2 in the 1950s, the maximum BDV of the Ta capacitor reduced to 150 V. In the 1990s, the maximum BDV decreased further to 50 V, when the cathode material was replaced with a polymer in the *in situ* polymer Ta capacitors. In the late 2000s, changing the method of polymer deposition to a pre-polymerized method resulted in a pre-poly capacitor with a BDV of 225 V. This significant increase in BDV led to the development of high voltage polymer Ta capacitors; however, the reason for this increase is not fully understood.

The comparison of the relationship between the dielectric thickness and the BDV for the ideal case and for the case of real Ta capacitors can be seen in Fig. 4.3. From this figure, it can be observed that the BDV of all tantalum capacitors initially increases significantly with increasing dielectric thickness until at a particular thickness, after which the BDV begins to roll-off. Its culmination, the point at which increasing thickness does not increase the BDV, is referred to as the saturation of the BDV. The BDV of *in situ* type and MnO_2 type capacitors clearly saturates; however, the BDV for the capacitor employing pre-polymerized cathodes is not yet saturated even with a 700 nm thick oxide. Although, the BDV versus thickness curve is increasing, it has deviated from the ideal linear curve. Since pre-poly capacitors with dielectrics of thicknesses greater than 700 nm have not yet been fabricated, their ultimate BDV is unknown.

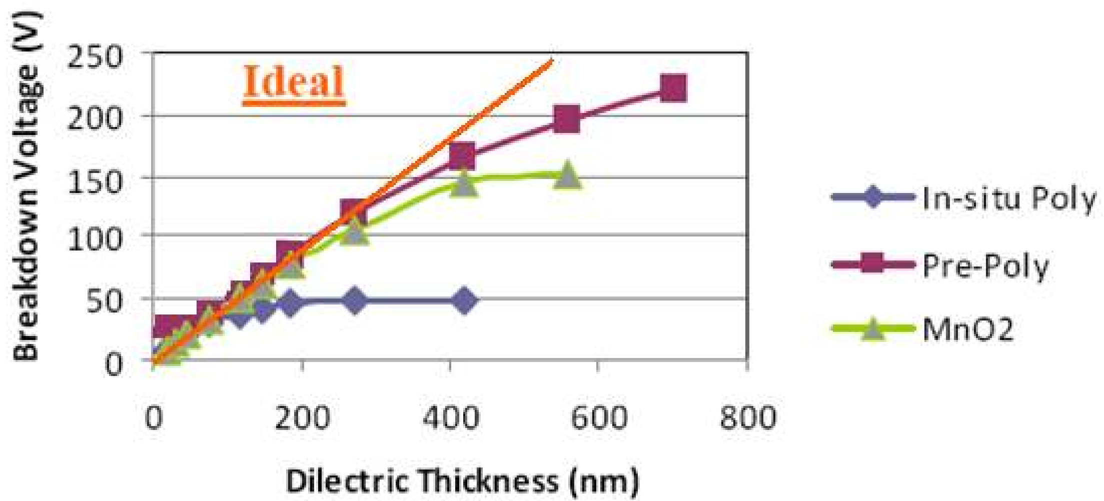

Fig. 4.3. Dependence of Breakdown voltage on dielectric thickness in Ta capacitors [48].

The early saturation of BDV in *in situ* capacitors in comparison to the pre-poly capacitors may be a result of the higher pre-breakdown current measured in *in situ* devices [30]. By examining and modeling this pre-breakdown current, it is possible to understand the fundamental dielectric leakage mechanisms that give rise to the current leading to the early breakdown in the *in situ* capacitors.

A dielectric leakage mechanism, or a combination of several, provides a physical explanation of the origin of the current that flows through the dielectric, even though it is typically considered an insulator. Common dielectric leakage mechanisms are the Poole-Frenkel Effect, Schottky Effect, Space Charge Limited Conduction, Tunneling, and Fowler-Nordheim Tunneling.

4.3 Poole-Frenkel Mechanism

The Poole-Frenkel (PF) Effect involves thermal emission of charge carriers out of coulombic traps in the bulk of a dielectric or a semiconductor, enhanced by the application of an external field, which aids the electron to escape from the trap. For the field-enhanced thermal emission of electrons to occur, coulombic traps must be neutral when filled with an electron, and positively charged when the electron is emitted [49]. This effect is generally observed in amorphous materials and it is a consequence of the existing traps in the dielectric [50]. Because the PF Effect depends on the availability of traps in the bulk of the dielectric, it is referred to as a bulk-limited mechanism. When an electric field is applied, the potential barrier on one side of the coulombic trap is reduced increasing the thermal emission rate of electrons from the trap. The Poole-Frenkel current density is given by,

$$J = C\,\mathcal{E}\,\exp\left(-\frac{q\,\Phi - \beta\sqrt{\mathcal{E}}}{\xi kT}\right) \tag{4.1}$$

where C is a proportionality constant, $\mathcal{E}$ the electric field, $q\Phi$ the ionization potential of the trap, β, referred to as the PF constant, is a material constant defined as $\beta = \sqrt{\frac{q^3}{\pi\epsilon_0\epsilon_r}}$, ξ the slope factor of the PF Effect, T the absolute temperature, and *k* is the Boltzmann's constant. By rearranging Eq. 4.1 and taking the natural logarithm on both sides, Eq. 4.1 can be written as,

$$ln\left(\frac{J}{\mathcal{E}}\right) = \frac{\beta}{\xi kT}\sqrt{\mathcal{E}} + \left(\ln C - \frac{q\Phi}{\xi kT}\right) \quad (4.2)$$

A plot of $ln\left(\frac{J}{\mathcal{E}}\right)$ versus $\sqrt{\mathcal{E}}$, known as the PF Plot, should be linear if the PF Effect is the dominant conduction mechanism. The slope of a PF plot, M, is given by $\beta/_{\xi kT}$; ξ can vary between 1 and 2 to account for acceptor compensation in the material [49]. ξ=1 corresponds to heavy acceptor compensation and ξ=2 corresponding to no compensation. The linearity of Eq. 4.2 is the first test used to determine whether the dominant conduction mechanism could be due to the PF Effect. [51, 52]. The other criteria needing to be satisfied will be discussed in Chapter 6.

4.4 Schottky Effect

The Schottky Effect is the image force induced lowering of the potential energy for charge carrier emission when an electric field is applied [53]. Although it closely resembles the Poole-Frenkel Effect, it differs in two important aspects: it depends on the mobile image charge created by an electron escaping from a metal surface, and it is controlled by the interface barriers between a metal electrode and the dielectric, meaning the Schottky Effect is an electrode limited process. The current density due to the Schottky Effect is given by the Richardson-Dushman Equation, which is given by,

$$J = A^{*}T^{2} exp\left(- \frac{q\Phi - \frac{1}{2}\beta\sqrt{\mathcal{E}}}{kT} \right) \tag{4.3}$$

where A^{*} is the Richardson constant that depends on the effective mass of the electrons in the material, T the absolute temperature, Φ the barrier height, k is the Boltzmann's constant and β, a material constant given as $\beta = \sqrt{\frac{q^{3}}{\pi\epsilon_{0}\epsilon_{r}}}$. This value of β is equal to the β mentioned previously as the PF constant. Rearranging this equation and taking the natural logarithm on both sides, yields,

$$\ln(J) = \frac{1}{2kT}\beta\sqrt{\mathcal{E}} + \left(\ln(A^{*}T^{2}) - \frac{q\Phi}{kT} \right) \tag{4.3}$$

A plot of $\ln(J)$ versus $\sqrt{\mathcal{E}}$, known as a Schottky Plot, will be linear if the Schottky Effect is the dominant conduction mechanism, the slope of the linear fit being $\frac{\beta}{2kT}$. The slope of this characteristic plot will be same as the PF effect characteristic plot, if the value of $\xi = 2$ in the PF equation. As a result, other methods to determine the precise current conduction mechanisms such as evaluating its dependence on temperature are needed [54].

4.5 Space-Charge-Limited Conduction Mechanism

Space-Charge-Limited Conduction (SCLC) is a mechanism in which the current is carried by electrons and holes injected into the insulator from the electrodes. If there

are compensating charges present in the insulator, the injected carrier combines with them; otherwise, it remains as a free carrier. At low voltages and high temperatures, the current is carried by electrons hopping from one state to the other [53]. In the absence of traps in the dielectric, the current is expressed by the Mott-Gurney Law,

$$J = \frac{9}{8}\mu\epsilon_0\epsilon_r\frac{V^2}{L^3} \tag{4.4}$$

where μ is the free carrier mobility, ϵ_0 and ϵ_r the permittivity of free space and the relative permittivity of the material respectively, V is the applied voltage and L is the thickness of the dielectric. The presence of traps modifies this equation depending on their distribution and nature. However, under all conditions, the current is proportional to V^n, where n is an integer or fraction, its value determined by the distribution of the traps. Plotting the current versus voltage on a log-log plot, results in a linear curve of slope n, showing the probability of the conduction mechanism being dominated by SCLC [55].

4.6 Tunneling Mechanism

Tunneling occurs when the field ionizes trapped electrons into the insulator's conduction band or when electrons tunnel through a trapezoidal electronic barrier between the electrodes. In the second case, when a sufficiently high voltage is applied across a dielectric, there is a finite probability that an electron can quantum mechanically tunnel through the oxide. This probability can be written as, [53]

$$T \approx \exp(-\alpha_t \Phi_t^{0.5} d) \tag{4.5}$$

where α_t is a fraction that approaches 1 when the electron's effective mass in the insulator equals the free electron mass, Φ_t is the barrier height between the insulator and the electrode in volts, and d is the thickness of the insulator in Å. This tunneling probability is insignificant when the insulator thickness is greater than a few nanometers for typical barrier heights. The tunneling current due to field ionization can be expressed as,

$$J = C\, \mathcal{E}^2 \exp\left[-\frac{4\sqrt{2m^*}(q\Phi_b)^{\frac{3}{2}}}{3\hbar q \mathcal{E}}\right] \tag{4.6}$$

where C is a proportionality constant, $\mathcal{E}$ is the electric field, m* is the effective mass, Φ_b is the barrier height, and $\hbar$ is the reduced Plank's constant. This current is strongly dependent on the applied voltage; however, it is independent of the temperature [53]. According to Eq. 4.6, $\ln\left(J/\mathcal{E}^2\right)$ versus $1/\mathcal{E}$ should result in a linear plot if the dominant conduction mechanism is due to the tunneling or field emission.

4.7 Fowler-Nordheim Tunneling Mechanism

Fowler-Nordheim (FN) tunneling is similar to the direct tunneling process, except that the electrons tunnel through a triangular electronic barrier between the electrodes. The triangular barrier is the result of the application of a high voltage across the dielectric and is thinner than the classical trapezoidal barrier. The tunneling probability is higher because of the decreased barrier width. The equation governing FN tunneling is similar to that governing the field assisted tunneling, which can be empirically written as,

$$J = A\mathcal{E}^2 \exp\left(-\frac{B}{\mathcal{E}}\right) \quad (4.7)$$

where

$$A = \frac{m}{m^*}\frac{q^3}{8\pi h \Phi_b}$$

$$B = \frac{8\pi}{3}\left(\frac{2m^*}{h^2}\right)^{0.5}\frac{\Phi_b{}^{0.5}}{q}$$

h, the Plank's constant, m the electron mass, and all other symbols have their usual meanings [56].

From Eq. 4.7 it can be observed that if FN tunneling is the dominating mechanism, then a plot of $\ln\left({}^{J}/_{\mathcal{E}^2}\right)$ versus ${}^{1}/_{\mathcal{E}}$ should be linear; this is the same criterion used to test for the presence of the field ionization tunneling process, which occurs majorly in ultra thin oxides [57].

4.8 Activation Energy of a Leakage Mechanism

Certain dielectric leakage mechanisms, such as the PF effect and the Schottky Effect, which are dependent on the sample's temperature, are thermally activated processes, which are represented by a general equation of the form:

$$Y = Y_0 \exp\left(-\frac{E_a}{kT}\right) \tag{4.8}$$

where E_a is referred to as the activation energy of the process, Y is the process rate, Y_0 the pre-exponential factor, T the absolute temperature, and k the Boltzmann's constant. Taking the natural logarithm of Eq. 4.8, the following equation is obtained,

$$ln(Y) = -\frac{E_a}{kT} + ln(Y_0) \tag{4.9}$$

For a thermal process, a plot of $ln(Y)$ versus $1/T$, referred to as an Arrhenius plot, results in a linear fit, the slope of which is $-E_a/k$. From the slope, it is possible to determine the value of the activation energy, as the value of k is known. This activation energy of the process controls the rate of change of Y with temperature. By measuring the current at a constant voltage at different temperatures, it is possible to extract the activation energy of the leakage mechanism. This extracted value represents the depth of traps in the Poole-Frenkel Effect or the interface barrier height in the Schottky Effect.

Lower activation energy signifies a lower barrier to current conduction in the insulator and an increased chance of breakdown.

4.9 Leakage Mechanisms Observed in Tantalum Pentoxide Structures

The mechanism that causes current leakage through a dielectric not only depends on the nature of the material; the mechanism is also dependent on the electrodes, dielectric thickness, and the device fabrication process. The leakage current also depends on other factors such as the device annealing process and environmental conditions such as temperature and humidity affecting the measurement. These parameters and conditions should be taken into consideration while comparing the experimental results of the measurements on the Ta_2O_5, tabulated in Table I. Structures listed in this table are MIM/MIS based ones and they do not necessarily represent the complexities of a manufactured discrete capacitor. In Table, “Structure” refers to the layers of materials in the device. “Thickness” refers to the thickness of Ta_2O_5 in the structure and “Mechanism” refers to the dominant leakage mechanism and the electric field range it is applicable as determined by the authors mentioned in the “Ref.” column. Other details about the structure or measurements, which may be influence the leakage mechanism, are mentioned in the column titled “Deposition Process, Other Comments”. In the column titled “Mechanism”, PF stands for Poole-Frenkel mechanism, SE for Schottky Emission and FN for Fowler-Nordheim tunneling.

Table I. Leakage mechanisms observed in Ta_2O_5 devices.

	Structure	Thickness (nm)	Deposition Process / Other Comments	Mechanism	Ref.
1	$TiN/Ta_2O_5/TiN$	20-90	MOCVD	PF (1-4 MV/cm)	[58]
2	$TiN/Ta_2O_5/SiO_2/p\text{-}Si$	20-90	SiO_2 thickness = 2nm, MOCVD	PF (1-4 MV/cm)	[58]
3	$TiN/Ta_2O_5/SiN/Si$	10-20	MOCVD	FN (positive E) PF/SE (negative E)	[59]
4	$TiN/Ta_2O_5/TiN$	45	MOCVD	PF (6-20 MV/cm)	[60]
5	$Al/Ta_2O_5/Si$	26	RF Sputtering, Annealing	PF (0.4-1.2 MV/cm for as-deposited) SE (0.8-1.3 MV/cm after annealing)	[45]
6	$TaNx/Ta_2O_5/W\text{-}Al$	10-450	Anodization	PF (1-5MV/cm)	[61]
7	$Al/Ta_2O_5/Au$	35	RF Sputtering	PF (0.8-2 MV/cm)	[62]

As Table I shows, the dominant leakage mechanisms commonly observed in Ta_2O_5-based structures are due to the Poole-Frenkel Effect, the Schottky Effect, or the Fowler Nordheim tunneling. The associated thermal activation energy for a leakage mechanism in this dielectric is found to be between 0.2 and 0.8 eV [63-65]. If the leakage mechanism is dominated by the Poole-Frenkel Effect, the activation energy of the mechanism represents the shallowest defect or trap depth; however, if it is dominated by the Schottky Effect, this activation energy corresponds to the barrier height between the dielectric and one of the electrode [63, 64]. Leakage mechanisms controlled by a Tunneling mechanism are independent of temperature, apparent only when considering second order effects. To compare the leakage mechanism between *in situ* capacitors and pre-poly ones, the pre-breakdown currents in both need to be carefully measured and

modeled. The understanding of the leakage mechanism can also lead to reason for the earlier breakdown of the *in situ* capacitors than the pre-poly capacitors.

CHAPTER FIVE

ELECTRICAL CHARACTERIZATION TECHNIQUES FOR CAPACITORS

Capacitors can be electrically characterized by measuring their current versus voltage (I-V) and capacitance versus voltage (C-V) characteristics. I-V measurements, which are more frequently used in this research, were conducted on two types of capacitors – polymer Ta capacitors and flat MIM structures. In comparison to the discrete polymer Ta capacitors, flat MIM structures are simple, requiring minimal deviation from standard electrical characterization techniques; however, characterizing discrete polymer Ta capacitors requires special techniques that will be discussed in this section.

5.1 I-V Measurements

All current measurements at room temperature (300 ˚K) were conducted using a Keithley 4200 Semiconductor Characterization System. While the polymer Ta capacitors were held in the Keithley 8101 PIV Component Test Fixture, the flat samples were measured by placing them on a chuck in a probe station manufactured by Micromanipulator Co., Inc. (Carson City, NV).

5.1.1 Limiting Noise in I-V Measurements

The polymer Ta capacitors tested here have capacitances in the range of 10s of microfarads, which is larger than the maximum load capacitance specification of the Keithley measurement system, which is only 10 nF; hence, the measured results are filled with noise, resulting in oscillations. Fig 5.1 illustrates the results from an I-time

measurement performed using the Keithley SCS 4200 on the device under test (DUT). The resulting oscillations are due to the amplification of noise, which can be directly observed. In this figure, the highest current value is 1 μA, which is the current compliance level set during the measurement.

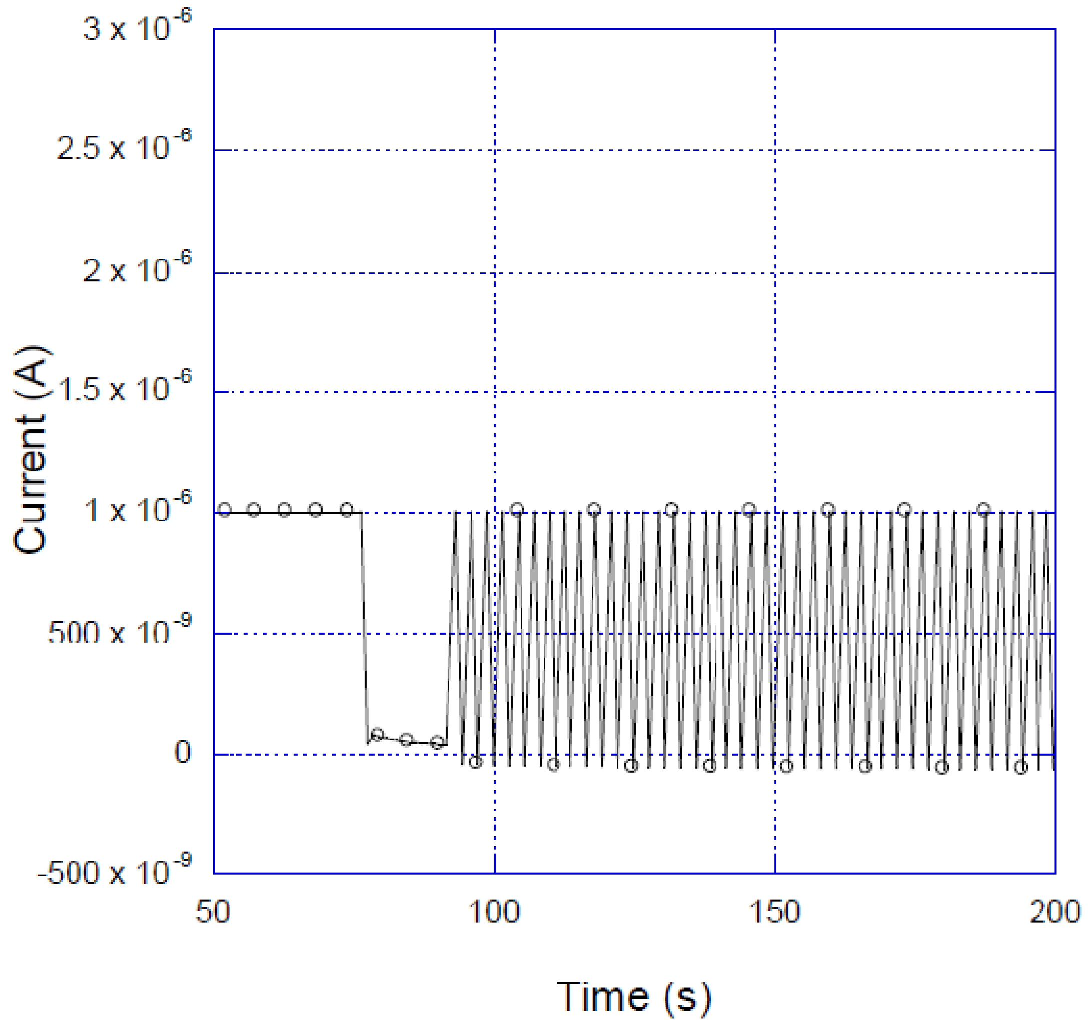

Fig. 5.1. I-time measurement result on a Ta polymer capacitor.

The reason for the large noise content that was observed in Fig 5.1 is illustrated in Fig. 5.2, which shows a simplified schematic of the measurement system, a feedback ammeter with its op-amp configured in the inverting mode [66].

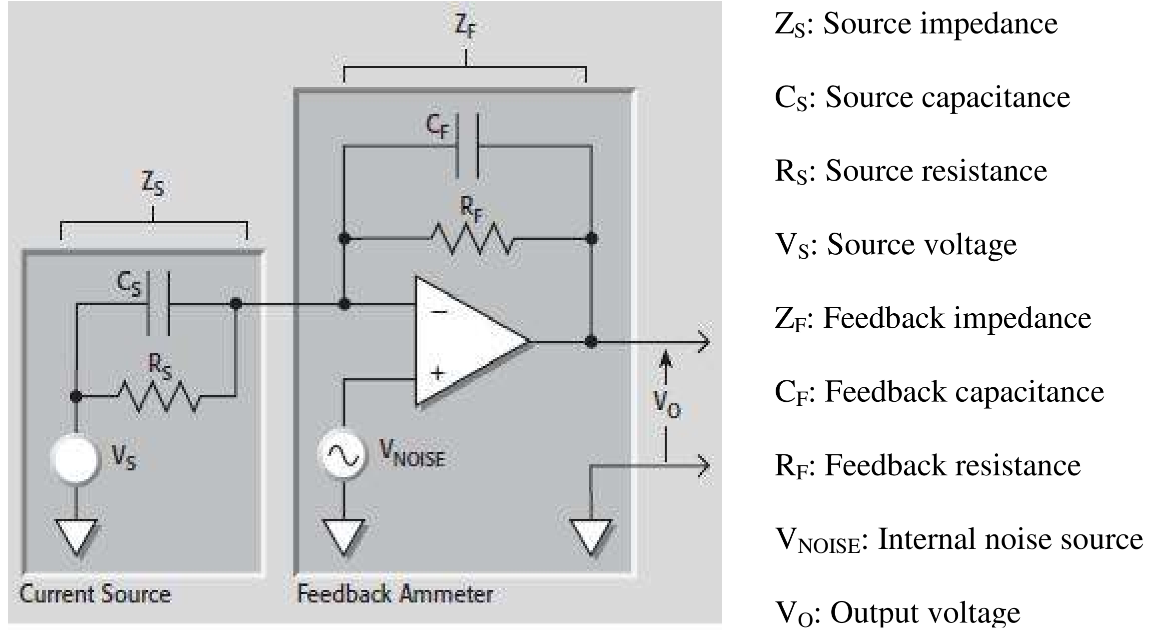

Z_S: Source impedance

C_S: Source capacitance

R_S: Source resistance

V_S: Source voltage

Z_F: Feedback impedance

C_F: Feedback capacitance

R_F: Feedback resistance

V_{NOISE}: Internal noise source

V_O: Output voltage

Fig. 5.2. Simplified schematic of the measurement system [66].

The output noise of this system obtained at V_O can be expressed as,

$$Output\ V_{NOISE} = Input\ V_{NOISE}\left(\frac{Z_F}{Z_S}\right) \tag{5.1}$$

$$Z_F = \frac{R_F}{\sqrt{(2\pi f R_F C_F)^2 + 1}} \tag{5.2}$$

$$Z_S = \frac{R_S}{\sqrt{(2\pi f R_S C_S)^2 + 1}} \tag{5.3}$$

As C_S in Eq. 5.3 increases, Z_S decreases, and the noise gain of the op-amp increases. This increase is the reason that measuring capacitors with a capacitance larger than that specified by the measurement equipment is problematic. To reduce noise gain, the source impedance, Z_S, needs to be increased. One method of achieving the increase is by adding a resistor R_N in series with the capacitor.

When introducing an external resistance into the measurement system, certain factors should be considered. Most importantly, adding this noise-limiting resistor, R_N, in series increases the voltage burden by a factor $V_B = I_{MEASURED} \text{ x } R_N$, meaning that the actual voltage across the DUT will be the applied voltage minus V_B. In this research, typical values of $I_{MEASURED}$ are between 1 nA and 250 nA when 25 V is applied across the capacitor. Assuming R_N to be 1 MΩ results in a voltage correction factor, V_B, of 0.25 V at the maximum, a value which is negligible compared to the applied 25 V. However negligible this voltage correction factor may be, it should be subtracted from the applied voltage in determining the actual voltage across the DUT.

Secondly, adding a series resistance also decreases the chance of device breakdown because the series resistance limits the current and thus, the energy that can be discharged during a possible breakdown. However, the capacitors being measured in this research were already aged and tested for breakdown by applying a voltage higher than their working voltage for 1-2 hours without the series resistor. If they were to break down, they would have been damaged during the aging process. Thus, because the voltage burden's effects can be accounted for and the capacitors were tested for

breakdown, no undesirable changes are assumed to be introduced into the measurement setup by adding the 1 MΩ noise-limiting resistor.

To choose an appropriate resistor for this research, different values of resistance, 1 kΩ, 10 kΩ, 100 kΩ, and 1 MΩ, were investigated. The 1 MΩ resistor was found to be optimal for reducing the noise while keeping the voltage burden sufficiently low. The noise exhibited while using the other three smaller resistors was significant enough to affect the accuracy of the measured results. When the noise-limiting resistor was added in series with the capacitor, noise was minimal, and the oscillations observed in Fig. 5.1 were absent. This is illustrated in Fig. 5.3, which shows the result from an I-time measurement on a Ta polymer capacitor with the 1 MΩ noise-limiting resistor. During this measurement, 15 V was applied across the capacitor and the resistor, which are in series and the current flowing in the circuit was sampled every second for approximately 25 minutes. The current can be observed to decay smoothly over time, after the voltage was applied.

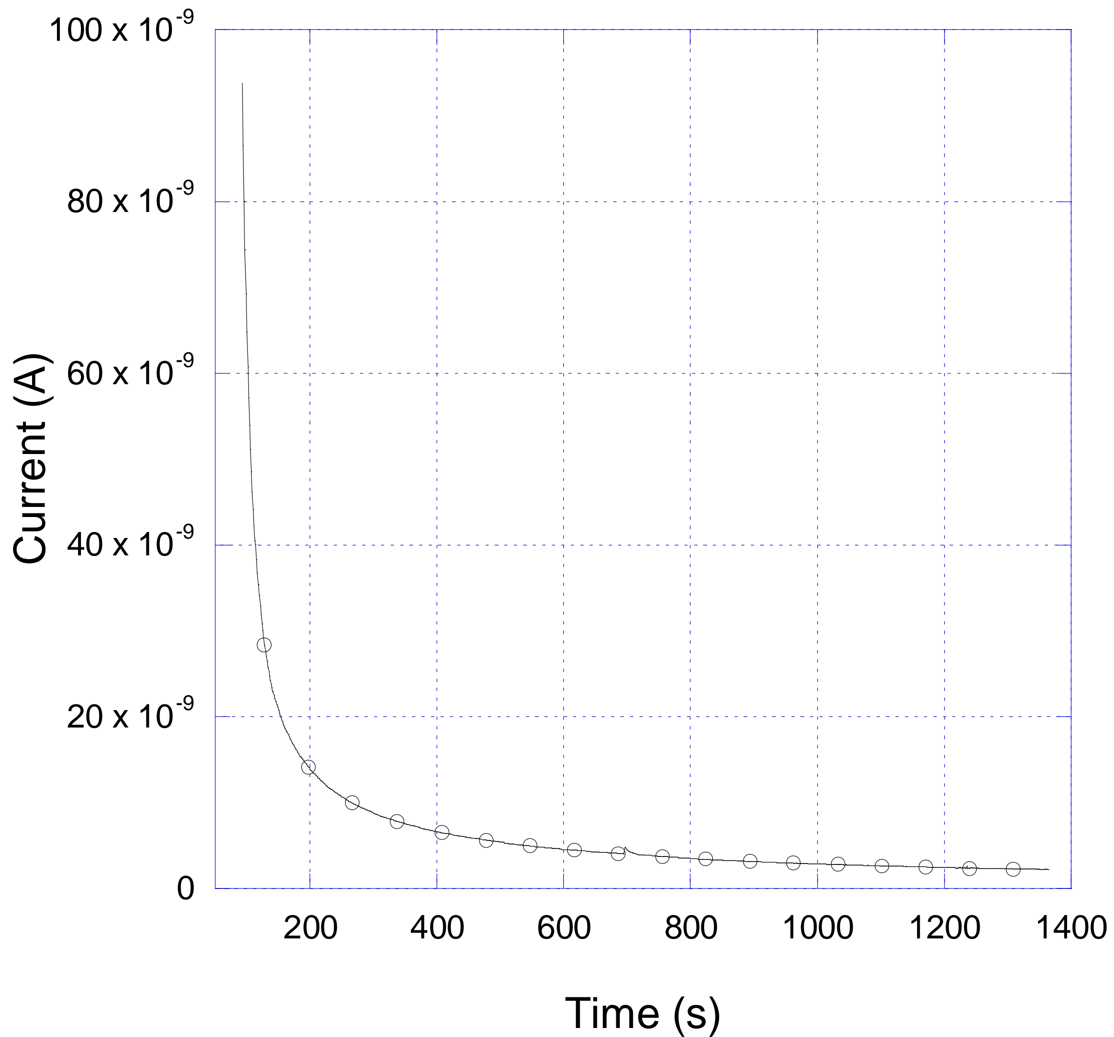

Fig. 5.3. I-time measurement result on polymer Ta capacitor with the series resistor.

5.1.2 Determining Time Delay required for I-V Measurements

With the measurement system set up to perform the I-V measurements, the next step is to examine the method to perform them. An I-V measurement involves the application of a voltage across a capacitor and measuring the resultant steady state current. This process needs to be repeated at different voltages to obtain the complete I-V

curve over a certain voltage range. To perform this measurement, a voltage sweep test is used to vary the voltage applied across the DUT in steps from the starting voltage to the ending voltage. The measured current is affected by the test parameters, the most important ones being the step size and the time delay between the steps. The step size is determined based on the I-V data resolution required. The delay should be experimentally determined using an I-time measurement, during which a constant voltage is applied across the capacitor while the leakage current is sampled continuously for several hours. When the current stops decaying significantly with time, the capacitor system is assumed to have reached steady state; the current measured at this state is referred to as the steady state current. If the current flowing through a capacitor at a constant voltage is observed to be increasing with time, rather than decaying, the dielectric is being progressively degraded by the applied voltage and the possibility of breakdown is high.

This current decay is a two stage process. Initially, when a voltage is applied across the capacitor, it creates a displacement current, ideally expressed as,

$$i = C\frac{dv}{dt} \tag{5.4}$$

where C is the capacitance and ${dv}/_{dt}$ the time rate of change of voltage across the capacitor. In practice, this current is lower because of the resistance in the capacitor-charging path. This displacement current decays over time as the capacitor becomes

charged to a voltage equal to the applied voltage, resulting in the term $\frac{dv}{dt}$ in Eq. 5.4 reducing to zero. This transient current can be expressed as a function of time by

$$i(t) = \frac{V_0}{R} e^{-t/RC} \tag{5.5}$$

where V_0 is the voltage applied across the capacitor, t the time after the voltage has been applied, and R is the series resistance in the capacitor charging circuit. In this research, the approximate values of C and R are 10 μF and 1 MΩ, the R being the noise-limiting resistor. Assuming the initial applied voltage, $V_{0,}$ to be 15 V, the displacement currents after 10, 100 and 175 seconds are 5.6 μA, 680 pA, and 0.4 pA respectively. Since the current measured is in the range of nanoamperes, it is desirable to wait for sufficient time after the application of the voltage until the displacement current decays three orders of magnitude lower than the nanoamperes range. This delay is approximately 175 seconds in the research reported here. The current decay measured and the current decay as calculated using Eq. 5.5 during the first 200 seconds after applying a voltage across the capacitor are shown in Fig. 5.4. The measured current can be seen to be in good agreement with the value of current calculated until about 100 seconds, after which the measured current decays towards a non-zero finite value, while the calculated current decays towards zero.

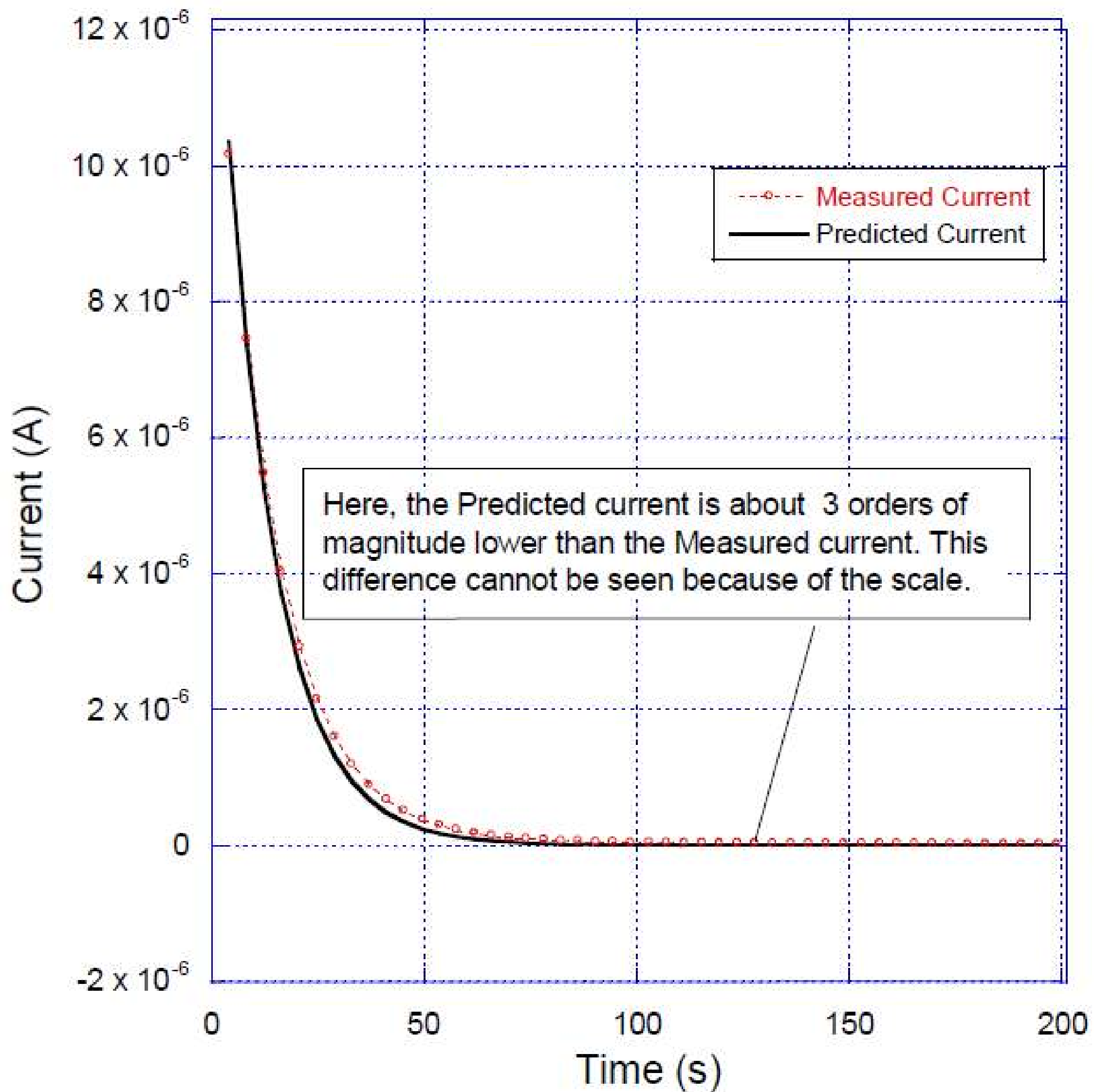

Fig. 5.4. Current decay in an *in situ* capacitor for the first 200 s. V_0 = 15 V.

After the displacement current has decayed away, the current flowing between the electrodes is due to electrons leaking through the dielectric from one electrode to the other and charge carriers moving along the surface of the capacitor which is in contact with the electrodes. The second component is generally negligible and to keep it so, the

capacitor's surface must be kept clean by handling the capacitor using tweezers. After the displacement current decays to zero, the first component, the leakage current dominates the measured current. This leakage current also decays to a non-zero finite value slowly, during which the capacitor reaches steady state. This is demonstrated in Fig. 5.5, which is an I-time measurement showing the current decay for about 5 hours from the 175th second. Even after 17000 seconds (4 h and 45 min) subsequent to applying the voltage, the dielectric leakage current continues to decrease; however, during the last 8000 seconds (2 h and 10 min), the current changes only from 2.6 nA to 2.4 nA, this difference is less than 10% of the final current, 2.4 nA, as illustrated in this Fig. 5.5. It would be ideal to wait for 5 hours between each voltage step, but obtaining an I-V curve from 2 V to 26 V using a wait time of 5 hours between each 2 V step will require 216000 seconds (60 h) of measurement time. To strike a balance between the measurement time required and the accuracy of the steady state current, a delay of 9000 seconds was selected while conducting most measurements. In addition, another factor to consider while applying voltages for long intervals across the capacitor is that stressing it at voltages near its breakdown voltage for long periods may expedite the breakdown process due to the creation of Stress Induced Leakage Currents [39].

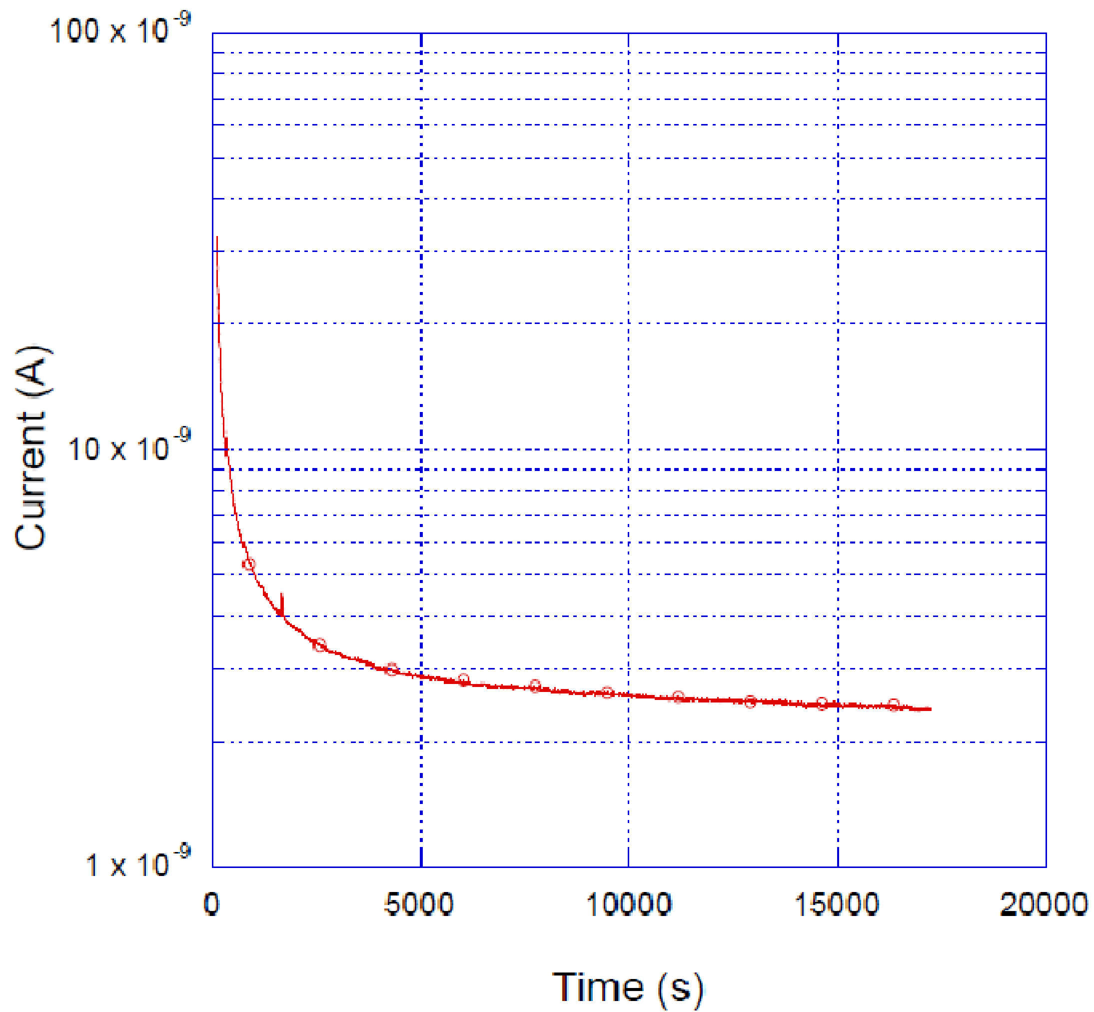

Fig. 5.5. Current decay in an *in situ* capacitor from t = 175 s to 17 ks. V_0 = 15 V.

Thus, from these I-time measurements, an optimal delay of 9000 seconds was chosen between voltage steps that range from 1 – 3 V, depending on the resolution required. However, the maximum delay allowed by the measurement equipment during a voltage sweep is only 1000 seconds; this requires performing I-time measurements at the required voltages and compiling the final value of current from each measurement into one I-V curve. This technique has already been reported in the literature [58, 62]. In this

research, the final value of current from each I-time measurement was obtained by averaging the last 5-10 % of the measured current readings in order to reduce chances of an error. A complete I-time measurement result at 15 V is shown in Fig. 5.6; the first 25 points, which would otherwise change the graph's scale, are not shown. During this experiment, current was sampled for 9000 seconds at every fourth second. Such I-time measurements conducted at 5 V, 6.5 V and so on up to 25 V resulted in the I-V curve shown in Fig. 5.7.

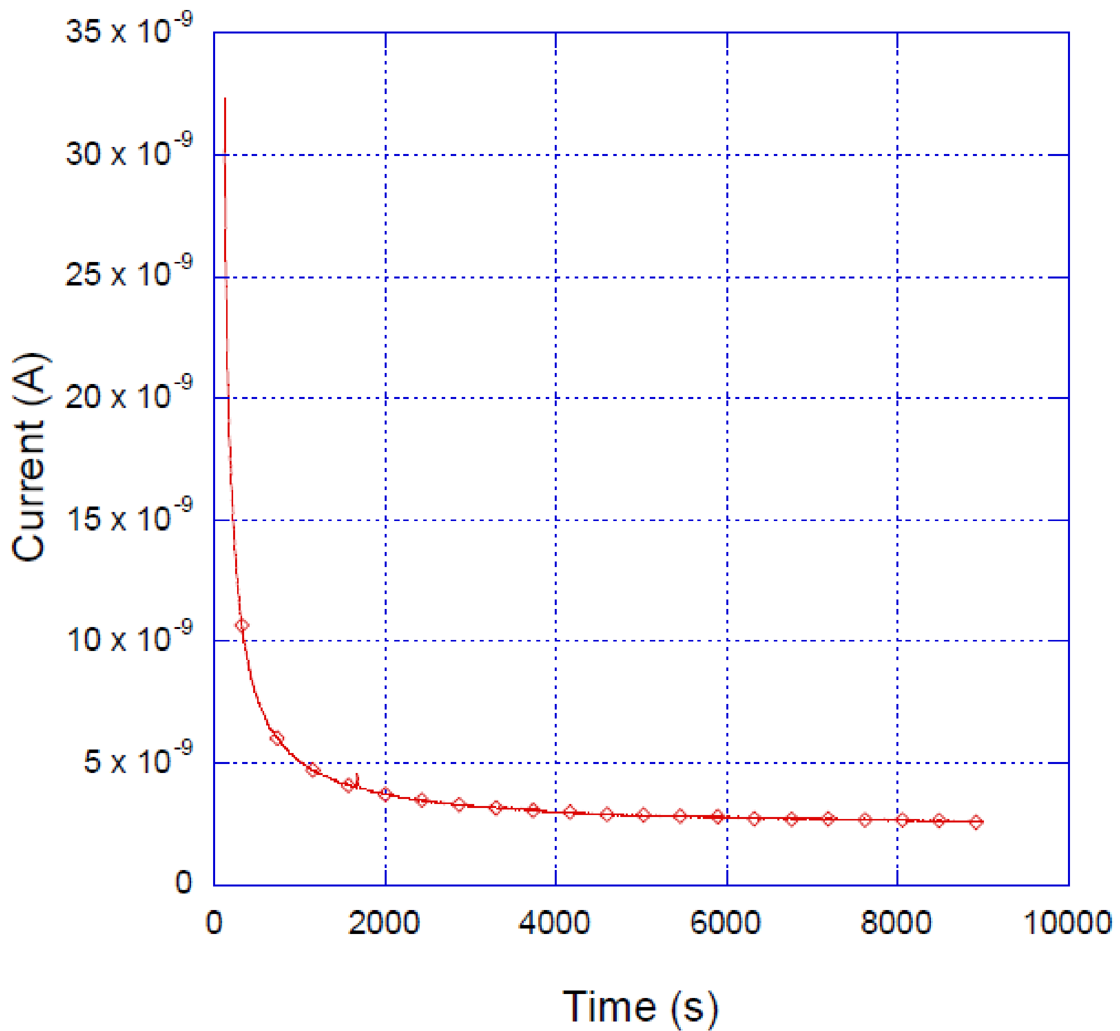

Fig. 5.6. I-time measurement results at 15 V on an *in situ* capacitor.

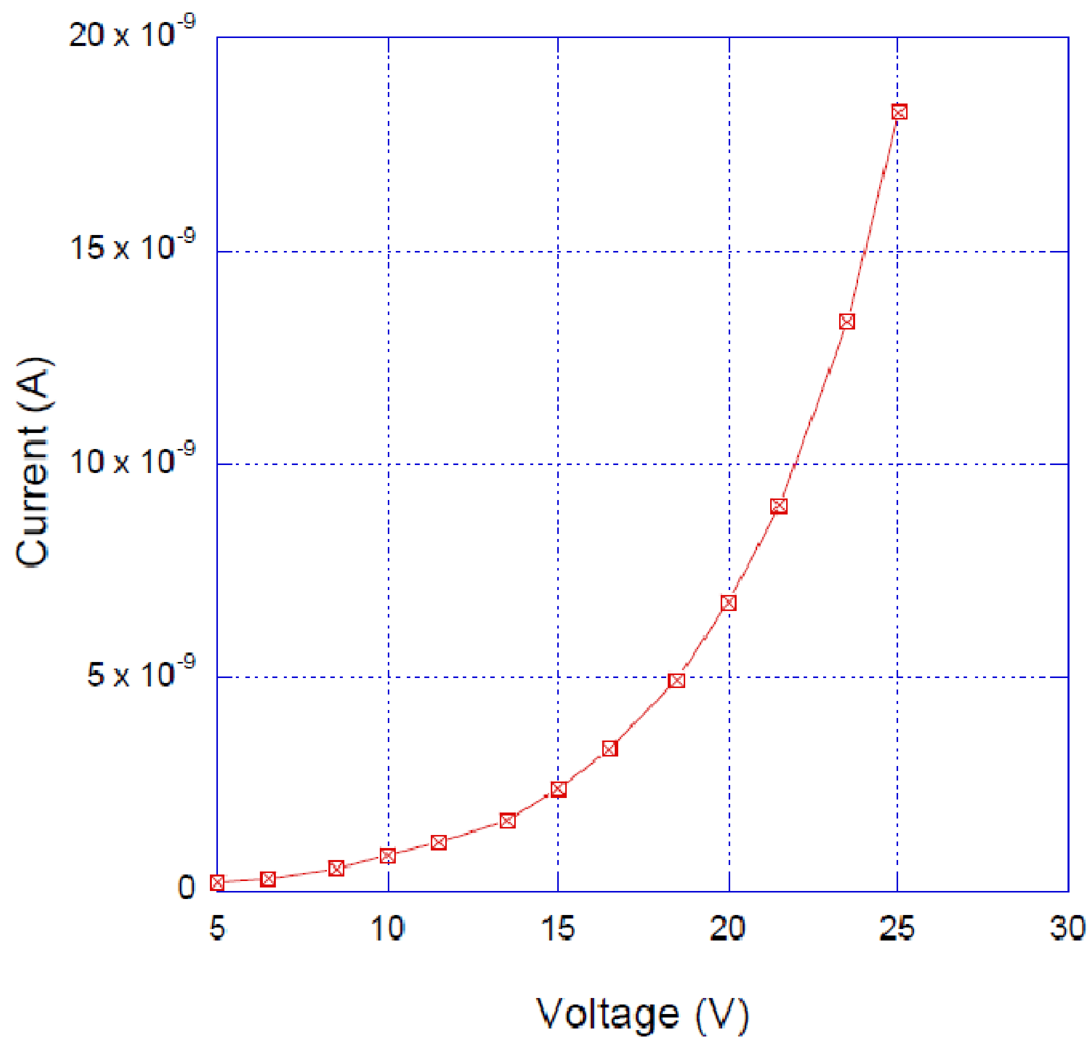

Fig. 5.7. Compiled I-V data of an *in situ* capacitor from I-time measurements.

To demonstrate the importance of including the right time delay, it is helpful to observe the I-V characteristics resulting from I-time measurements without sufficient delay. This result in an I-V characteristic with a higher current than the actual value because the current was measured before it could decay to a steady state value.

Performing I-V measurements directly, without using the I-time technique described earlier will also result in a higher value of current than the actual value at the applied voltage. Fig. 5.8 shows the results from a direct I-V measurement performed using a step size of 500 mV and a step delay of 60 seconds along with I-V data compiled by performing I-time measurements using only a 600 second delay between applying the voltage and measuring the final current. This step size of 500 mV and step delay of 60 s was chosen to obtain the direct I-V data close to the data compiled from I-time measurements. If either of these parameters are varied, the results obtained will also vary significantly. This variation is because the time required for the current to reach steady state depends on the magnitude of the change in voltage applied across the capacitor. The measurements described above were performed using the HP 4156B on the same capacitor type that was used before without adding the 1 MΩ noise-limiting resistor in series to the capacitor. The current level in this figure is in the range of hundreds of nanoamperes while the current level in Fig. 5.7 is only in tens of nanoamperes. Thus, the utmost care should be taken when deciding the time delay used to obtain the I-V data; however, this problem might not be prominent in regular MOS structures used in the microelectronics industry because of their smaller area, smaller thickness and the presence of alternative slightly conductive paths between the electrodes.

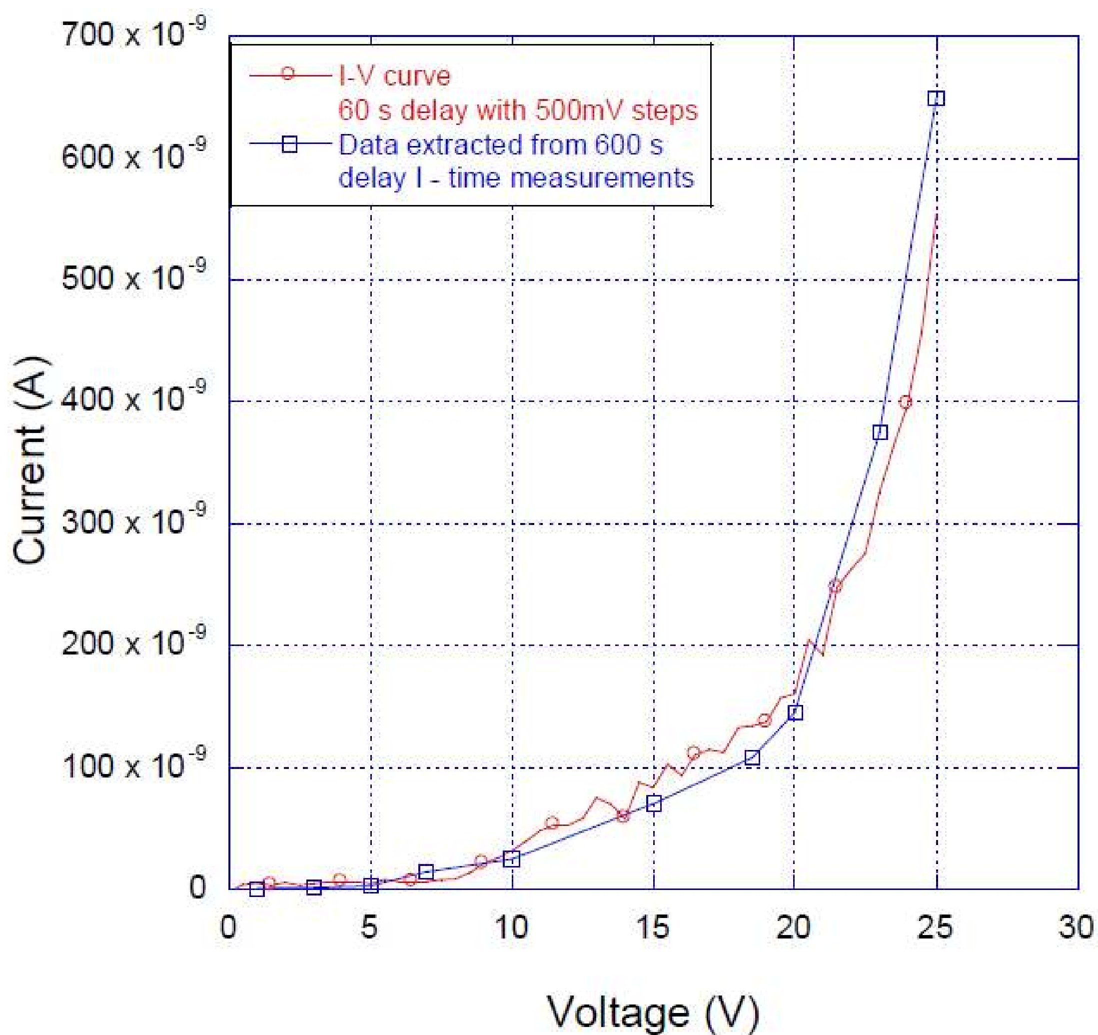

Fig. 5.8. Results from incorrect I-V measurements on an *in situ* capacitor.

During one phase of the research, soft probes were needed to make contact to a fragile layer of PEDOT that was deposited on to certain flat samples. This was achieved by using a graphite lead taken from a good quality dark pencil. A contact to this graphite lead was achieved by taping a soft copper foil around it, the foil itself being connected to the measurement system using alligator clips, as shown in Fig. 5.9. This probe only had a

resistance of 40 Ω, which is sufficiently low to make an I-V measurement; however, the PEDOT did not adhere well on the tantalum pentoxide surface and the measurements did not result in useful data for this research. Although the probe could not be put to significant use during this research, it will be useful for future research that may involve probing organic materials.

Fig. 5.9. Graphite probe attached to an alligator clip.

5.2 C-V Measurements

Another method to characterize capacitors is a C-V measurement. To perform this, an Agilent E4980A Precision LCR meter was used with the sample held inside the cage of the cryostat, manufactured by SULA Technologies, Inc. (Ashland, OR). However, these C-V measurements resulted in data that was less insightful than the data obtained from I-V measurements; hence, this thesis does not present an analysis of the

C-V data. In a research conducted earlier, C-V results were used to show that polymer Ta capacitors exhibit typical characteristics of MIS devices, suggesting that polymer Ta capacitors can be considered as MIS devices for analysis purposes [30].

The discrete capacitors measured in this research, being non-ideal, have parasitic resistances associated with them. The LCR meter used to make the capacitance measurements reports the DUT's characteristics as either a capacitor in series with a resistor or a capacitor in parallel with a resistor, depending on the mode chosen. This meter technically measures only the complex impedance of the DUT; with this information, the meter calculates the capacitance and the resistance of the DUT, depending on the series or the parallel mode chosen. To achieve optimal results, the LCR meter manufacturer suggests that the parallel mode be used while measuring a capacitor with an impedance greater than 10 kΩ and the series mode while measuring a capacitor with an impedance less than 10 Ω [67]. At standard testing frequencies of both 120 Hz and 1 kHz, the 10 μF capacitor's impedance is 132 Ω and 16 Ω respectively, both of which do not fall directly in any of the two specified ranges. For this situation, the instrument manufacturer does not suggest any particular mode for measurement; experiments were performed to determine the correct mode. In these experiments, several capacitors were measured using both modes and the results are tabulated in Table II. Cs and Rs are the measured values in the series mode, while Cp and Rp are the measured values in the parallel mode. R-X is the measured resistance and reactance, which does not depend on the mode of measurement. $|X|_{SS}$ is the calculated value of reactance from Cs

and Rs, and $|X|_{PP}$ the calculated value of reactance using Cp and Rp. The values of $|X|_{PP}$ and $|X|_{SS}$ were calculated using the following equations,

$$|X|_{SS} = \sqrt{Cs^2 + Rs^2} \tag{5.6}$$

$$|X|_{PP} = \sqrt{Cp^2 + Rp^2} \tag{5.7}$$

Table II. Results from Series and Parallel mode measurements.

Series Mode		Parallel Mode		R-X Measured (Ω)	$\|X\|_{SS}$ (Ω)	$\|X\|_{PP}$ (Ω)
Cs (μF)	Rs (Ω)	Cp (μF)	Rp (Ω)			
36.8	1.6	36.7	807	1.6, -36.31	36.03	36.15
450	3.8	167	6.1	3.98, -2.84	2.94	7.94
502	0.5	474	12	0.670, -2.6	2.64	2.79
126	0.47	126.5	235	0.462, -10	10.53	10.48
127	1.8	122.9	62.5	1.78, -10.4	10.44	10.79
404	2.2	277.2	7.0	2.2, -3.28	3.28	4.78
414	1.95	296.7	7.18	1.93, -3.20	3.20	4.47
459	0.97	412	9.6	0.970, -2.9	2.89	3.22
11.7	0.24	11.67	656	0.284, -13.6	13.64	13.64
11.8	0.27	11.78	682	0.267, -13.5	13.51	13.51
11.9	0.13	11.96	1.4k	0.128, -13.2	13.31	13.31
11.9	0.13	11.98	1.3k	0.130, -13.2	13.38	13.29

From Table II, it can be observed that the calculated value of $|X|_{SS}$ is closer to the measured reactance, X, in all cases. Hence, for this research, the correct mode to measure the capacitance and resistance is the series mode. This result was also confirmed by the

capacitor manufacturer. The value of Rs physically represents the ESR of the capacitor plus uncompensated resistances of the cable leading to the DUT and the contact resistance between the probe and the capacitor's electrodes.

Another problem that occurs while measuring the characteristics of a capacitor with a large ac impedance and with a dc bias voltage applied across it is that if the capacitor's dc leakage is significant, it interferes with the impedance measurement by flooding the current sensors of the LCR meter. Under this condition, the meter displays "Overload" to warn the experimenter of the problem, this can be corrected by enabling the DC Isolation Feature on the LCR meter. With this feature turned on, the maximum dc leakage current that the Agilent 4980A can accept is 100 mA, which is large enough to account for dc leakages in typical capacitors.

5.3 Performing Measurement as a Function of Temperature

Performing either current or capacitance measurements at low and high temperatures require placing the DUT in the cryostat, which is connected to a liquid nitrogen Dewar. To cool the sample, a rotary pump is first used for roughing the cryostat, creating a vacuum, and then an electromagnetic pump is used to circulate liquid nitrogen around the cryostat's sample holder. The cryostat also has a built-in heating element to heat the DUT. The temperature range is controlled between 77 and 400 ˚K by a Lakeshore 331 Temperature Controller.

While performing measurements on discrete capacitors as a function of temperature, ample time should be allowed for the capacitor to cool down or warm up,

because it is often hermetically sealed. In addition, the temperature should be varied slowly to prevent thermal stresses from damaging the dielectric.

Thus, in this research I-time measurements were performed to obtain the I-V characteristics of the polymer tantalum capacitors by using a 1 MΩ noise-limiting resistor in series with the capacitors. Moreover, while measuring the capacitance, the series mode on the LCR meter was used and the DC isolation feature was turned ON whenever required.

CHAPTER SIX

CHARACTERISTICS OF POLYMER TANTALUM CAPACITORS

The *in situ* and pre-poly capacitors to be characterized were fabricated using the method described in Chapter 3, the oxide being grown with a formation voltage of 93 V, resulting in an oxide of thickness 186 nm and a capacitance of 35 μF. The capacitors fabricated at this formation voltage had a maximum rated/working voltage of 25 V at room temperature, and the area calculated using the ideal capacitor equation is approximately 350 cm^2. These capacitors were enclosed in a chip-type package with electrodes protruding from both sides. Prior to the actual measurement, all capacitors were aged and tested for breakdown by applying a dc voltage of 1.3 times their rated voltage for at least two hours.

Additionally, to study the dielectric without the effects of anode geometry and of the polymer, flat MIM capacitors were fabricated using a Ta foil on which the oxide was grown by applying a formation voltage of 110 V, resulting in an oxide of thickness 200 nm. The counter electrode was then deposited by evaporating small aluminum dots on the oxide using a shadow mask in a physical vapor deposition chamber. This process resulted in a flat structure of $Ta–Ta_2O_5–Al$ having an area of approximately 2 mm^2.

The primary goal of this research was to identify the major leakage mechanism that causes a higher leakage current in *in situ* capacitors than in pre-poly capacitors of identical dielectric thickness, grown using a similar process. The I-V characteristics of *in situ* capacitors will be examined first, followed by that of the pre-poly capacitors.

6.1 *In situ* Capacitors

The current in five *in situ* capacitors was measured between a range of 0–25 V, the compiled results being shown in Fig. 6.1. This data was compiled from the result of individual I-time measurements as described in the Chapter 5. The highest current measured in these samples at 25 V was 280 nA, while the lowest current at 25 V was 20 nA. Although the measured current is not identical in the five capacitors, the general trend is similar. These variations could possibly be due to minor variations in the process involved in the capacitor manufacturing and/or degradation due to previous measurements performed on them, both of which can change the dielectric's defect density and distribution.

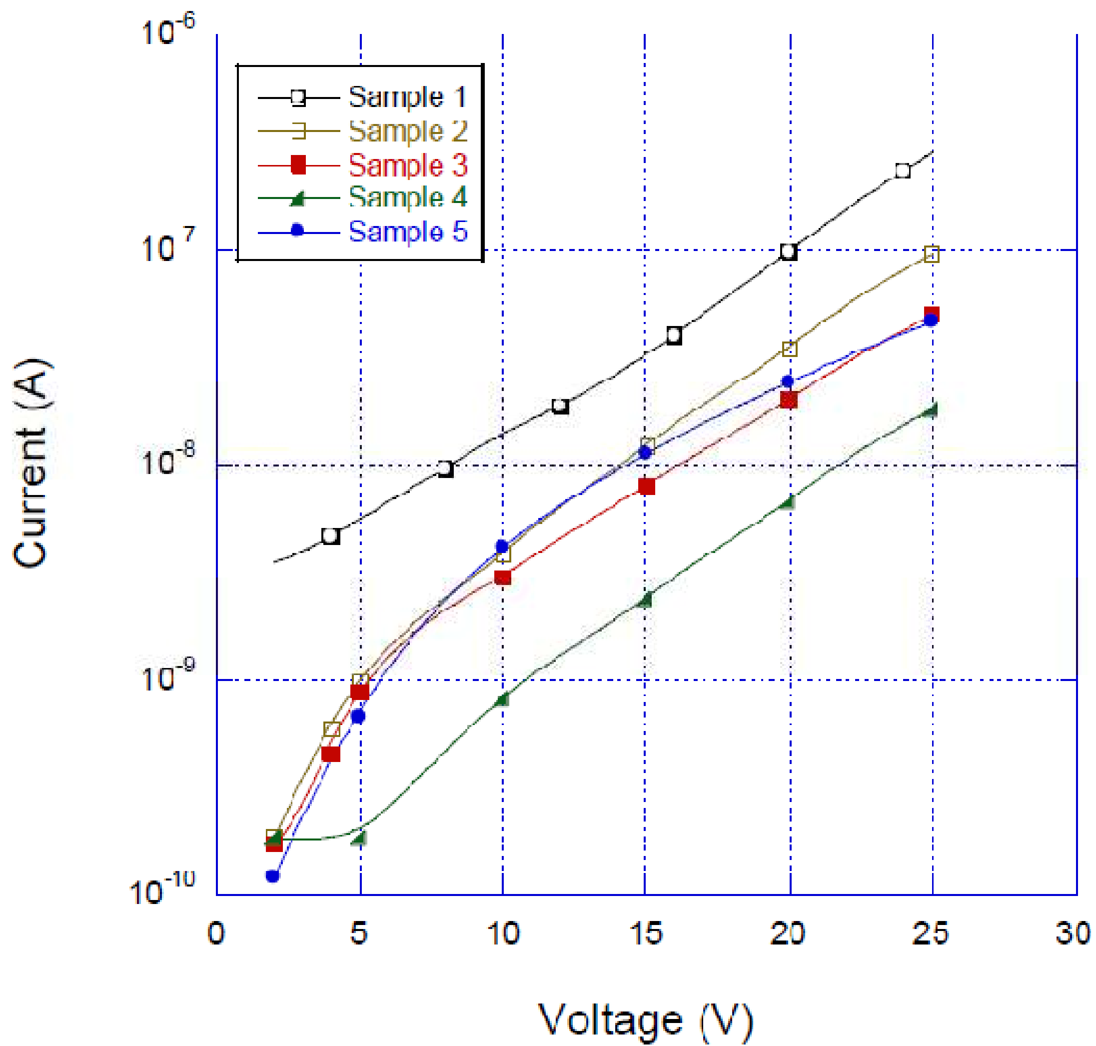

Fig. 6.1. I-V characteristics of *in situ* capacitors.

To investigate the dominant leakage mechanism, the I-V data for Sample 1 and 4, the two curves with the highest and lowest leakage current, were first presented on the characteristic plot of the Schottky Effect, a common leakage mechanisms observed in Ta_2O_5 structures. The equation pertaining to this characteristic plot was derived in Chapter 4.

To create the Schottky plot, the current density was calculated and its natural logarithm computed, the result being plotted against the square root of the electric field. The resulting plot is shown in Fig. 6.2, which shows good linear fits for Sample 1 in the 8–25 V range, and Sample 4 in the 5–25 V range. The correlation coefficient of these linear fits is greater than 0.99 and is consistent with the Schottky Effect. The equation for the linear fit obtained from Sample 1 is $\mathrm{y} = -29.2 + 0.0069\mathrm{x}$, implying a slope of 0.0069. In the case of Sample 4, the equation is $y = -32.2 + 0.0072\mathrm{x}$, implying a slope of 0.0072. The theoretical slope, $\frac{\beta}{2kT}$, of both Samples 1 and 4 is calculated to be 0.0029. Such a large difference between the calculated and measured slope suggests that the Schottky Effect is not the dominant leakage mechanism even though the data appears to fit the characteristic plot over a significant voltage range. Such situations, where the I-V data shows a good fit on the characteristic plot are common; however, the parameters determined from the fit should be compared with their theoretical values to identify the dominant presence of any leakage mechanism.

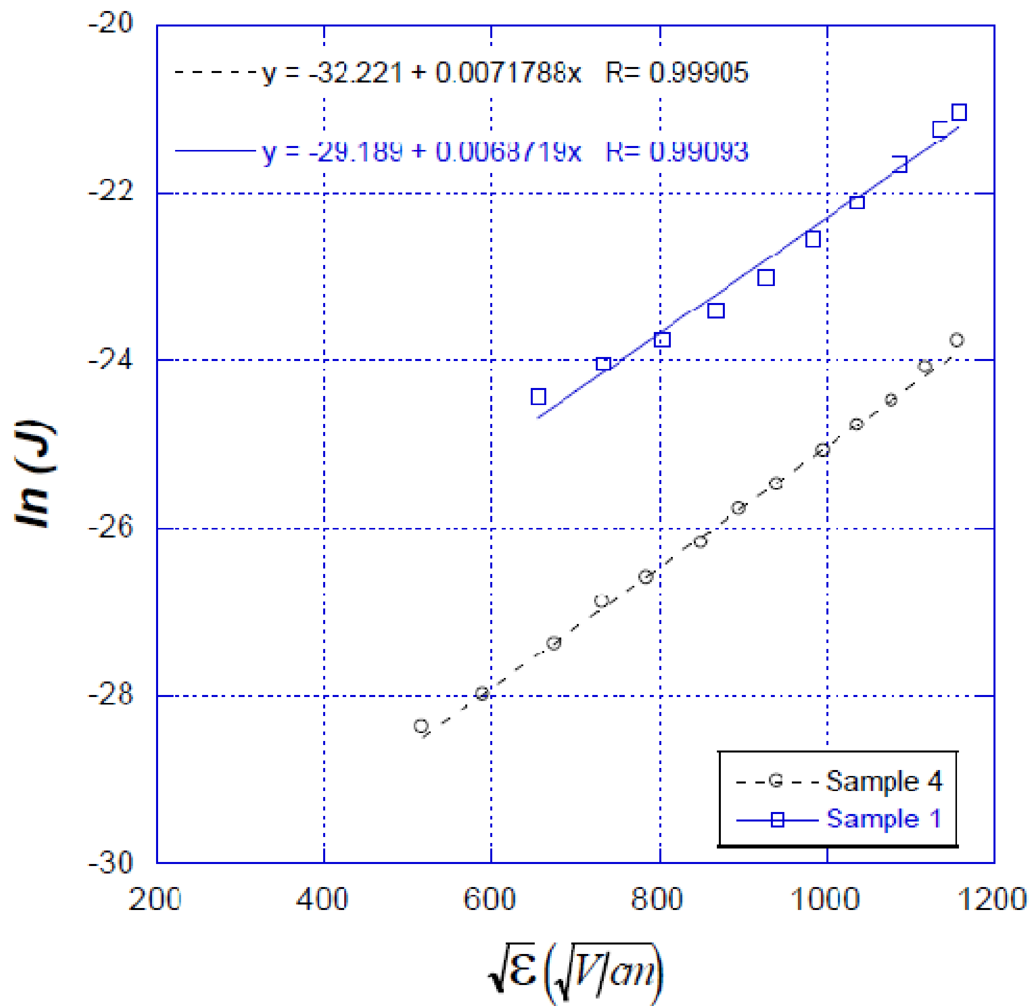

Fig. 6.2. Schottky plot of the I-V characteristics of *in situ* capacitors.

Since the Schottky Effect is inconsistent with the measurements, the data was plotted on a Poole-Frenkel characteristic plot, a common mechanism often observed in high k dielectrics [70]. The I-V data from Samples 1 and 4 are presented on a Poole-Frenkel characteristic plot and shown in Fig. 6.3. Linear fits with correlation coefficients greater than 0.99 were obtained in the range 12-25 V for Sample 1, and7-25 V for Sample 4, consistent with Poole-Frenkel emission. For Sample 1, the equation is $y = -37.8 +$

$0.005x$, implying a slope of 0.005, and for Sample 4, the equation for the fit is determined to be $y = -41.9 + 0.0057x$, implying a slope of 0.0057. These measured slopes are in good agreement with the theoretical calculated slope, $\frac{\beta}{\xi kT}$, which ranges between 0.0029 and 0.0058 when ξ varies from 2 to 1. To fit the measured current to the Poole-Frenkel current equation, the value of the Poole-Frenkel slope parameter, ξ, should be equal to 1.16 for Sample 1 and 1.01 for Sample 4. Both these values of ξ indicate heavy acceptor compensation in the dielectric.

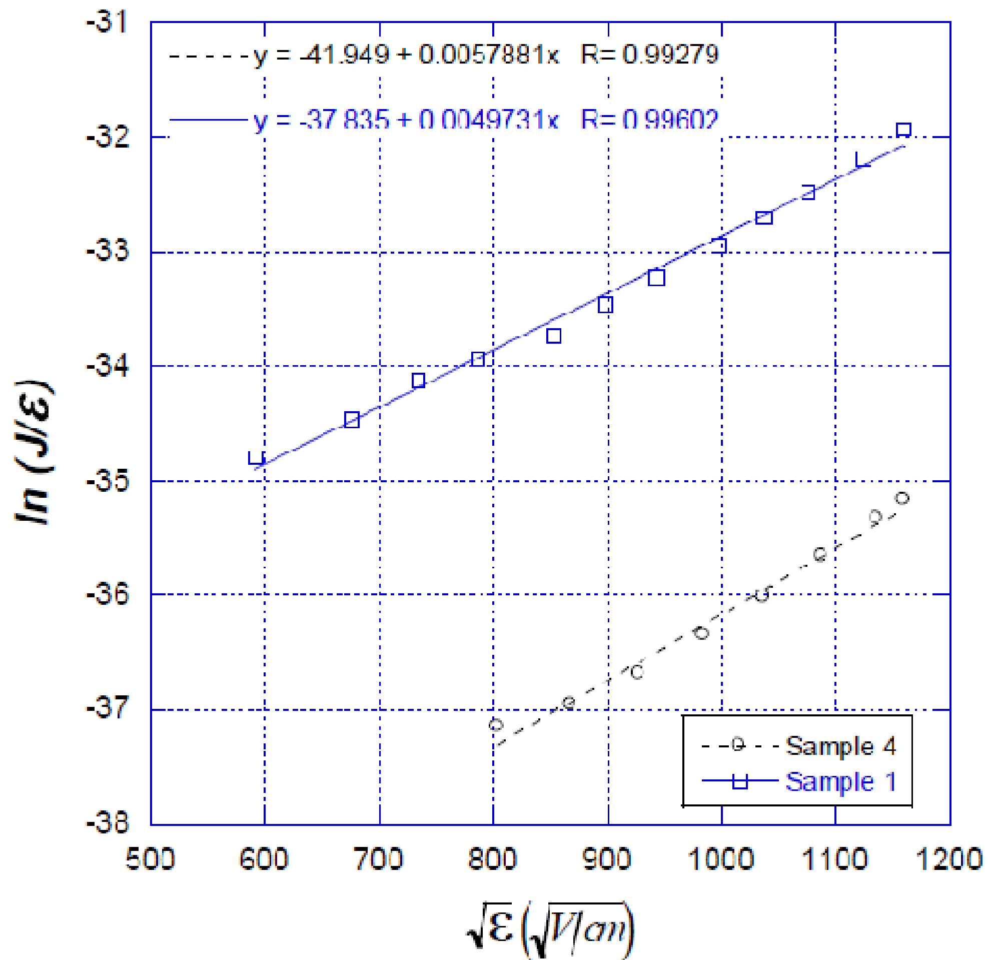

Fig. 6.3. PF plot of the I-V characteristics of *in situ* capacitors.

To further verify the presence of the Poole-Frenkel effect, the current was monitored at a constant voltage as a function of temperature. The capacitor was placed in the cryostat while its temperature was varied thrice between 250 ˚K and 325 ˚K. This capacitor was biased at 22 V, a reasonable voltage that is within its working range and the resulting current measured. When the temperature is varied, the current is expected to change as predicted by the Poole-Frenkel current equation, which can be rearranged and expressed as,

$$\ln(J) = \ln(C\mathcal{E}) - \frac{1}{T}\left(\frac{q\Phi - \beta\sqrt{\mathcal{E}}}{\xi k}\right) \tag{6.1}$$

The resulting Arrhenius plot of $\ln(J)$ versus $1/T$ is shown in Fig. 6.4. The linear region for both Sample 1 and 4 on the plot suggests that their leakage mechanism is a thermally activated process. For Sample 1, the equation for the linear fit is $y = -9.892 - 1740.5x$, yielding a slope of -1740.5. The theoretical slope of the Poole-Frenkel equation as a function of temperature in Eq. 6.1 is $-\frac{q\Phi - \beta\sqrt{\varepsilon}}{\xi k}$. Substituting the values of the known quantities and constants, the value of Φ, which is effectively the activation energy of this thermal process, was found to be 0.151 eV. Similarly, for Sample 4, the equation of the linear fit is $y = -18.568 - 1487.2x$, yielding a slope of –1487.2. The extracted activation energy was determined to be 0.148 eV, which is close to the extracted activation energy of Sample 1, 0.151 eV. Since the Poole-Frenkel Effect is thermally activated, these activation energy values represent the ionization potential, Φ, of the traps

that contribute to this effect. This evidence suggests that the Poole-Frenkel Effect is indeed the dominant leakage mechanism in the *in situ* capacitor.

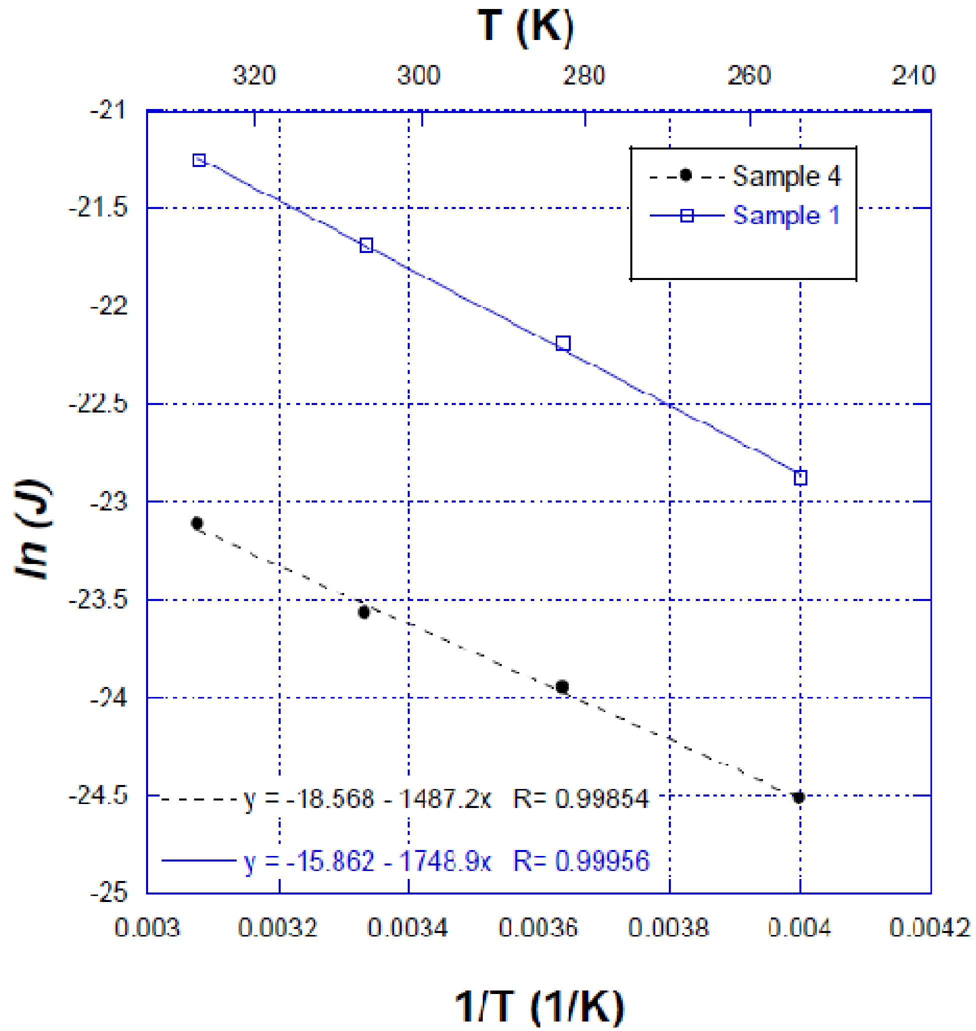

Fig. 6.4. Arrhenius plot for the *in situ* capacitors.

6.2 Pre-poly Capacitors

Similar experiments were performed on the pre-poly capacitors to investigate their leakage mechanisms. I-time measurements were performed on four samples and their compiled I-V curves are shown in Fig. 6.5. The results show that the maximum

current at 25 V in two samples is approximately 300 pA, while the current in the other two samples is approximately 700 pA. All samples show similar behavior up to approximately 15 V, after which the current in Sample 4 increases significantly. Samples 1, 2, and 3 remain similar even after 15 V until the current in Sample 2 increases significantly near 25 V. Similar to the results observed for the *in situ* capacitors, the current measured in similar samples of pre-poly capacitors varied, possibly due to minor variations in the manufacturing process. Two trends can be seen in the measured data, if the last data point in Sample 2 is not included: one trend that is representative of Samples 1, 2, and 3 and the other representative of Sample 4. To investigate the leakage mechanism behind these trends, both will be examined by analyzing the I-V data of Samples 3 and 4, those exhibiting the lowest and highest average current.

To investigate the pre-poly leakage mechanism, the I-V data of Samples 3 and 4 were analyzed on the characteristic Schottky plot, as shown in Fig. 6.6. A good linear fit was obtained in both cases from ~16–26 V, consistent with the Schottky Effect. The correlation coefficients were both greater than 0.99. The equations of these linear fits are $y = -33.25 + 0.0052x$ for Sample 4, implying a slope of 0.0052, and $y = -31.406 + 0.0029x$ for Sample 3, implying a slope of 0.0029. The theoretical slope is 0.0029, which is identical to the measured value in Sample 3, suggesting the presence of Schottky Effect in Sample 3. However, in Sample 4, the measured and calculated values of the slope disagree, suggesting the absence of Schottky Effect in it.

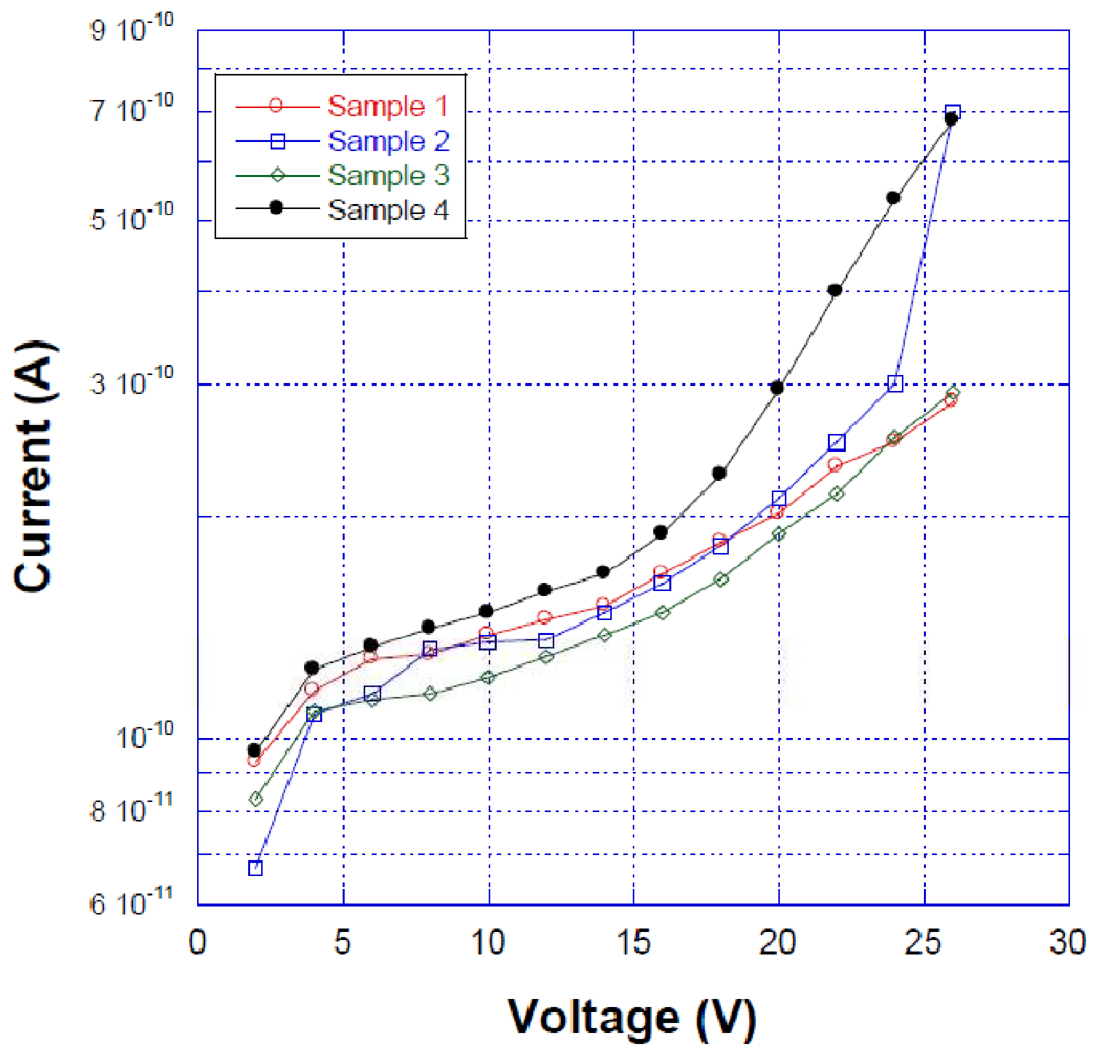

Fig. 6.5. I-V characteristics of pre-poly capacitors.

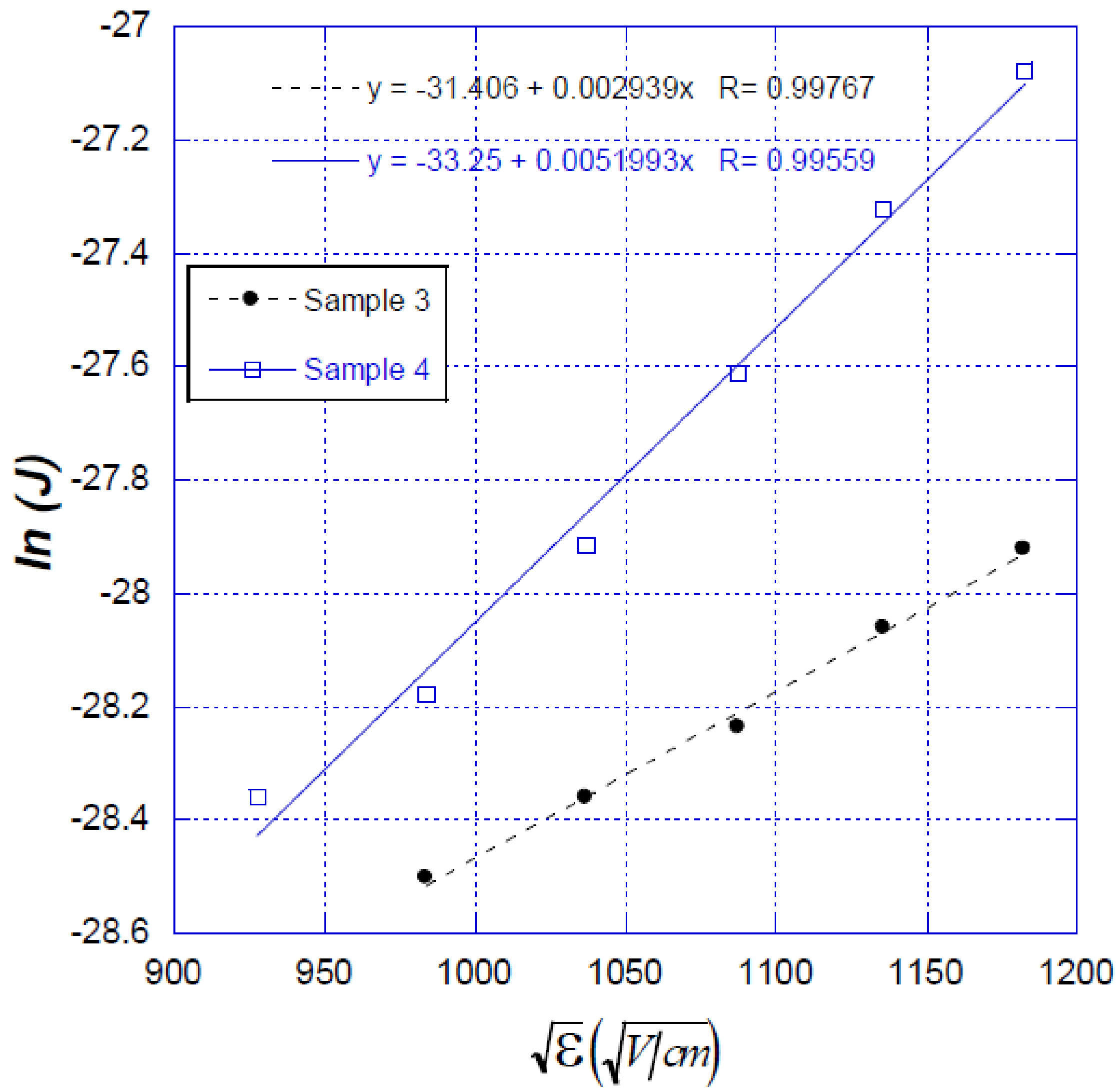

Fig. 6.6. Schottky plot of I-V characteristics of pre-poly capacitors.

To further investigate the validity of the Schottky mechanism in Sample 3, a current versus temperature measurement was performed. The current is expected to vary according to the Schottky Effect equation, which can be rearranged and expressed as,

$$\ln\left(\frac{J}{T^2}\right) = \ln(A^*) - \frac{1}{T}\left(\frac{q\Phi - \frac{1}{2}\beta\sqrt{\mathcal{E}}}{k}\right) \tag{6.2}$$

The resulting Arrhenius plot of ln (J/T^2) versus $1/T$ is shown in Fig. 6.7. The linear fit obtained suggests that the leakage mechanism is a thermally activated process. According to Eq. 6.2, the slope of this fit is $-\left(\frac{q\Phi-\frac{1}{2}\beta\sqrt{\mathcal{E}}}{k}\right)$. Equating this slope to the one measured from the Fig. 6.7, which is – 6290, and then substituting all the known values and constants into the theoretical slope, the value of Φ obtained is 0.54 eV. This activation energy of the thermal process represents the Schottky barrier height. Since these results are consistent with the Schottky Effect, and because Samples 1, 2, and 3 exhibit similar I-V characteristics, we conclude that the leakage is dominated by the Schottky Effect in these three devices.

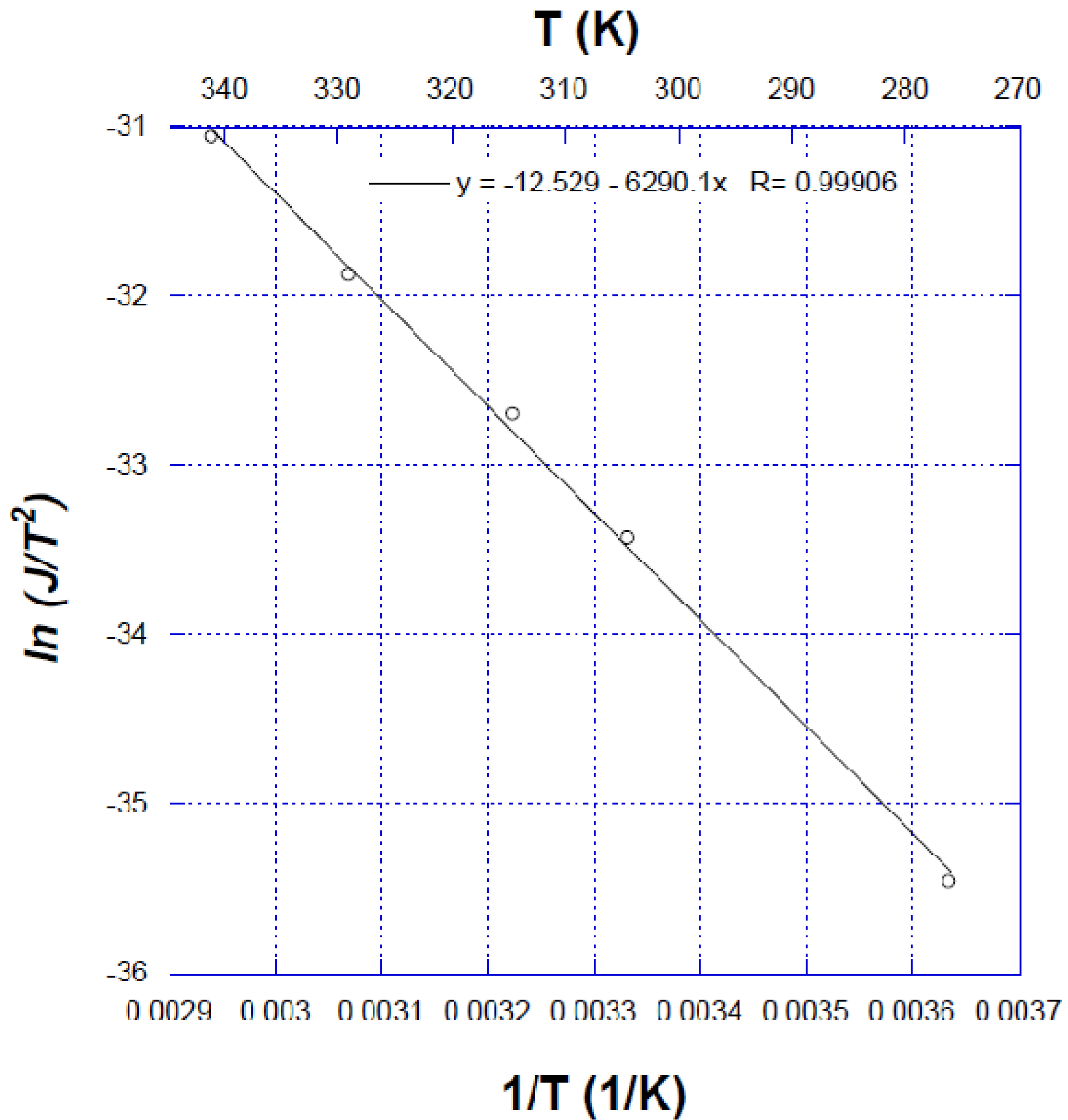

Fig. 6.7. Arrhenius plot for pre-poly capacitor (Sample 3).

Since the current in Sample 4 is not consistent with the Schottky Effect, its I-V measurements were plotted on the Poole-Frenkel characteristics plot and is shown in Fig. 6.8. The I-V data of Sample 3 is plotted alongside the data of Sample 4 to allow comparison.

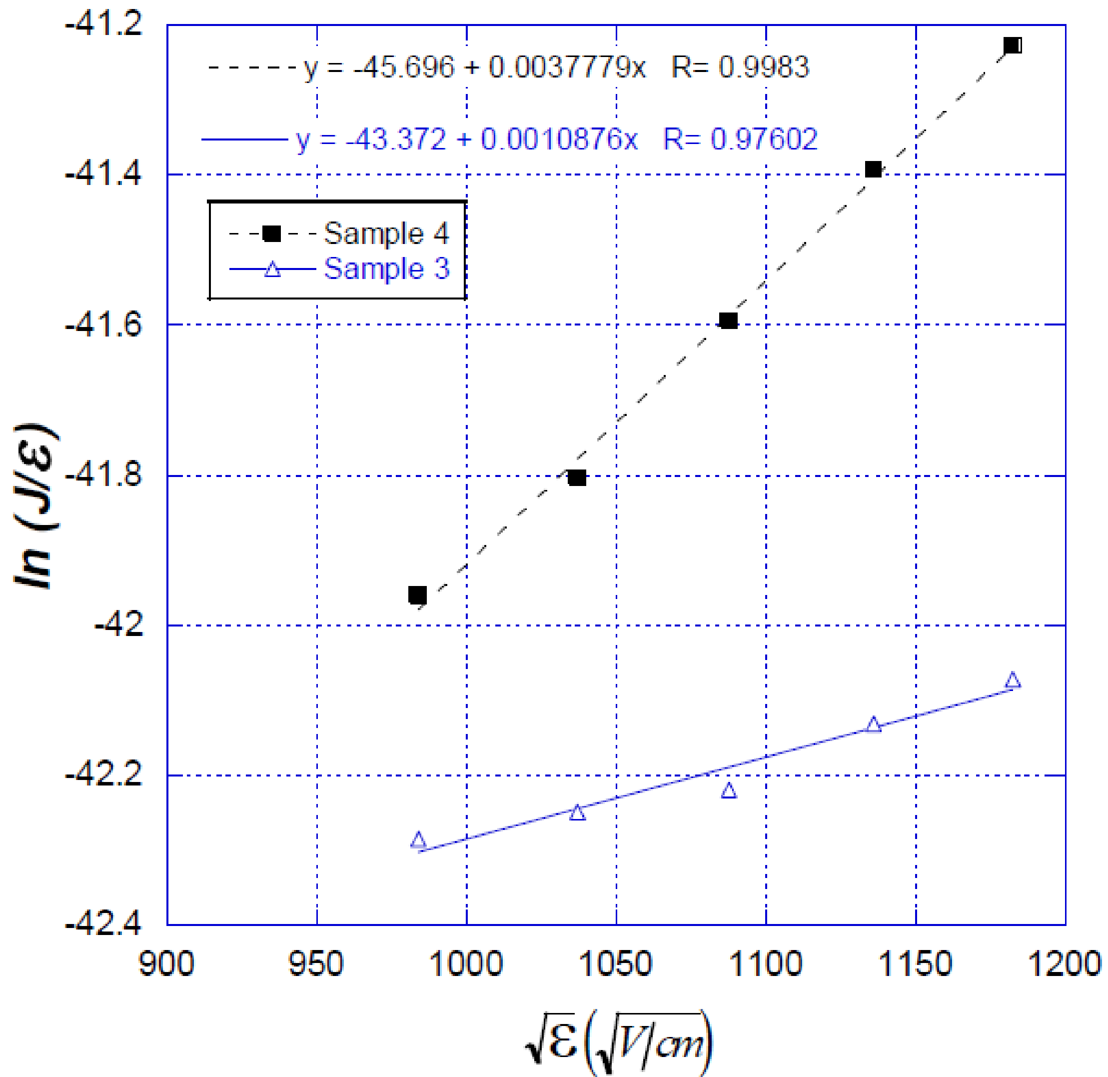

Fig. 6.8. PF plot of the I-V characteristics of pre-poly capacitors.

As this plot shows, the I-V data of Sample 4 exhibits a good linear fit from 18 to 26 V, with a correlation coefficient greater than 0.99; however, Sample 3 does not exhibit a good linear fit in the same voltage interval, as its correlation coefficient is only 0.97. The good linear fit in the case of Sample 4 is consistent with the Poole-Frenkel Effect,

although the fit with a correlation coefficient lower than 0.99 in the case of Sample 3 does not rule out the presence of Poole-Frenkel Effect. To investigate these observations, the equations for the two fits were calculated. For Sample 3, the extracted equation is $y = -43.372 + 0.0011x$, implying a slope of 0.0011, while for Sample 4, the extracted equation is $y = -45.696 + 0.0038x$, implying a slope of 0.0038. Comparing these extracted slopes to the theoretical PF slope range of 0.0029 to 0.0058 suggests that for a value of $\xi = 1.53$, the I-V data obtained for Sample 4 can be modeled by the PF current equation. However, the slope of the linear fit of the I-V data of Sample 3 is not close to the theoretical PF slope for any possible value of ξ, indicating that the Poole-Frenkel mechanism is not dominant in Sample 3. This further verifies the presence of the Schottky Effect in Sample 3.

To further verify the presence of the Poole-Frenkel Effect in Sample 4, its current versus temperature characteristics were measured. During this experiment, the current in this sample exhibited anomalous behavior, resulting in negative currents at a voltage bias of 22 V, a phenomenon more prominent at temperatures below 300 ˚K which results in a current in the range of a few picoamps. Fig. 6.9 shows the leakage current in Sample 4 at 22 V, hours after the temperature was lowered from 350 to 275 K. Even after eleven hours, the current failed to stabilize. The current can even be observed to flow in the opposite direction of the applied voltage at some point on the curve. Although this behavior was also observed in Sample 3, it was not as dominant as in Sample 4. Because of this problem, current versus temperature measurements could only be performed across a limited temperature range. Possible reasons for this behavior could be the

presence of deep traps in the dielectric that become filled at high temperatures, creating an internal electric field within the dielectric. This internal field then forces the electrons to flow in a direction opposite to the externally applied field, resulting in a negative current at an externally applied positive voltage. This negative current flow is also supported by the lower barrier to electron flow in the reverse direction than in the forward direction, a property that makes currently manufactured tantalum capacitors polar in nature [30].

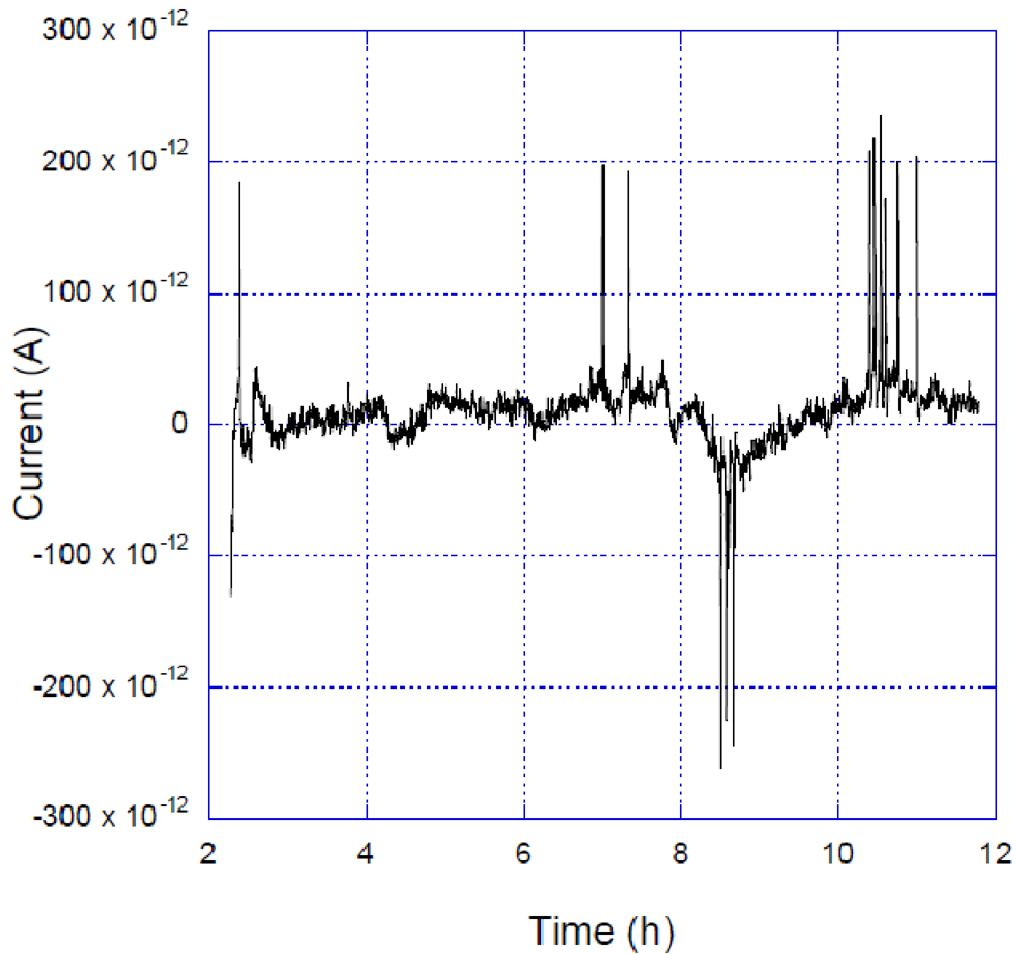

Fig. 6.9. Variation of current with time in Sample 4 at 250 K.

The current versus temperature data for Sample 4 was plotted on the Arrhenius plot shown in Fig. 6.10. A good linear fit was obtained, suggesting that the leakage mechanism is thermally activated. The equation of the fit is $y = -8.8948 - 5663.4x$, implying a slope of –5663.4. Comparing and analyzing this measured slope with the slope of Eq. 6.1 results in an activation energy of 0.75 eV for the process. This extracted activation energy represents the ionization potential of the traps in the dielectric, which gives rise to the Poole-Frenkel Effect.

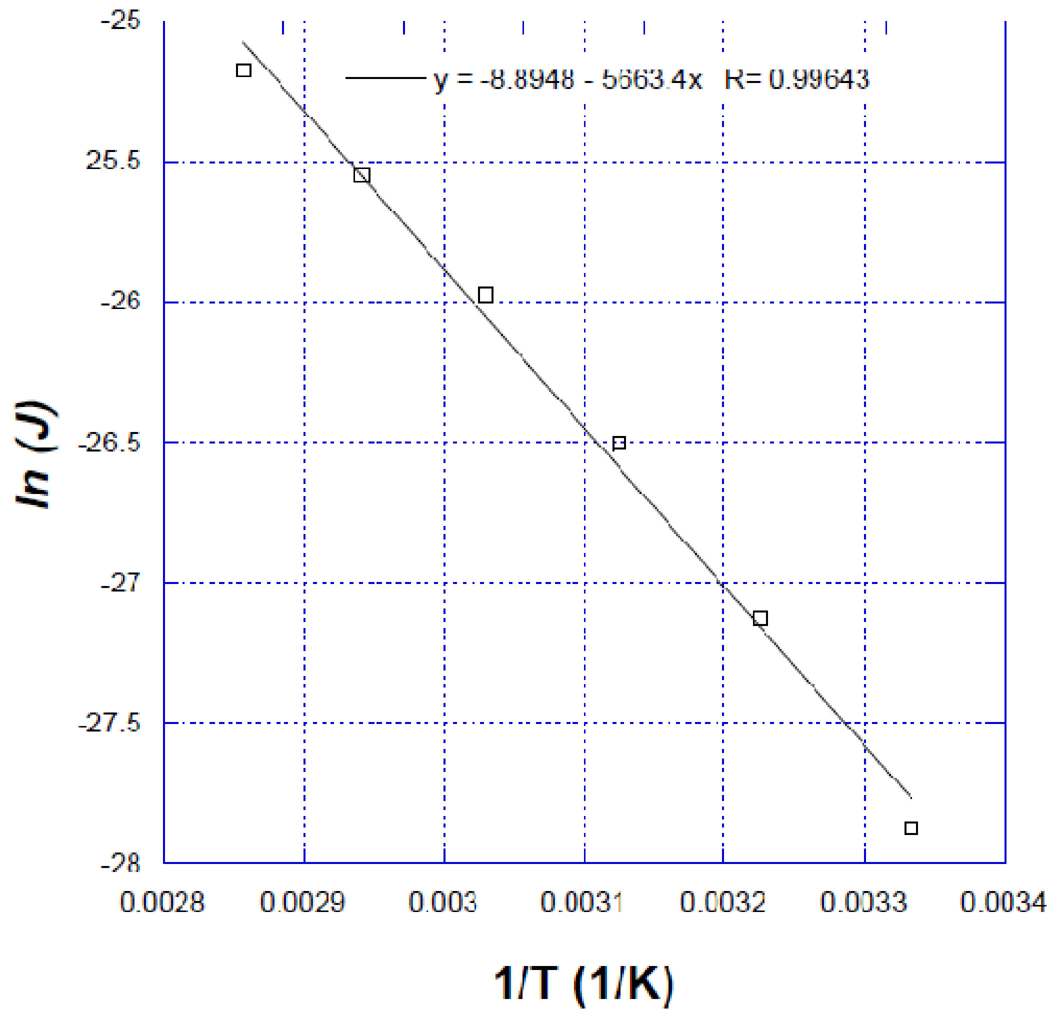

Fig. 6.10. Arrhenius plot for pre-poly capacitor (Sample 4).

Since, the I-V data for one pre-poly sample fits the Schottky Effect and I-V data for another pre-poly sample fits the Poole-Frenkel Effect, one single mechanism cannot explain the leakage in these pre-poly capacitors. However, the Schottky barrier height of Sample 3 and the ionization potential of the traps in Sample 4 are moderately high to prevent excessive leakage current flowing through the dielectric.

6.3 Comparison of *In situ* and Pre-poly Capacitors

To compare the I-V characteristics of *in situ* and pre-poly capacitors, all the data were plotted together on the graph as shown in Fig. 6.11. It is clear that the current at 25 V in the *in situ* capacitor is significantly higher than that in the pre-poly capacitors. Numerically, the current in the *in situ* capacitor at 25 V is in the range of 20-300 nA, while the current in the pre-poly capacitor is in the range of 0.25-0.7 nA. Although the figure shows the data for only a few capacitors, these measurements agree with the values reported by KEMET Electronics Corp. based on its measurements of numerous *in situ* and pre-poly capacitors. Thus, statistically, the *in situ* capacitors have significantly higher leakage currents than the pre-poly capacitors. This higher leakage current is the probable cause of the lower breakdown voltage of *in situ* capacitors as compared to the pre-poly capacitors. Because of this low breakdown voltage exhibited in *in situ* capacitors, KEMET has phased out manufacturing of high voltage polymer Ta capacitors using the *in situ* polymerization.

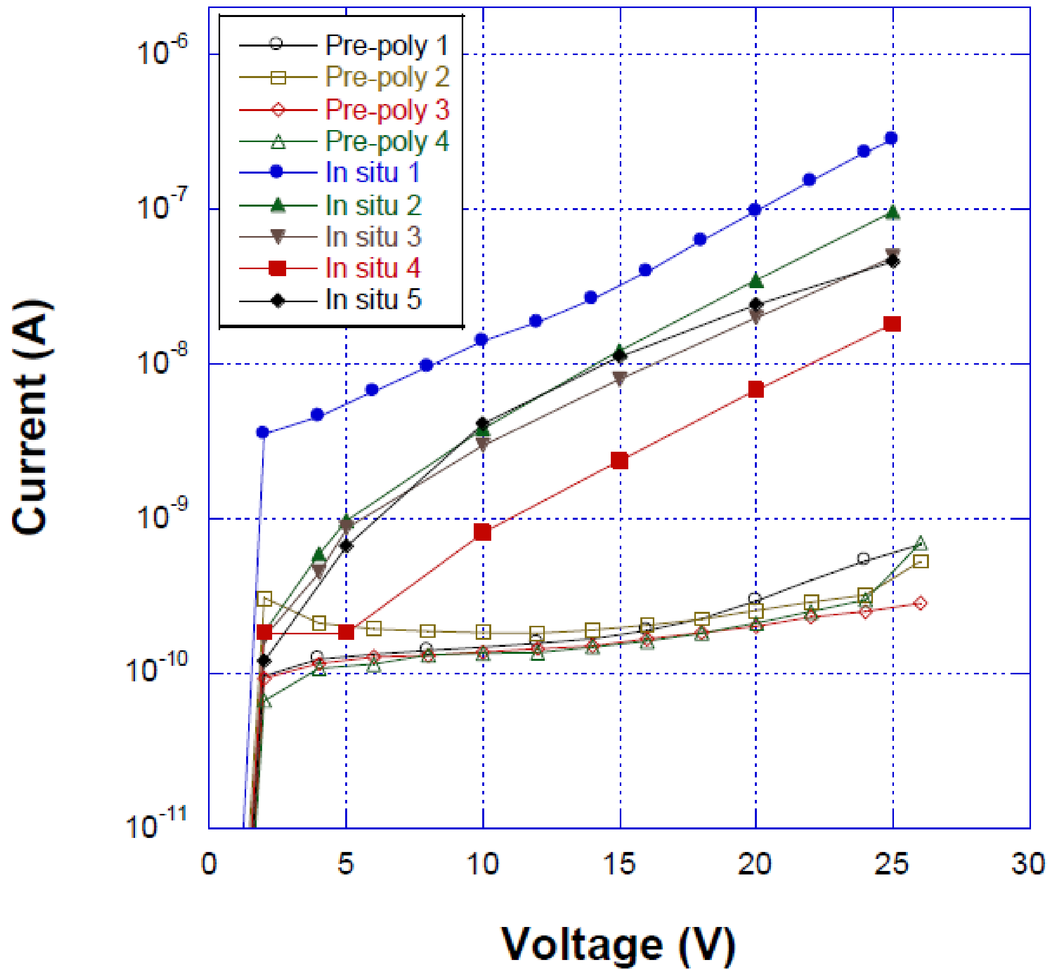

Fig. 6.11. Comparison of I-V characteristics of *in situ* and pre-poly capacitors.

The results obtained here also imply the presence of shallow traps in the dielectric of the *in situ* capacitor that contribute to current conduction through the dielectric resulting in its lower breakdown voltage. This defect-initiated breakdown has been observed in other dielectrics such as the SiO_2 [39]. In addition, according to Allers, the reliability of a dielectric can be predicted from its I-V characteristics by a $\sqrt{E}$ model, because the current density of the Poole-Frenkel Effect varies as $\sqrt{E}$ [68]. This means

that a dielectric with a lower leakage current density has a higher reliability and thus a decreased probability of breakdown in comparison with one that has a higher leakage current density. Thus, pre-poly capacitors are more reliable than their *in situ* counterparts are.

6.4 Reverse Polarity Characteristics of Tantalum Capacitors

Thus far, this research has investigated only the forward biased operation of the capacitors, because they tend to breakdown readily with the application of a small reverse voltage. To observe the reverse characteristics of discrete polymer Ta capacitors, further measurements were performed, and the current densities measured at positive and negative biases are shown in Fig. 6.12. The current density was plotted to facilitate comparison with data reported later. Since applying a reverse bias causes the capacitors to breakdown more readily, only one measurement for each type of capacitor was conducted. As Fig. 6.12 shows, the leakage current increases rapidly as the applied reverse voltage is increased in both the *in situ* and the pre-poly capacitors.

To explore the fundamental conduction mechanism in the dielectric that prevents it from operating in reverse bias, measurements were conducted on a flat MIM Ta-Ta_2O_5-Al structure. The results are shown in Fig. 6.13. Two major observations that can be made are: the current density at 15 V in the MIM structure is approximately 50 nA/cm^2, which is five orders of magnitude greater than the value for the discrete capacitors at the same voltage.

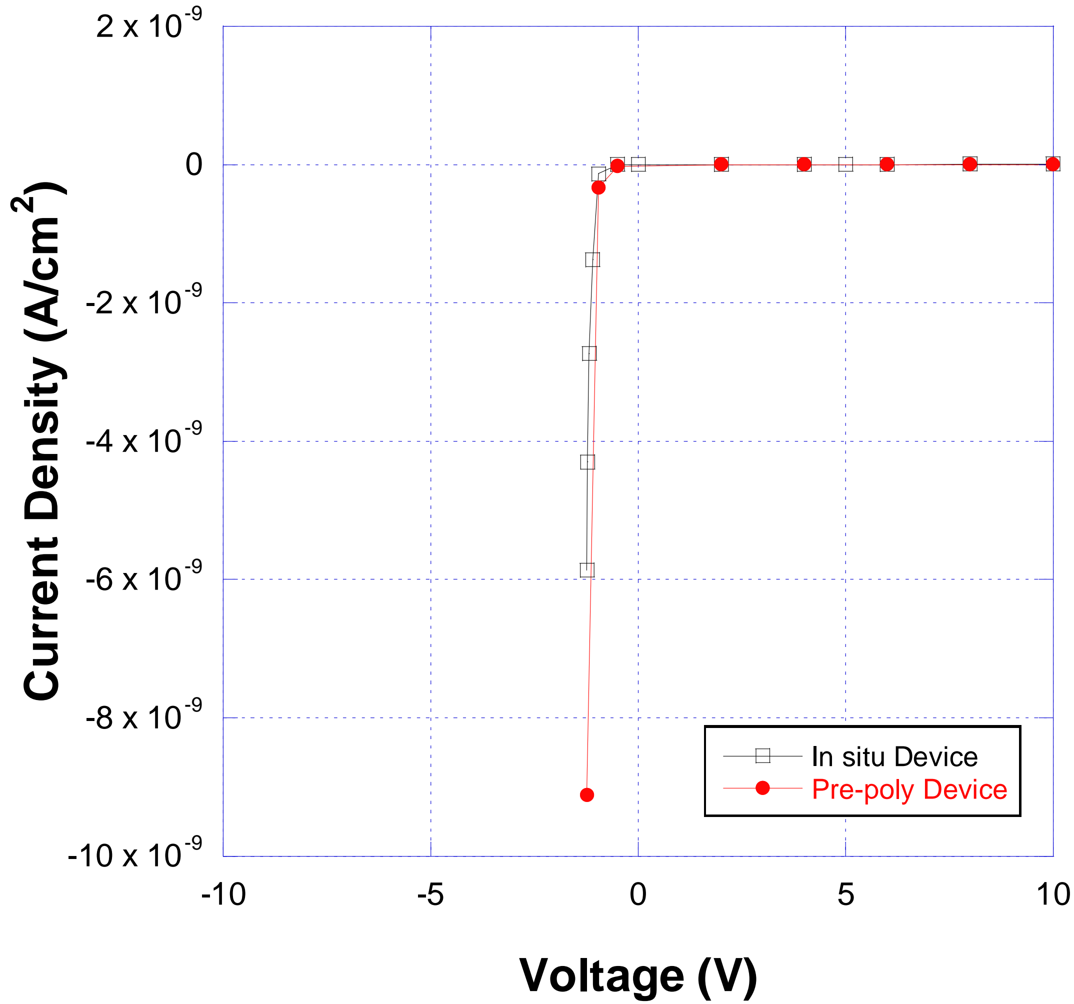

Fig. 6.12. I-V curve of discrete polymer capacitors from – 1 to 10 V.

The cause of this high current is probably because the MIM structures do not have self-healing capabilities, meaning the defects formed during fabrication are not healed during operation. In addition, the Ta foil used to fabricate these MIM structures contained surface impurities, giving them a lower purity than the Ta powder used to manufacture the polymer Ta capacitor. These surface impurities were created because of the process

used to fabricate the Ta foils [69]. Moreover, the oxide in the MIM structures was not annealed after growth, so this oxide had a higher defect density than the oxide in the discrete polymer Ta capacitors. In addition, unlike the discrete capacitors, the MIM structure was exposed to the atmosphere during testing, since they were not sealed in a package.

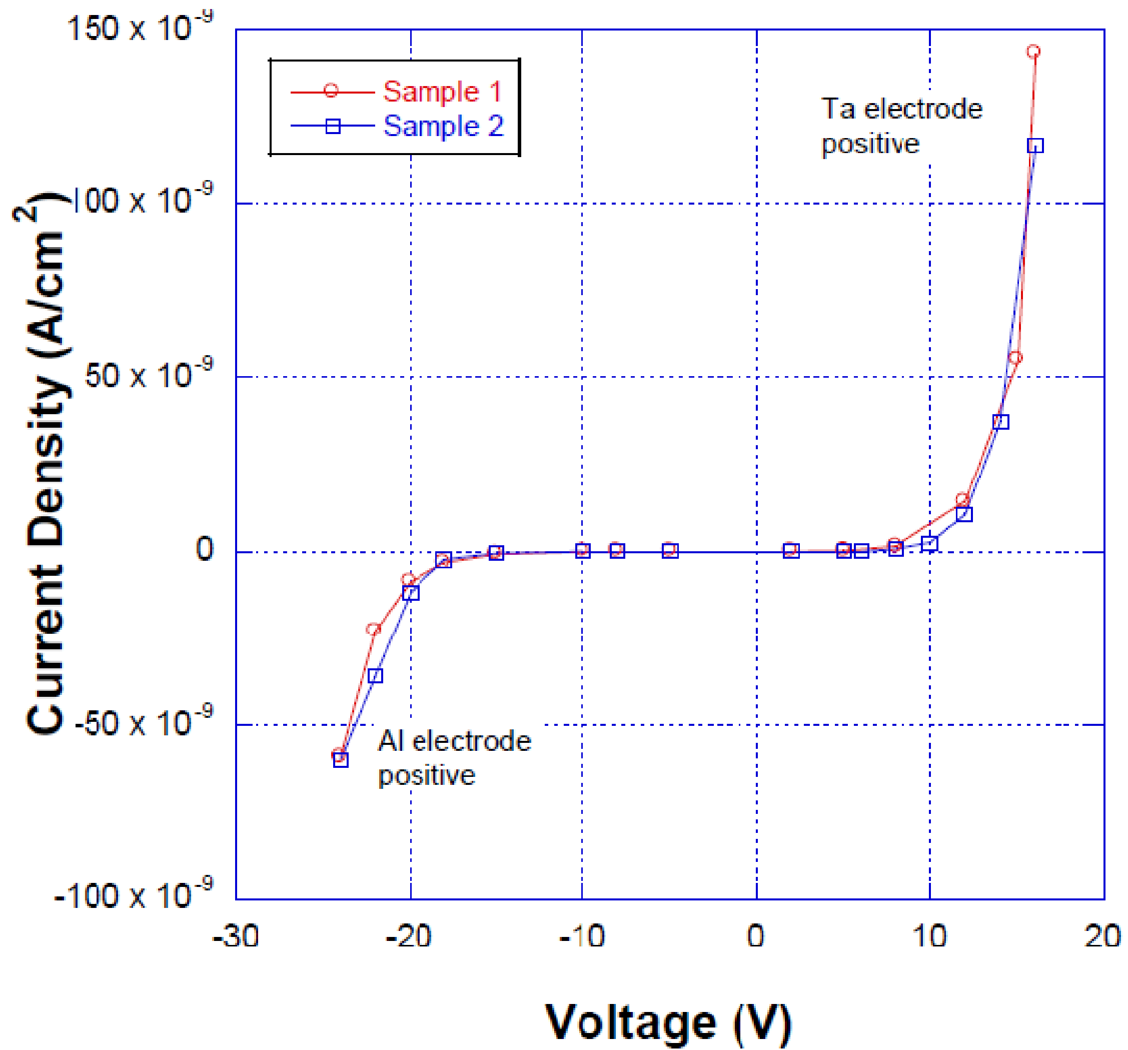

Fig. 6.13. I-V characteristics of the Ta-Ta_2O_5-Al MIM structure.

The second major observation is that the current densities at positive and negative voltages are reasonably symmetrical in the voltage range of ±10 V, unlike the discrete capacitors in which the I-V characteristics are severely asymmetrical. Numerically, the current density in the discrete capacitor at –1 V is in the region of 5 nA/cm^2, while that in the MIM structure is only 1 pA/cm^2, a difference of three orders of magnitude. This suggests that it is possible to make Ta based discrete capacitors with a lower reverse polarity leakage current than in the existing Ta capacitors. The general current versus voltage behavior of these MIM capacitors is qualitatively explained based on the electronic band diagram of the MIM structure illustrated in Fig. 6.14.

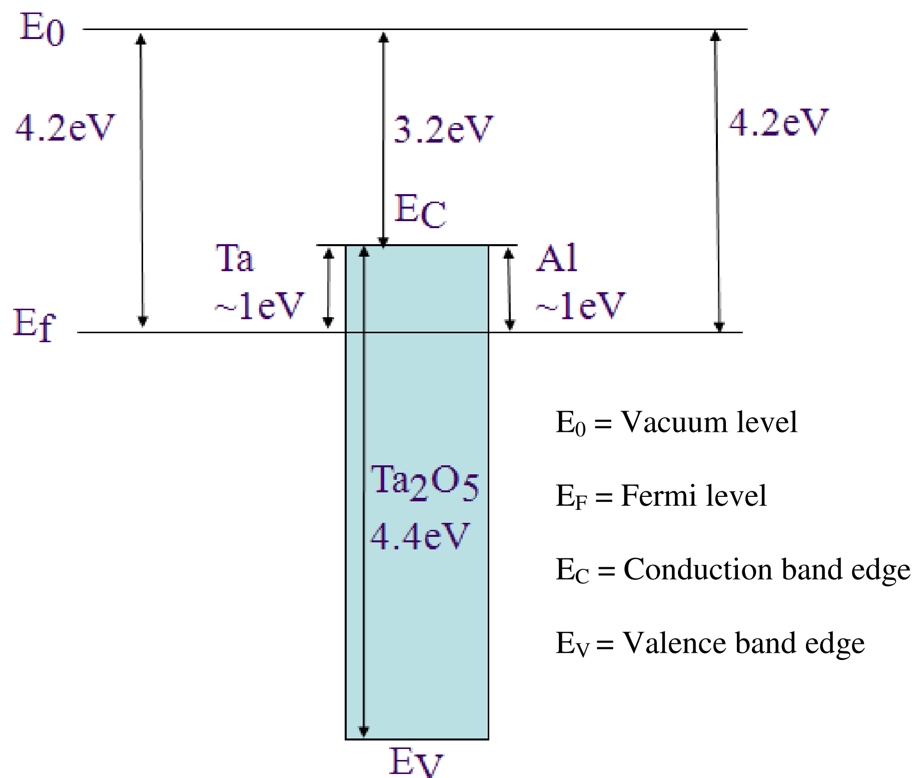

Fig. 6.14. Electronic band structure of Ta-Ta_2O_5-Al

As this figure shows, the work function of Ta and Al are both approximately equal to 4.2 eV, meaning that the barrier for electron flow through the structure in either direction is essentially the same. Since the current at both forward and reverse polarity is comparable, there is no fundamental reason why Ta_2O_5 cannot be used as a dielectric in at least low voltage non-polar capacitors. To fabricate high voltage non-polar capacitors, which operate equally well, both at high forward and at high reverse polarity, Ta is probably not a good choice. This is because the maximum barrier to electron flow between the Ta and the dielectric at reverse polarity is only 1 eV, which may not be high enough to prevent electrons hopping across the barrier and causing leakage. However, this low barrier will not prevent the capacitor from operating at a high forward polarity, during which the barrier between the cathode and the dielectric plays an important role.

The measurements on the polymer Ta capacitors reveal the presence of the Poole-Frenkel mechanism in all the *in situ* capacitors and one pre-poly capacitor; however, the Schottky mechanism was observed in the other pre-poly capacitors. In the capacitors that exhibited the Poole-Frenkel Effect, the trap depth was determined to be 0.15 eV for the *in situ* type and 0.75 eV for the pre-poly type. The other pre-poly capacitors, which exhibited the Schottky mechanism, were found to have a barrier of 0.54 eV. From these results, we conclude that the primary reason for the higher current in the *in situ* capacitors as compared to the pre-poly capacitors is the presence of shallow traps in the *in situ* devices. This higher leakage current in the *in situ* capacitors causes their breakdown to

occur at approximately 50 V. On the other hand, pre-poly capacitors exhibit a lower leakage current because of the presence of either a sufficiently high electron-blocking barrier and/or only deep level traps. In addition, measurements on flat MIM samples suggest that no fundamental problems exist in the Ta_2O_5 dielectric that prevents it from being used in low voltage non-polar capacitors.

CHAPTER SEVEN

SUMMARY AND CONCLUSIONS

In this thesis, a technique to accurately measure the leakage current in polymer Ta capacitors was established. Using this technique, the pre-breakdown current in *in situ* and pre-poly polymer tantalum capacitors was measured. From the measurements, it is evident that the *in situ* capacitors exhibit a significantly higher leakage current than the pre-poly capacitors, even though the only difference between the two is the method used to deposit the PEDOT. To determine the leakage mechanism in both capacitors, their measured I-V characteristics were modeled and analyzed. Results from the analysis indicate the presence of the Poole-Frenkel mechanism in the *in situ* capacitors and the presence of both Poole-Frenkel and Schottky mechanisms in the pre-poly capacitors.

Additional current versus temperature measurements were performed to verify the leakage mechanisms and to determine the activation energy of the mechanism. The results from these experiments were consistent with the leakage mechanisms deduced from the previously obtained results at room temperature. The activation energy was determined by creating Arrhenius plots of the leakage mechanism. For *in situ* capacitors, the activation energy obtained was 0.15 eV, while in the pre-poly capacitors, two activation energy values were obtained: 0.54 eV and 0.75 eV. Since the *in situ* capacitors exhibited the Poole-Frenkel mechanism, their activation energy represents the depth of the traps in the Ta_2O_5 dielectric. In the case of the pre-poly capacitors, their activation energy of 0.54 eV represents the Schottky barrier height, and the activation energy of 0.75 eV represents the trap depth in the sample which exhibited the Poole-Frenkel Effect.

Both the Schottky barrier and the deep level traps assist in limiting the leakage current through the dielectric.

In comparison with independent results, the extracted activation energy for the *in situ* capacitors is close to the 0.17 eV value that KEMET independently determined [10]. The calculated activation energy for the pre-poly capacitors, 0.54 eV and 0.75 eV, are close to the activation energy for wet type Ta capacitors, in which the activation energy is 0.6 eV. This result suggests that pre-poly capacitors can operate at high voltages similar to the wet Ta capacitors [10]. KEMET has already fabricated polymer Ta capacitors with a working voltage of 125 V. This development is a significant improvement over existing polymer capacitors with a working voltage of only 25 V. This research suggests that the Poole-Frenkel and Schottky Effects are the prominent dielectric leakage mechanisms in Ta_2O_5 based devices; this conclusion is also supported by previous research [45, 58, 59, 60, 61, 62].

In all cases, the measured I-V characteristics showed minor variations between samples of the same type. Although the limited number of capacitors available for characterization meant a statistical analysis of this data was not feasible, data from KEMET Electronics Corporation confirm that the *in situ* capacitors have a higher leakage and lower breakdown voltage than pre-poly capacitors.

Measurements were also conducted on Ta-Ta_2O_5-Al flat samples to investigate the behavior of the dielectric at reverse polarity. The I-V curve obtained for the flat samples was symmetrical in magnitude at positive and negative applied voltages, suggesting that the dielectric by itself does not have a fundamental limitation that makes

it unsuitable for negative polarity operation. However, the electronic barrier between Ta-Ta_2O_5 is only 1 eV at the maximum.

Once high voltage Ta polymer capacitors are successfully manufactured, the next improvement that has the potential to revolutionize the capacitor industry is the development of non-polar Ta capacitors. However, the direct combination of Ta and Ta_2O_5 does not seem to be best for developing non-polar capacitors because of the low 1 eV barrier between them. This value is not sufficiently high to keep the reverse polarity leakage current adequately low for the satisfactory performance of the capacitor. In other words, the low barrier does not preclude the possibility of a Ta capacitor withstanding a high reverse polarity across it; however, the low barrier suggests that it may not be possible to make Ta capacitors that perform equally well at both forward and reverse polarities. Other metal-insulator systems such as Al-Al_2O_3, which has a barrier height of approximately 3 eV between them, is more effective in blocking electron flow from the metal to the insulator during reverse operation. Currently, Ta is employed as the anode material because of its high volumetric efficiency and stability; however, other metals with these useful properties may be useful as the anode material for future devices.

APPENDIX

An Analysis of Measured Data

The following tests were performed to obtain the run-to-run variance and sample-to-sample variance for three samples. Ideally, measurements need to be conducted on about 30-50 samples to perform statistical analysis with good confidence. However, this was not possible because only a small number of capacitors were fabricated for this research and the time required for conducting I-time tests on capacitors was exceedingly large.

The first test involved conducting multiple I-time measurements at 10 V on one sample. The results from this test are shown in Fig. A.1, which shows the results from 14 continuous I-time measurements on an *in situ* capacitor. In this figure, the current level is seen to be decreasing with each 2 hour long run. In the first run, the final value of current was ~2.5 nA, this value decreased to ~800 pA in the last run. This trend was also observed in other samples. Such a trend suggests that the applied voltage is causing slow changes within the dielectric and/or the polymer of the capacitor. To get accurate consistent results, the capacitors need to be treated to revert them to their known state.

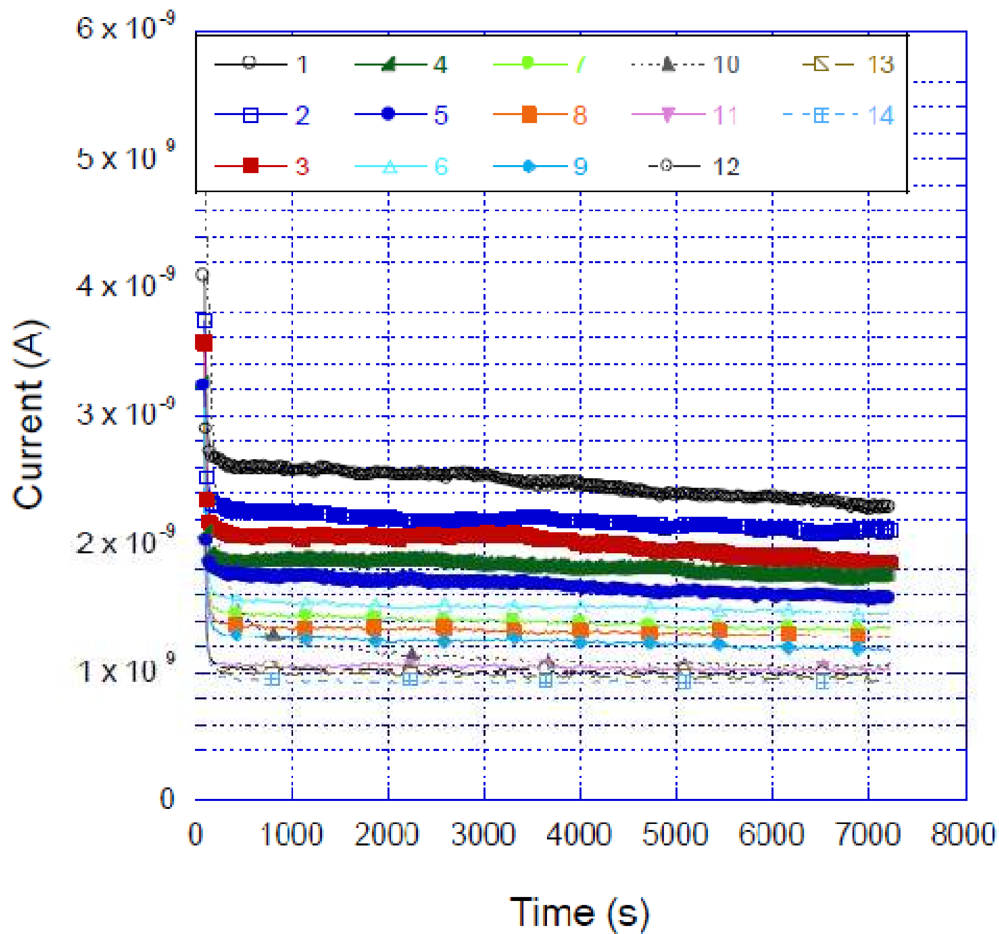

Fig. A. 1. Results from fourteen continuous I-time runs on an *in situ* capacitor.

To ensure the capacitors are in a known condition, the leads are shorted and the capacitor is placed in an oven at 85 ˚C for 6-8 hours. Using this approach, the I-time results shown in Fig. A.2 were obtained. During this test, first an I-time was performed on all the three capacitors at 10 V, after which they were treated as mentioned above. Another I-time was subsequently performed on all the three capacitors. The results in Fig. A.2 indicate that the current tracked within experimental error to the value that was observed in the first run. For example, R1P6 is the current observed in a sample during

the first run and HR1P6 is the current observed in the same sample after it was heat-treated.

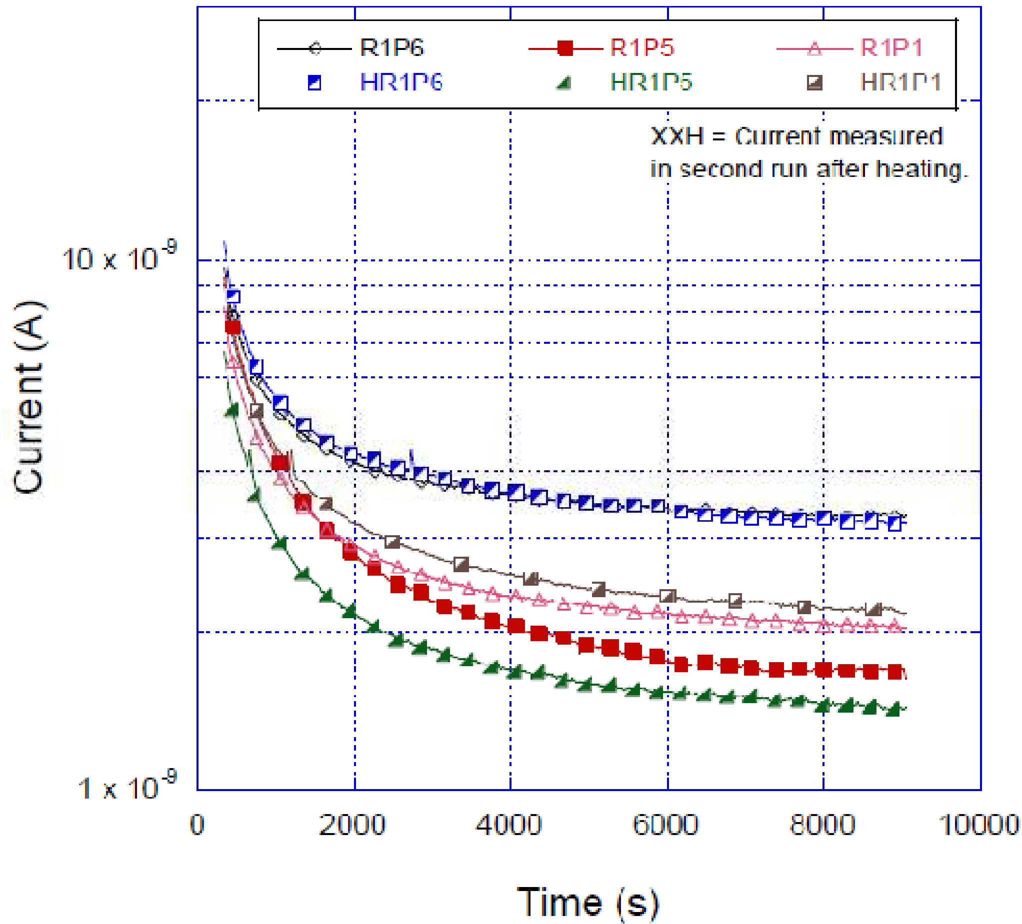

Fig. A.2. Comparison of I-time results on all samples.

From Fig. A.2, at 9000 s, the difference in current between the two runs is 0.1, 0.2, and 0.1 in samples 1, 2, and 3 respectively. Hence, the worst-case run-to-run variation of current is approximately 8 %. Similarly, the worst-case sample-to-sample variation of current is 1.7 nA, which is approximately ±38 % of the average measured current. The obtained sample-to-sample variation is about four times higher than the run-

to-run variation. Hence, the run-to-run variation can be ignored when the sample-to-sample variations are taken into consideration.

A ±38 % sample-to-sample variation is assumed throughout the 0-25 V range, and a Poole-Frenkel plot was constructed for Sample 3, which was previously characterized as shown in Fig. 6.1. This new Poole-Frenkel plot is shown in Fig. A.3. The worst case slopes of this plot are 0.0027 and 0.0062; however, the theoretical slope, $\frac{\beta}{\xi kT}$, ranges only between 0.0029 and 0.0058. Thus, the obtained slopes indicate that for the given sample-to-sample variation, the slope may not always fall within the range predicted by the Poole-Frenkel model. However, the obtained slopes are not significantly different from the theoretical slope range. This analysis shows the extreme theoretical limits and the limitation of the model used to explain the results. Possibly newer models can be developed to explain the out of range data.

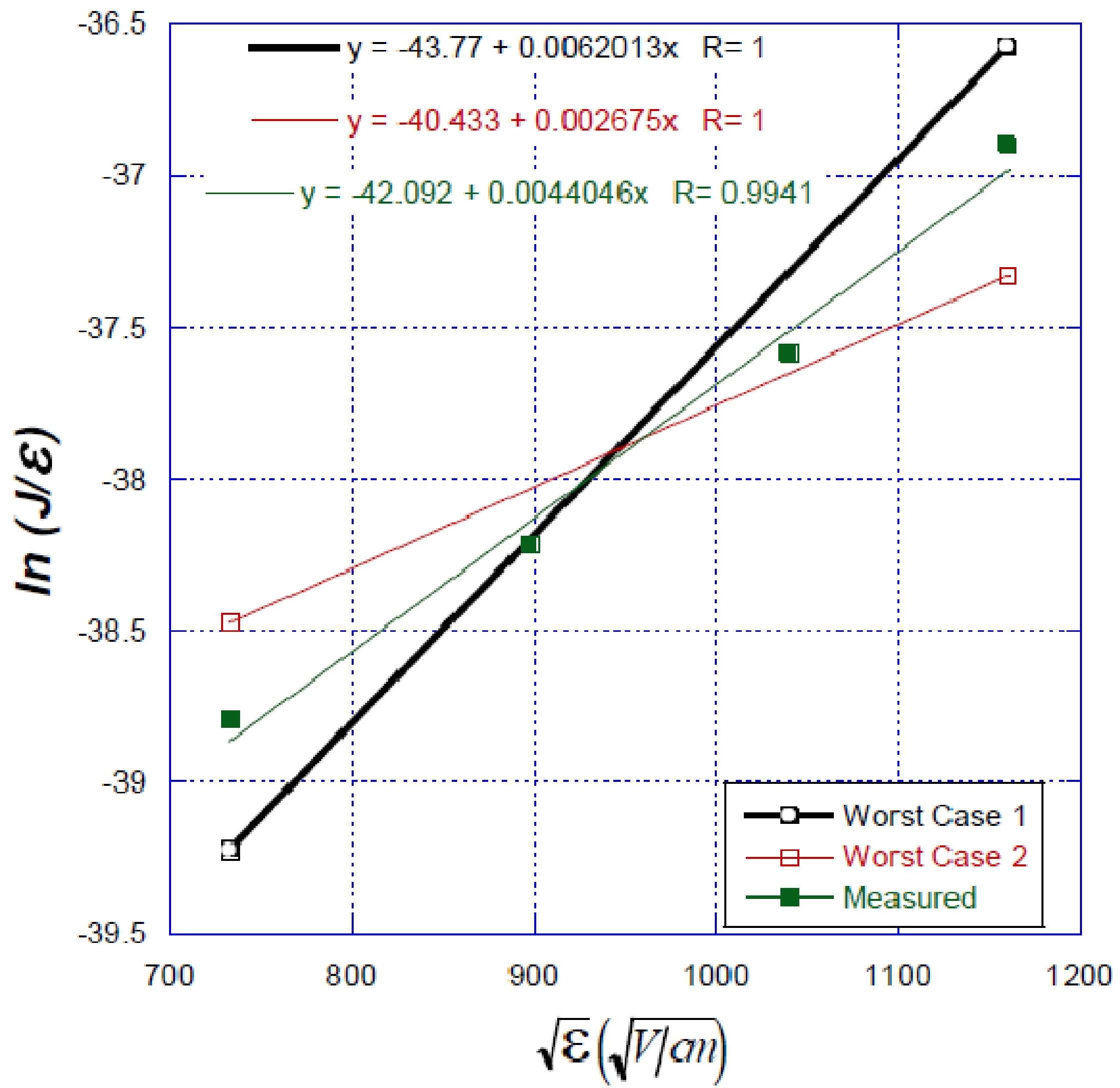

Fig. A.3. Worst-case PF plot.

REFERENCES

[1] KEMET Electronics Corp., "Defense and Aerospace: Tantalum Surface Mount Capacitors," 2006.

[2] S. Parler, "Electrochemistry Encyclopedia -- Electrolytic capacitors," vol. 2010, March, 2005.

[3] A. Nishino, "Capacitors: operating principles, current market and technical trends," J.Power Sources, vol. 60, pp. 137, 1996.

[4] P.M. Deeley, Electrolytic Capacitors - Theory, Construction, Characteristics, and Applications http://www.faradnet.com/deeley/

[5] L. Young, Anodic Oxide Films, New York: Academic Press, 1961.

[6] J. Moore and J.D. Prymak, "Tantalum Capacitors - Challenges and Developments," in TIC Conference, Portugal, 2003.

[7] K. Wakino, Y. Tsujimoto, K. Morimoto and N. Ushio, "Technological progress in materials application for electronic capacitors in Japan," Electrical Insulation Magazine, IEEE, vol. 6, pp. 29-43, 1990.

[8] J. Prymak, "New Tantalum Capacitors in Power Supply Applications," in IEEE Industry Applications Society Annual Meeting, 1998.

[9] D.A. Mclean and F.S. Power, "Tantalum Solid Electrolytic Capacitors," Proceedings of the IRE, vol. 44, pp. 872-878, 1956.

[10] Y. Freeman, R. Hauhn, P. Lessner and J. Prymak, "Reliability and critical applications of Tantalum capacitors," Passive Component Industry, vol. 1, pp. 22, 2007.

[11] T. Zednicek, "Trends in Tantalum and Niobium Capacitors," in CARTS USA 2006.

[12] Y. Kudoh, K. Akami and Y. Matsuya, "Solid electrolytic capacitor with highly stable conducting polymer as a counter electrode," Synth.Met., vol. 102, pp. 973-974, 6. 1999.

[13] J.D. Prymak, "Conductive polymer cathodes-the latest step in declining ESR in tantalum capacitors," Applied Power Electronics Conference and Exposition, 2000. APEC 2000. Fifteenth Annual IEEE, vol. 2, pp. 661-667 vol.2, 2000.

[14] A.P. Chandrakasan and R.W. Brodersen, Low-Power CMOS Design, Wiley-IEEE Press, 1997.

[15] J.D. Prymak, "Derating differences in Tantalum MnO_2 caps vs Tantalum-polymer caps vs Aluminum-polymer," in CARTS 2003, Components Technology Institute Inc. 2003.

[16] J.S. Shaffer, "Electrolytic capacitor with polymer conductor," 1986. 1983.

[17] H. Gerhard, B. Ottmar, F. Klaus, M. Helmut and M. Helmut, "Solid-state capacitor with an electroconducttve polymer as constituent of the solid electrolyte," 1989. 1987.

[18] S.D. Ross, "Method of making poly aniline solid electrolyte capacitor," 1993. 1991.

[19] S. Koji, M. Maki, F. Takashi, N. Toshihiko, A. Satoshi and T. Hiromichi, "Solid electrolytic capacitor and process for production thereof," 1996. 1994.

[20] Kosuke Amano, Hitoshi Ishikawa, Etsuo Hasegawa, "Solid electrolyte capacitor using polyaniline doped with disulfonic acid," 1996. 1995.

[21] P.M. Lessner, T.Y. Su, M. B.J. Melody, K. J.T. Kinard and V. Rajasekaran, "Process of preparing a solid electrolytic capacitor containing a conductive polymer counter electrode," 2002. 1998.

[22] T. Daisuke, "Solid electrolytic capacitor and method for preparing the same," 2003. 2002.

[23] J.R. Reynolds, F. Larmat and Y.-. Qui, "Polypyrrole as a solid electrolyte for tantalum capacitors," Synth.Met., vol. 79, pp. 229, 1996.

[24] F. Masahisa, F. Shin and N. Koji, "Solid electrolytic capacitor," 2001. 2001.

[25] B. Melody, T. Kinard, K. Moore and D. Wheeler, "Removal of organic acid based binders from powder metallurgy compacts," Nov 20, 2001. 2001.

[26] J.D. Prymak, "Improvements with polymer cathodes in aluminum and tantalum capacitors," Applied Power Electronics Conference and Exposition, 2001. APEC 2001. Sixteenth Annual IEEE, vol. 2, pp. 1210-1218 vol.2, 2001.

[27] B.T. Holman, "The Electrical Characterization of Tantalum Capacitors as Mis Devices," Master's Thesis, Department of Electrical and Computer Engineering, Clemson University, Clemson, USA, 2008.

[28] J. Young, J. Qiu, and R. Hahn, "High Voltage Polymer Ta Capacitors," in Proceedings of the 28th Symposium for Passive Electronic Components, pp. 241-251, 2008.

[29] Q. Yongjian, H. Randy S. and B. Keith R., "High voltage solid electrolytic capacitors using conductive polymer slurries," 2009. 2006.

[30] Y. Freeman, W.R. Harrell, I. Luzinov, B. Holman and P. Lessner, "Electrical Characterization of Tantalum Capacitors with Poly(3,4-ethylenedioxythiophene) Counter Electrodes," J.Electrochem.Soc., vol. 156, pp. G65-G70, 2009.

[31] C. Chaneliere, J.L. Autran, R.A.B. Devine and B. Balland, "Tantalum pentoxide (Ta_2O_5) thin films for advanced dielectric applications," Materials Science and Engineering: R: Reports, vol. 22, pp. 269, 1998.

[32] A.J. Kramer and E.C. Dickey, "Quarterly Research Report: Fundamentals of Tantalum Anodization: Effects of Curvature," 2009.

[33] B. Goudswaard and F.J.J. Driesens, "Failure Mechanism of Solid Tantalum Capacitors," in ElectroComponent Science and Technology, pp. 171-179, 1976.

[34] P.P.P. Budenstein, "On the Mechanism of Dielectric Breakdown of Solids," IEEE Transactions on Electrical Insulation, vol. EI-15, pp. 225-240, 1980.

[35] P.M. Lenahan and J. Conley J.F., "A physically based predictive model of Si/SiO_2 interface trap generation resulting from the presence of holes in the SiO_2," Appl.Phys.Lett., vol. 71, pp. 3126-3128, November 24, 1997.

[36] D.J. Dumin, K.J. Dickerson, M.D. Hall and G.A. Brown, "Polarity dependence of thin oxide wearout," in Reliability Physics Symposium, 1989. 27th Annual Proceedings., International, pp. 28-33, 1989.

[37] J. Wu, L.F. Register and E. Rosenbaum, "Trap-assisted tunneling current through ultra-thin oxide," in Reliability Physics Symposium Proceedings, 1999. 37th Annual. 1999 IEEE International, pp. 389-395, 1999.

[38] D.R. Young, E.A. Irene, D.J. DiMaria, R.F. De Keersmaecker and H.Z. Massoud, "Electron trapping in SiO_2 at 295 and 77 °K," J.Appl.Phys., vol. 50, pp. 6366-6372, October 1979.

[39] D.J. Dumin Ed., Oxide Reliability: A Summary of Silicon Oxide Wearout, Breakdown, and Reliability, World Scientific Publishing Company, Incorporated, 2002.

[40] N. Klein, "Switching and breakdown in films," Thin Solid Films, vol. 7, pp. 149-177, 4. 1971.

[41] A.T. Hideki Satake and, "SiO_2 dielectric breakdown mechanism studied by the post-breakdown resistance statistics," Semiconductor Science and Technology, vol. 15, pp. 471, 2000.

[42] R. Degraeve, G. Groeseneken, R. Bellens, M. Depas and H.E. Maes, "A consistent model for the thickness dependence of intrinsic breakdown in ultra-thin oxides," in Electron Devices Meeting, 1995., International, pp. 863-866, 1995.

[43] R.R. Degraeve, "A new model for the field dependence of intrinsic and extrinsic time-dependent dielectric breakdown," IEEE Trans.Electron Devices, vol. 45, pp. 472-481, 1998.

[44] N. Klein and H. Gafni, "The maximum dielectric strength of thin silicon oxide films," Electron Devices, IEEE Transactions on, vol. 13, pp. 281-289, 1966.

[45] E. Atanassova and A. Paskaleva, "Leakage current in thin-films Ta_2O_5 on Si – is it a limiting factor for nanoscale dynamic memories?" J.Mater.Sci.: Mater.Electron., vol. 14, pp. 671-675, 10/01/. 2003.

[46] Y.-. Zhao, G.-. Wang, T.-. Lu, G. Palasantzas and J.T.M. De Hosson, "Surface-roughness effect on capacitance and leakage current of an insulating film," Phys.Rev.B, vol. 60, pp. 9157-9164, Sep. 1999.

[47] J.J. O'Dwyer, The Theory of Dielectric Breakdown in Solids, London: Oxford University Press, 1964.

[48] Y. Freeman, "Clemson-KEMET Project, Electrical Characterization and Modeling of Leakage and Breakdown Mechanisms in Polymer Tantalum Capacitors," 2009.

[49] W.R. Harrell and J. Frey, "Observation of Poole–Frenkel effect saturation in SiO_2 and other insulating films," Thin Solid Films, vol. 352, pp. 195-204, 9/8. 1999.

[50] S.R. Elliott, Physics of amorphous materials, Longman, 1983, pp. 386.

[51] J.R. Yeargan and H.L. Taylor, "The Poole-Frenkel Effect with Compensation Present," J.Appl.Phys., vol. 39, pp. 5600-5604, 1968.

[52] J.G. Simmons, "Poole-Frenkel Effect and Schottky Effect in Metal-Insulator-Metal Systems," Phys.Rev., vol. 155, pp. 657-660, Mar. 1967.

[53] S.M. Sze, Physics of Semiconductor Devices, John Wiley and Sons, 1981.

[54] P. Mark and T.E. Hartman, "On Distinguishing between the Schottky and Poole-Frenkel Effects in Insulators," J.Appl.Phys., vol. 39, pp. 2163-2164, March 1968. 1968.

[55] A. Rose, "Space-Charge-Limited Currents in Solids," Phys.Rev., vol. 97, pp. 1538-1544, Mar. 1955.

[56] Y.L. Chiou, J.P. Gambino and M. Mohammad, "Determination of the Fowler–Nordheim tunneling parameters from the Fowler–Nordheim plot," Solid-State Electronics, vol. 45, pp. 1787-1791, 10. 2001.

[57] M. Lenzlinger and E.H. Snow, "Fowler-Nordheim Tunneling into Thermally Grown SiO_2," J.Appl.Phys., vol. 40, pp. 278-283, January 1969. 1969.

[58] J. Manceau, S. Bruyere, S. Jeannot, A. Sylvestre and P. Gonon, "Leakage current variation with time in Ta2O5 MIM and MIS capacitors," in Integrated Reliability Workshop Final Report, 2006 IEEE International, pp. 129-133, 2006.

[59] H. Miki, M. Kunitomo, R. Furukawa, T. Tamaru, H. Goto, S. Iijima, Y. Ohji, H. Yamamoto, J. Kuroda, T. Kisu and I. Asano, "Leakage-current mechanism of a tantalum-pentoxide capacitor on rugged Si with a CVD-TiN plate electrode for high-density DRAMs," in VLSI Technology, 1999. Digest of Technical Papers. 1999 Symposium on, pp. 99-100, 1999.

[60] E. Deloffre, L. Montès, G. Ghibaudo, S. Bruyère, S. Blonkowski, S. Bécu, M. Gros-Jean and S. Crémer, "Electrical properties in low temperature range (5 K–300 K) of Tantalum Oxide dielectric MIM capacitors," Microelectron.Reliab., vol. 45, pp. 925-928, 6. 2005.

[61] S. Duenas, E. Casta´n, J. Barbolla, R.R. Kola and P.A. Sullivan, "Use of anodic tantalum pentoxide for high-density capacitor fabrication," J.Mater.Sci.: Mater.Electron., vol. 10, pp. 379-384, 07/01/. 1999.

[62] P.L. Young, "dc electrical conduction in thin Ta_2O_5 films. II. Highly imperfect films," J.Appl.Phys., vol. 47, pp. 242-247, January 1976.

[63] W.W.S. Lau, "Detection of oxygen vacancy defect states in capacitors with ultrathin Ta_2O_5 films by zero-bias thermally stimulated current spectroscopy," Appl.Phys.Lett., vol. 83, pp. 2835, 2003.

[64] W.S. Lau, T.S. Tan, N.P. Sandler and B.S. Page, "Characterization of Defect States Responsible for Leakage Current in Tantalum Pentoxide Films for Very-High-Density Dynamic Random Access Memory (DRAM) Applications," Japanese Journal of Applied Physics, vol. 34, pp. 757-761, 1995.

[65] W.S. Lau, L. Zhong, A. Lee, C.H. See, T. Han, N.P. Sandler and T.C. Chong, "Detection of defect states responsible for leakage current in ultrathin tantalum pentoxide (Ta_2O_5) films by zero-bias thermally stimulated current spectroscopy," Applied Physics Letters, vol. 71, pp. 500-502, 1997.

[66] KEITHLEY, Low Level Measurements Handbook, 2004.

[67] Agilent Technologies, Agilent E4980A Precision LCR Meter User's Guide, Agilent Technologies, 2006.

[68] K. Allers, "Prediction of dielectric reliability from I–V characteristics: Poole–Frenkel conduction mechanism leading to $\sqrt{E}$ model for silicon nitride MIM capacitor," Microelectronics Reliability, vol. 44, pp. 411-423, 3. 2004.

[69] Y. Freeman, Personal Communication, April 2010.

[70] W.R. Harrell, T. Cordella and K. Poole, "Implications of Non-Linear Poole-Frenkel Plots on High-k Dielectric Leakage," ECS Trans., vol. 1, pp. 705-716, July 7, 2006.